Lithospheric structure imaging of Alberta from regional broadband seismic network

by

Yunfeng Chen

A thesis submitted in partial fulfillment of the requirements for the degree of

Master of Science

in
Geophysics

Department of Physics
University of Alberta

Abstract

The development of dense, broadband seismic network provides a solid foundation for the implementation of a variety of seismic imaging methods.The integration of receiver function method and finite-frequency traveltime tomography offershigh-resolution images of the crust and upper mantle structures in Alberta. The shear velocities from receiver function modelingprovide compelling evidencefor a crustal low velocity zone beneath the central Alberta. The P velocity model of the upper mantle recovered from body-wave traveltime inversion reveals 1) a well-defined Cordillera-craton transition coincides with the Cordillera deformation front, and 2) Archean-aged cratonic lithosphere under Medicine Hat Block and Loverna Block. These findings contribute to better understandings of the tectonic structure and evolution history of western Laurentia.

Acknowledgement

I would to express my sincere gratitude to my supervisor Dr. Gu for the continuous support and careful guidance during my MSc study and research. His passion in life and enthusiasm for scientific research alwaysinspire me.

I thank Professor Hung from Taiwan National University for kindly sending me code and supporting me in the tomography project.

I also would like to thank my fellows and friends in UofA for the help and fun we have had in the past two years.

Thanks to my families for all your love and support throughout my life.

Table of Contents

List of Figures

List of Symbols and Abbreviations

λ	Wavelength for seismic wave
μ	Damping parameter tradeoffs the misfit and model norm
ϕ	Cross-correlation coefficient
δc	Wave-speed perturbation
δl	Differential path length
δs	Slowness perturbation
δt	Traveltime perturbation
$\Delta\mathbf{d}$	Data residual vector
$\Delta\mathbf{m}$	Model correction vector
Δt	Relative arrival time
$\mathbf{d}$	Data vector (observed receiver function or traveltime)
$\mathbf{d}_0$	Receiver function corresponds to model $\mathbf{m}_0$
$\mathbf{D}$	Second-order differential matrix
$F[\mathbf{m}]$	Operator that produces the receiver function based on the model

$\mathbf{G}$	Inversion kernel
i, j, k	Vector/matrix indices
$\mathbf{I}$	Diagonal matrix
J	Cost function
$\mathbf{m}$	Model vector with M layers or M nodes
$\mathbf{m}_0$	Initial model
$\widehat{\mathbf{m}}$	Model solution
$\widetilde{\mathbf{m}}$	Wavelet domain expression of model $\mathbf{m}$
p	Ray parameter
$\mathbf{W}$	Weighting or wavelet transform matrix
AK135	AK135 reference earth model
CCP	Common conversion points
CDF	Cordillera deformation front
CRANE	Canadian Rockies and Alberta Network
Ga	Billions of year

LAB	Lithosphere asthenosphere boundary
LVZ	Low velocity zone
MCCC	Multi-channel cross-correlation
NMO	Normal moveout correction
Pds	P-to-S converted phase generated by discontinuity at depth d
PpPds	S reverberated phase generated by discontinuity at depth d
PpPdp	P reverberated phase generated by discontinuity at depth d
RF	Receiver function
PREM	Preliminary reference Earth model
SNR	Signal-to-noise ratio
WCSB	Western Canadian Sedimentary Basin

Chapter 1 Introduction

1.1 Background

Seismic imaging has been one of the most effective tools for the understanding of the evolution history and state of the Earth's interior [*Liu and Gu*, 2012]. On the global scale, researchers continue to pursue high-resolution models that explain the arrival times, waveforms, and phases of various waves recorded by the worldwide seismic network. Early examples are mainly one dimensional (1D) (e.g. PREM [*Dziewonski and Anderson*, 1981], IASP91 [*Kennett et al.*, 1995] and AK135 [*Montagner and Kennett*, 1996]), which provide solid representations of the average properties, such as elastic moduli, density and quality factor, as function of depth.These global models provided benchmarks for the regional-scale structures, where heterogeneous bodies such as low velocity zones, subducting slabs or mantle plumesoffer a much more detailed view of the processes, dynamics and mineralogy.

A critical depth range for the understanding of the Earth's history and evolution is the lithosphere, the outermost rocky shellcontaining the crust and shallow upper mantle[*Stein and Wysession*, 2009]. Investigation of lithosphere can be traced to 1909when Mohorovicic discovered a seismic velocity discontinuity at ~54 km depth between the crust and upper mantle;thisinterface became the well known Mohorovicic discontinuity or Moho for short [*Rawlinson and Sambridge*, 2003]. Since then, detailed information pertaining to the lithosphere has been uncovered owing to monumental progress in two areas: 1) development of the broadband seismographs and networks, and 2) improvement in seismic data analysis methods.

Seismic networks offer many advantages in signal detection and noise reduction in comparison with a single-station approach. A large number of uniform, broadband seismic stations with small station spacing are now producing high-quality seismic records with great consistency globally, which enhance signal-to-noise ratio (SNR) of the seismic source [*Rost and Thomas*, 2002] and structures substantially even with simplistic methods such as beam-forming. The global seismic networks developed relatively quickly since its debut in the 1950s [*Gu*, 2010]. Today, thousands of broadband instruments operate daily, thanks to the focused regional efforts in association with the ANZA seismic network in the southernmost California[*Kilb et al.*, 2003], Earthscope USArray Transportable Array (TA) network across the US[*Astiz et al.*, 2014], High sensitivity seismograph network (Hi-net) in Japan [*Obara*, 2003], recently deployed China Digital Seismic Network (CEArray) in northeastern China[*Niu*, 2011], among many others. The data from these arrays provide first order constraints on the crust and mantle structures, the key targets of this thesis. These datasets set the foundation for multi-scale analysis of critical seismic observables such as receiver functions, shear wave splitting parameters and traveltimes[*Gu*, 2010].

1.2 Motivation

In the spirit of the globalization of seismic arrays, the Canadian Rockies and Alberta Network (CRANE) was developed as the first passive broadband seismic array in Alberta, Canada;this array is jointly operated by the University of Alberta and Alberta Energy Regulator (AER). Since the deployments of the first seismic station in southern Alberta in 2006[*Gu et al.*, 2011], CRANE has increased its inventory to 24 three-component broadband receivers, with an average separation of 150 km, and forms a semi-uniform grid in central and southern Alberta. More than 8 years of continuous seismic data from the field are now incorporated into a large database with 500+ of GB seismic records. Most of the CRANE stations are

equipped with state-of-the-art instruments including Trillium 120, 240 and Compact three-component seismometers with flat frequency response ranging from 240 sec to 145 Hz. The wide frequency range of the CRANE data enables the full use of the information contained in a given seismic signal. The integration of relatively dense station coverage, extensive data and broadband signals is ideal conditions for investigating the regional crust and mantle seismic structures.

CRANE resides in the Alberta basin east of the Canadian Rockies. This region marks the southwestern corner of the Western Canadian Sedimentary Basin (WCSB) where the Precambrian crystalline basement is buried under the thick Phanerozoic sediments. The crystalline basement of Alberta is a complex tectonic assembly that comprisesa number of lithospheric fragments welded together during the 1.9-2.0 Ga Paleoproterozoic eon[*Ross et al.*, 2000]. Three major tectonic discontinuities, the Great Slave Lake Shear Zone (GSLSZ), the Snowbird Tectonic Zone (STZ) and the enigmatic Vulcan structure (VS) have been reported in northern, central and southern Alberta, respectively[*Ross et al.*, 1994]. The GSLSZ and STZ provide the rare surface exposures of the boundaries of the tectonic collision while the VS, which is entirely buried by the thick sediments, is only recognizable from its low potential field signature. Similarly, the vast regions of Alberta are masked by thick sediments and the subdivision of those tectonic fabrics is mainly dependent on the geochemical measurements of rock samples and gravity and aeromagnetic anomaly signatures of the basement in the early 1990's[*Ross et al.*, 1991; *Villeneuve et al.*, 1993].

Seismic exploration experiments have greatly contributed to the verification of aforementioned regional domain structures. As part of the trans-Canada LITHOPROBE project, the Alberta portion of seismic reflection transect is composed of Central Alberta Transect (CAT, 1992), Peace River Arch Industry Survey Experiment (PRAISE, 1994) and Southern Alberta Lithospheric Transect

(SALT, 1995). Crustal scale deformation in central Alberta and evidence of crustal thickening in southern Alberta were reported bythese earlier seismic surveys.These experiments were followed by the passive seismic experiments utilizing three-component seismometers. The Canadian Northwest Experiment (CANOE), which consisted of 60 three-component broadband stations,covered northern Alberta and extended northward to the Northwest Territories. A shear wave splitting study with CANOE data [*Courtier et al.*, 2010]reveals that the fast lithospheric anisotropy direction is roughly consistent with the plate motion. Teleseismic experiment in central-southern Alberta[*Shragge et al.*, 2002]discovered a high velocity lithospheric structure down to 200-250 km. The observation was interpreted as evidence of the preservation of lithosphere beneath the Archean Hearne province. The active-source refraction experiment, the Lithoprobe's Southern Alberta Refraction Experiment (SAREX) [*Clowes et al.*, 2002],investigatedthe crustal and upper mantle velocities of the Hearne craton. They reported a high velocity layer in the lower crust that is interpreted as the Paleoproterozoic underplating initiated by tectonic collision.

Despite the milestone efforts from earlier studies,they are limited by 1) linear receiver geometries of the seismic surveys and 2) short deployment duration of the temporal seismic arrays. Those deficiencies inevitably degrade the model resolution and confine the study of lithospheric structures in a 2D framework, which hindersa 3D investigation of the regional lithospheric structures with finer resolution.The CRANE network greatly improves the regional station coverage and fills in the gaps that are not investigated by the earlier surveys. Motivated by supplying a more complete view of lithospheric structure of Alberta, I apply high-resolution receiver function and finite-frequency tomographic methods to the high-quality datasets from the CRANE array, which can shed new light on the tectonic structure and evolution history of Alberta.

1.3 Thesis outline

Chapter 2 introduces the receiver function and finite-frequency tomographic methods. In the receiver function section, we outline thekey steps of preprocessing, deconvolution and inversion. Receiver functions are stacked and inverted for shear velocity structure with an iterative linear inversion scheme. The efforts of reducing the non-uniqueness of the inversion are explained in detail. The subsequent section reviews the finite-frequency tomography.The differences between the ray theory and finite-frequency theory are briefly explained,as well as theadvantage of finite-frequency over theoretical ray-theory based tomographic approaches.

Chapter 3 reveals a mid-crustal low velocity zone (LVZ) in central Alberta from the receiver function inversion. P-to-S receiver functions from more than 9000 events are analyzed and inverted for the shear velocity structure down to 80 km. The shear velocity model shows a 10+ km thick and 200+ km wide mid-crustal LVZ. We interpret the LVZ to be of granitic composition, formed by the crystallization of partially molten crust melted under favorable geological condition of convergent tectonic motion during the Paleoproterozoic eon. The LVZ is further supported by 1) high spatial correlation between LVZ and heat flow; 2) shear velocities that are consistent with laboratory measurements and reports of granite. The existence of a broad crustal LVZ suggests extensive subduction, orogenesis, and crustal melting during the Precambrian assembly of the North American craton.

Chapter 4 presents a new tomographic model of P-wave velocity perturbations for the lithosphere and upper mantle beneath the Cordillera-cration transition region in southwestern Canada based on finite-frequency theory and cross-correlation teleseismic relative traveltime data from the USArray, Canadian National Seismograph Network (CNSN) and CRANE. The inversion procedure

properly accounts for the finite-volume sensitivities of measured travel time residuals, and the resulting model shows a greater resolution of upper mantle velocity heterogeneity beneath the study area than earlier approaches based on the classical ray-theoretical approach. Our model reveals a lateral change of P velocities from -0.5% to 0.5% down to ~200-km depth in a 50-km wide zone between the Alberta Basin and the foothills of the Rocky Mountains, which suggests a sharp structural gradient along the Cordillera deformation front. The stable cratonic lithosphere, delineated by positive P-velocity perturbations of 0.5% and greater, extends down to a maximum depth of ~180 km beneath the Archean Loverna Block (LB). In comparison, the mantle beneath the controversial Medicine Hat Block (MHB) exhibits significantly higher velocities in the uppermost mantle and a shallower (130-150 km depth) root, generally consistent with the average depth of the lithosphere-asthenosphere boundary beneath Southwest Western Canadian Sedimentary Basin (WCSB). The complex shape of the lithospheric velocities under the MHB may be evidence of extensive erosion or a partial detachment of the Precambrian lithosphere. Furthermore, distinct high velocity anomalies in LB and MHB, which are separated by a 'normal' mantle beneath the Vulcan structure (VS), suggest different Archean assembly and collision histories between these two tectonic blocks.

Chapter 5 summarizes the key findings of the crustal and upper mantle structures from chapter 3 and chapter 4, respectively. Receiver function inversion images the shear velocity variations at crustal depthsandthe finite-frequency tomography is mostly sensitive to the upper mantle velocity anomalies, therefore a combination of the models from those two studies favorsacomplete understandings of lithospheric structure of Alberta. The recommendations of the future work are presented in the end.

Chapter 2 Receiver function and finite-frequency seismic tomography.

2.1 Receiver function method

2.1.1 Overview

The converted seismic waves generated at the subsurface impedance interfaces provide rich information about the Earth's internal discontinuities.*Burdick and Langston* [1977]compared the radial component with the vertical component seismograms and identified P-to-S converted phases resulting fromvelocity discontinuities beneath a given station. *Langston* [1979] applied a deconvolution technique to the radial component seismogram, which effectively removed the source time function and instrument response, and subsequently defined the source equalized radial component seismogram as the receiver function (RF). Since then, RF techniques have been widely used as an imaging tool in various aspects applications pertaining to,in a shortened list, craton structure[*James et al.*, 2003], Moho depth variation [*Zhu and Kanamori*, 2000], crustal LVZ in tectonically active orogens[*Beck and Zandt*, 2002; *Kind et al.*, 1996; *Zandt et al.*, 1994],and upper mantle transition zone thickness [*Bostock*, 1996; *Lawrence and Shearer*, 2006].

A key procedure in the RF computation is deconvolution, which removes the source signatures and increases the coherency of the seismic signals from different earthquakes. A commonly used deconvolution method is water-level deconvolution [*Clayton and Wiggins*, 1976], which is essentially a frequency division method with a minimum water-level value constraint to avoid numerical instability. [*Gurrola et al.*, 1995] applied a time domain deconvolution method to

simultaneously extract the RF from the inversion of the earthquake data. An alternative frequency-based approach is multi-taper deconvolution [*Park and Levin*, 2000], which tends to reduce frequency leakage at the expense of a higher computation cost. [*Ligorría and Ammon*, 1999] proposed a time-domain iterative deconvolution method that calculates the RF using correlation and convolution instead of the deconvolution. Since the time-domain iterative deconvolution does not require a subjectivechoice of the stabilization parameter, it is suitable for automated RF processing [*Crotwell and Owens*, 2005].

Once RFs are computed for individual event, they will be often subjected to stacking to improve the signal-to-noise ratio (SNR).Stacking can be performed on single stations as well as the P-to-S conversion points in common conversion point (CCP) gather[*Dueker and Sheehan*, 1997; *Yuan et al.*, 1997]. Furthermore, the availability of dense regionalnetworks enables comprehensive spatial sampling. The summation along diffraction hyperbolae can effectively collapse the scattering energy to the scatter point in a fashion similar to migration. Except for stacking RFs in time domain, H-k stacking [*Zhu and Kanamori*, 2000], a grid-search method that simultaneously determines the optimal Moho depth and Vp/Vs ratio has also been extensively used instudies of crustal structures.

2.1.2 Data preprocessing

Teleseismic events from 30 to 90 degrees are ideal for RFanalysis due to 1) the steep incidence angle of the seismic wave, 2) the lack of mantle triplication and PcP converted phase, and 3) the incidence P-wave is a plane wave beneath the regional array [*Rondenay*, 2009]. In our studies the seismic data are first bandpass filtered with Butterworth function at corner frequencies of 0.02 and 5 Hz to remove incoherent noise at very low or high frequencies. Filtered seismograms are often cut at 30 sec prior to, and 120 sec after, the predicted P-wave arrival time based on PREM [*Dziewonski and Anderson*, 1981]. Back-

azimuth is calculated according tostation and event locations and the N-S, E-W and vertical component seismogram are subsequently rotated to radial-transverse-vertical coordinate system using the following matrix transformation equation:

$$\begin{bmatrix} R \\ T \\ Z \end{bmatrix} = \begin{bmatrix} -\cos\theta & -\sin\theta & 0 \\ \sin\theta & -\cos\theta & 0 \\ 0 & 0 & 1 \end{bmatrix} \begin{bmatrix} N \\ E \\ Z \end{bmatrix}, \tag{2.1}$$

where θ is the back-azimuth,or the angle measured from incoming source-station path orientation relative to north. After the rotation, the P-wave energy is mainly focused on the vertical component while SV and SH converted energy are generally isolated on the radial and transverse components, respectively.

2.1.3 Deconvolution

Assuming the Earth structure is composed of flat-lying layers, which is a valid estimation to the first order, the ray path of the incident waves recorded by a station would resemble those shown in Fig. 2.1.

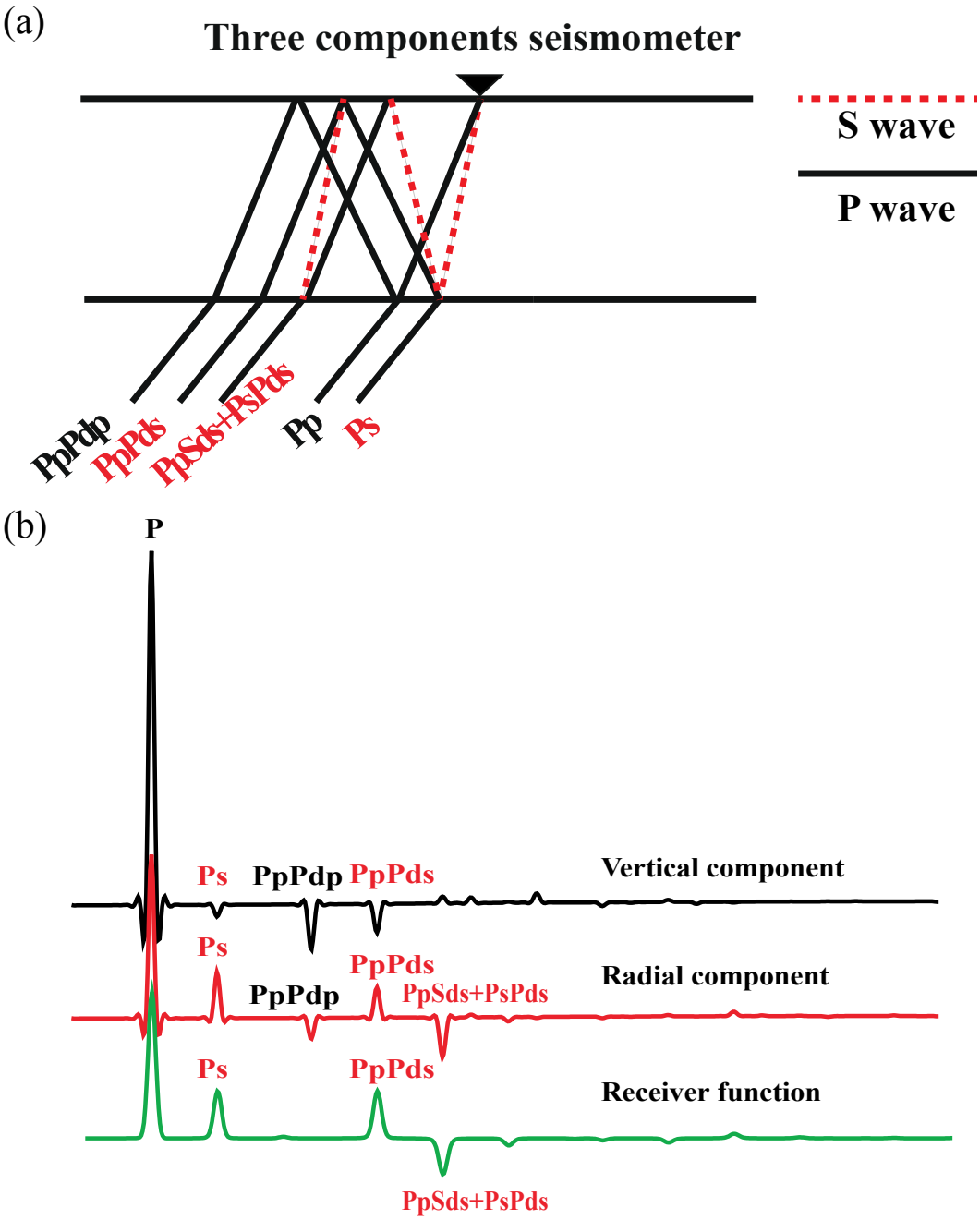

Fig. 2.1(a) Schematic diagram of the incident wave ray paths. (b)Vertical (black) and radial component seismograms (red) and receiver function (green) generated by the abovea layer over half-space model.

P-to-S conversions only occur at the impedance interface, where the amplitude of the converted Ps phase can be calculated based on Zoeppritz equations [*Aki and Richards*, 2002] that relate the incidence angle and the impedances of the bounding layers. The P-wave energy, which includes the energy of the direct P phase as well as those of reverberations, is projected onto the vertical and radial component (see Fig. 2.1b). The converted Ps and reverberations are mostly recorded on the radial component due to near vertical incidence angles of the seismic wave. Therefore, the removal of P wave energy and reverberations on the radial component seismogram will preferentially emphasize the converted waves recorded on the radial component seismogram, then the seismogram with only Ps phases remaining can ideally reflect the strength and the depth of the subsurface by the amplitude and the timing of the pulses.

Mathematically, we can express the radial and vertical component seismograms as

$$\begin{cases} Z(t) = \sum_{k=0}^{n} z_k s(t - t_k) \\ R(t) = \sum_{k=0}^{n} r_k s(t - t_k) \end{cases}, \tag{2.2}$$

where $s(t)$ is the source time function, the subscript k indicates the k-th incident ray recorded by the station. Variables z_k and r_k are the amplitude of the k-th ray on the vertical and radial components, respectively and t_k is the arrival time of the k-th ray. Deconvolvingthe vertical from the radial component seismograms in the frequency domain yields

$$H(\omega)=\frac{R(\omega)*S(\omega)}{Z(\omega)*S(\omega)}, \tag{2.3}$$

where $S(\omega)$ is the frequency spectrum of the source time function $s(t)$. The terms $R(\omega)$ and $Z(\omega)$ correspond to the frequency spectra of the radial and vertical component seismograms, respectively, where

$$\begin{cases} Z(\omega)=\sum_{k=0}^{n} z_k s(t-t_k) \\ R(\omega)=\sum_{k=0}^{n} r_k s(t-t_k) \end{cases}. \tag{2.4}$$

The symbol $\widehat{z_k}$ represents the amplitude of the vertical component of the k-th ray after the P-wave normalization, whereas, $\widehat{r_k}$ is the radial component equivalent amplitude term.If one only considers the first three arrivalsP, Ps and PpPdp (due to their sizable energy, see Fig. 2.1b), then $R(\omega)$ and $Z(\omega)$ can be expressed as

$$\begin{cases} R(\omega)=r_0\left(1+\widehat{r_p}e^{-i\omega t_p}+\widehat{r_s}e^{-i\omega t_s}\right) \\ Z(\omega)=r_0\left(1+\widehat{z_p}e^{-i\omega t_p}+\widehat{z_s}e^{-i\omega t_s}\right) \end{cases}. \tag{2.5}$$

Based on equation (2.3), receiver function $H(\omega)$ can be evaluated from the following spectral ratio

$$H(\omega)=\frac{r_0}{z_0}\frac{1+\widehat{r_p}e^{-i\omega t_p}+\widehat{r_s}e^{-i\omega t_s}}{1+\widehat{z_p}e^{-i\omega t_p}+\widehat{z_s}e^{-i\omega t_s}}. \tag{2.6}$$

Note that the relationship of $\widehat{r_p} = \widehat{z_p}$ is only valid for a planar incident P wave. Due to the steep incident angle of P wave at teleseismic distances (30-90 degrees), P-to-S converted energy is much smaller than the direct P wave and therefore $\widehat{z_s} \ll 1$. Equation (2.6) can then be simplified as

$$H(\omega) = \frac{r_0}{z_0} \frac{1 + \widehat{z_p} e^{-i\omega t_p} + \widehat{r_s} e^{-i\omega t_s}}{1 + \widehat{z_p} e^{-i\omega t_p}}. \tag{2.7}$$

Since $\widehat{z_p}$ is usually smaller than 0.5, onecan expand equation(2.7)using Taylor series:

$$H(\omega) = \frac{r_0}{z_0} \left(1 + \widehat{z_p} e^{-i\omega t_p} + \widehat{r_s} e^{-i\omega t_s}\right)\left(1 - \widehat{z_p} e^{-i\omega t_p} + \widehat{z_p}^{\,2} e^{-2i\omega t_p} - \cdots\right). \tag{2.8}$$

Neglecting the higher order terms in the equation (2.8) yields

$$H(\omega) = \frac{r_0}{z_0} \left(1 + \widehat{r_s} e^{-i\omega t_s}\right), \tag{2.9}$$

while the time domain signal becomes

$$h(t) = \frac{r_0}{z_0} \left(1 + \widehat{r_s} \delta\left(t - t_s\right)\right). \tag{2.10}$$

As Equation (2.10) indicates, the RF is intrinsically a scaled version (by a factor of $1/z_0$) of the radial component seismogram atthe removal of P-wave multiples $\widehat{r_p}\delta\left(t - t_p\right)$[*Ammon*, 1991].

2.1.4 Moveout correction and RF stacking

The moveout correction used in RF study in global seismology is similar to the concept of the Normal Moveout Correction (NMO) in exploration seismology. SinceRF uses the teleseismic P waves from 30 to 90 degrees, changes in incidence angles will cause considerable delays between P and the converted phases (i.e., P-Ps times). Based on the equation given by *Rondenay* [2009], the moveout correction can be formulated as

$$R(t) = \mathrm{IFT}\left(\hat{r}(\omega) e^{i\omega \Delta T_{ps}(p,h)}\right), \tag{2.11}$$

where IFT represents the Inverse Fourier Transform, $\hat{r}(\omega)$ and p are the frequency spectrum and ray-parameter of the RF, respectively. In this equation,$h$represents the conversion depth corresponding to time t and ΔT_{ps} is the time correction term corresponding to

$$\Delta T_{ps}(p,h) = T_{ps}(p,h) - T_{ps}(p_0,h), \tag{2.12}$$

where $T_{ps}(p_0,h)$and $T_{ps}(p,h)$ are the P-Ps time for the reference and final RF, respectively. Based on equations(2.11) and (2.12), we stretch or compress the RFs so that they are properly aligned with respect to the RF at the reference distance (60 degree in this study).

Finally, *Owens et al.* [1984]addressed the importance of stacks in improving the SNR of individual RFs. Two commonly adopted practices are station-based and CCP-based stacking of Ps arrivals. The choice between them largely depends on the relationship between station spacing and station aperture,which is defined as the maximum lateral distance sampled by the converted wave, a depth-

dependent quantity. As a rule of thumb, the lateral sampling distance is approximately 1/3rd of the depth to the subsurface interface [*Landes et al.*, 2006] or, more generally, approximately 0.4 to 0.7 times the depth to the interfacedepending on frequency and subsurface structure [*Cassidy*, 1992]. Fig. 2.2 schematically shows the relationship between station spacing and aperture [modified after *Rondenay*, 2009].

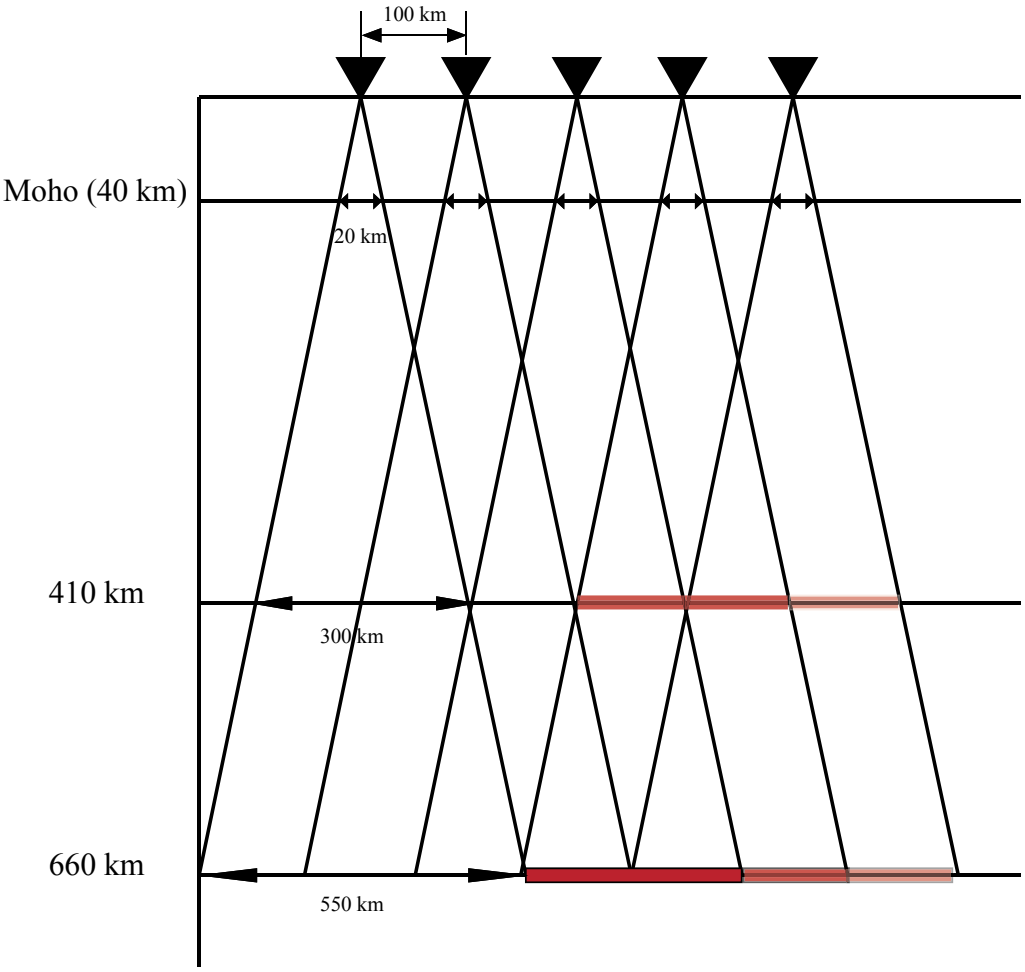

Fig. 2.2Schematic diagram illustrating the station spacingvs. aperture relationship. The station aperture becomes larger as the conversion interface increases in depth. The red color marks the overlapped apertures contributed from the nearby stations.

As illustrated in Fig. 2.2, the overlaps in ray coverage, which increases resolution at a given interface, decreases at shallower depths. This drawback is largely overcome by the use of CCP stacks for interface depth below ~200 km. In other words, CCP stacking provides higher lateral resolution than station-based stacking for relatively deep interfaces[*Dueker and Sheehan*, 1997]. The targeting structure of this thesis (crust< 60 km) requires a station spacing of ~40 km or less to achieve the ideal lateral resolution. Unfortunately, this is untenable due to the large average station separation within the regional networks (~150 km). Hence, station-base RF stack approach will be the main focus of the subsequent chapters.

2.1.5 Linear inversion of receiver functions

Whereas a pseudo two-dimensional (2D) profile constructed from stacked waveforms can reflect the depth and the geometry of the crustal/mantle interfaces, a more accurate projection of data space to the structural characteristics requires waveform of the RFs. The time domain linear inversion scheme of RFs was first introduced by*Owens et al.* [1984].*Ammon et al.* [1990]presenteda linearized RF inversion methodin detail and discussed the non-uniqueness problem due to the well-known velocity-depth tradeoffs during RF inversions.This part of my thesis follows Ammon's linearized inversion procedure and introduces regularizationmethods that impose priorconstraints on the inversion.The forward problem of the RF can be described as

$$\mathbf{d} = F[\mathbf{m}] \tag{2.13}$$

where $\mathbf{d}$ is the RF observation of length N, F is the operator that produces the RF based on the model $\mathbf{m}$ with M layers. To linearize equation (2.13), we expand it into a Taylor series with respect toan initial model $\mathbf{m_0}$ that is close to ground truth $\mathbf{m}$:

$$F[\mathbf{m}] = F[\mathbf{m_0}] + \mathbf{G}\Delta\mathbf{m} + O\left\|\Delta\mathbf{m}^2\right\|, \tag{2.14}$$

where $\Delta\mathbf{m} = \mathbf{m} - \mathbf{m_0}; \mathbf{G}$, the inversion kernel, is the first-order partial derivative of operator $F[\mathbf{m}]$ with respect to $\mathbf{m_0}$, $O\left\|\Delta\mathbf{m}^2\right\|$ is the higher order nonlinear term. Ignoring the nonlinear term and rearranging equation (2.14) yields

$$\mathbf{G}\Delta\mathbf{m} \approx F[\mathbf{m}] - F[\mathbf{m_0}], \tag{2.15}$$

where right-hand side of equation (2.15)is the residual vector $\Delta\mathbf{d}$. Equation (2.15) is an ill-conditioned system of linear equations that is solvable with the standard Least-Squares algorithm [*Wiggins*, 1972].Instead of solving for model correction term $\Delta\mathbf{m}$, we can evaluate the model vector $\mathbf{m}$ by adding a term $\mathbf{Gm_0}$ to both sides of equation (2.15):

$$\mathbf{Gm} = \Delta\mathbf{d} + \mathbf{Gm_0}. \tag{2.16}$$

This equation can be solved by minimizing the following cost function

$$J = \left\|\mathbf{Gm} - \hat{\mathbf{d}}\right\|_2^2 + \mu\left\|\mathbf{m}\right\|_2^2, \tag{2.17}$$

where $\hat{\mathbf{d}} = \Delta\mathbf{d} + \mathbf{Gm_0}$, μ is the damping parameter that controls the tradeoff between data misfit (first term on the left-hand side of equation (2.17)) and model norm (second term on the left-hand side of equation (2.17)).The standard least-squares solution of equation (2.17) becomes

$$\widehat{\mathbf{m}} = \left(\mathbf{G}^T\mathbf{G} + \mu\mathbf{I}\right)\mathbf{G}^T\hat{\mathbf{d}} \tag{2.18}$$

Though the model solution $\widehat{\mathbf{m}}$ can possibly fit the observation with a minimaldata misfit, itoften exhibitsvery rapid velocity variations that lead to unrealistic geological interpretations. An improvedmodel solution of $\widehat{\mathbf{m}}$ requiresthe additional roughness constraints on the cost function as:

$$J = \left\| \mathbf{G}\mathbf{m} - \hat{\mathbf{d}} \right\|_2^2 + \mu \left\| \mathbf{D}\mathbf{m} \right\|_2^2, \tag{2.19}$$

where $\mathbf{D}$ is the second-order derivative matrix defined by

$$\mathbf{D} = \begin{bmatrix} 1 & -2 & 1 & 0 & \cdots & 0 & 0 \\ 0 & 1 & -2 & 1 & \cdots & 0 & 0 \\ 0 & 0 & 1 & -2 & \cdots & 0 & 0 \\ 0 & 0 & 0 & 1 & \cdots & 0 & 0 \\ \vdots & \vdots & \vdots & \vdots & \cdots & \vdots & \vdots \\ 0 & 0 & 0 & 0 & \cdots & 1 & -1 \\ 0 & 0 & 0 & 0 & \cdots & 0 & 1 \end{bmatrix}. \tag{2.20}$$

By adding the term $\left\| \mathbf{D}\mathbf{m} \right\|_2$ to the cost function, the inversion also minimizes the L2 norm of the second order derivative of the model vector, whichsuppresses the rapid fluctuations in the model parameters and results in a smooth solution. Through reorganization equation (2.19)becomes

$$J = \left\| \begin{bmatrix} \mathbf{G} \\ \mu^{1/2}\mathbf{D} \end{bmatrix} \mathbf{m} - \begin{bmatrix} \hat{\mathbf{d}} \\ \mathbf{0} \end{bmatrix} \right\|_2^2. \tag{2.21}$$

If $\widetilde{\mathbf{G}} = \begin{bmatrix} \mathbf{G} \\ \mu^{1/2}\mathbf{D} \end{bmatrix}$ and $\tilde{\mathbf{d}} = \begin{bmatrix} \hat{\mathbf{d}} \\ \mathbf{0} \end{bmatrix}$, minimizing equation (2.21) is essentially solving the linear equation

$$\widetilde{\mathbf{G}}\mathbf{m} = \tilde{\mathbf{d}}. \tag{2.22}$$

Equation (2.22) is usually an ill-posed problem where $\widetilde{\mathbf{G}}$ is rank deficient. The generalized inverse $\widetilde{\mathbf{G}}^{-1}$ can be computed by Singular Value Decomposition (SVD) [*Lawson and Hanson*, 1974], where small singular values are eliminated to ensure an invertible matrix as well as a stable solution.

Other pre-conditioning schemes in addition to roughness constraint are also applied to the inversion to alleviate the non-uniqueness of the RF inversions. First, low and high frequency RFs are modeled simultaneously to constrain the structures at different wavelengths. In this case, the data vector $\mathbf{d}$ becomes two terms, $\mathbf{d}^h$ and $\mathbf{d}^l$, that represent the high- and low-frequency RFs, respectively. The inversion kernel $\mathbf{G}$ is also expanded to $\mathbf{G}^h$ and $\mathbf{G}^l$ corresponding to two different datasets. Then equation (2.22) can be reformulated as

$$\begin{bmatrix} \mathbf{G}^l \\ \mathbf{G}^h \\ \mu^{1/2}\mathbf{D} \end{bmatrix} \mathbf{m} = \begin{bmatrix} \hat{\mathbf{d}}^l \\ \hat{\mathbf{d}}^h \\ \mathbf{0} \end{bmatrix}, \tag{2.23}$$

where $\hat{\mathbf{d}}^l = \mathbf{G}^l\mathbf{m_0} + \mathbf{d}^l - \mathbf{d}_\mathbf{0}^l$ and $\hat{\mathbf{d}}^h = \mathbf{G}^h\mathbf{m_0} + \mathbf{d}^h - \mathbf{d}_\mathbf{0}^h$.

The second pre-conditioning step is to assign different weights to model layers with*a priori* information, e.g. speed of sedimentary layers from well-logging, in the model [*Chen and Niu*, 2013]. To accomplish this, we add a new set of linear equations to equation (2.23):

$$\begin{bmatrix} \mathbf{G}^{l} \\ \mathbf{G}^{h} \\ \mu^{1/2}\mathbf{D} \\ \mathbf{W} \end{bmatrix} \mathbf{m} = \begin{bmatrix} \hat{\mathbf{d}}^{l} \\ \hat{\mathbf{d}}^{h} \\ \mathbf{0} \\ \mathbf{W}\mathbf{m}_{\mathbf{0}} \end{bmatrix}, \tag{2.24}$$

where $\mathbf{W}$ is a diagonal matrix with thediagonal element w_{ii}, the weighting factor corresponds to layer i in the model [*Chen and Niu*, 2013]. The value of w_{ii} is proportional to the amount of weight assigned to layer i, and therefore larger valuesare assigned to layersthat need to be fixed.

2.2 Teleseismic P-wave travel time tomography

2.2.1 Overview

Seismic waves contain rich information on physical parameters such as velocity, density, and quality factor Q. The RF method introduced in the previous section utilizes the waveform of the P-wave coda to detect the velocities and depths of crustal discontinuities. This dataset ideally complements seismic tomography that is more sensitive to the relatively smooth variations in rock elastic properties.

Tomographic problems generally falls into four categories based on the data used in the inversion procedures, which are: normal incidence reflection, refraction and wide-angle reflection, local earthquake tomography and teleseismic tomography [*Rawlinson and Sambridge*, 2003]. The subject of discussion in chapter 4 belongs to the fourth category, which utilizes traveltime information from the teleseismic data to image the crust and upper mantle beneath a receiver array.

The first teleseismic tomography study was conducted by *Aki et al.* [1977], which determined seismic velocities down to 126 km beneath the Norsar array in Norway. From then on, increasing seismic data from regional arrays in combination with improved traveltime measurements[*VanDecar and Crosson*, 1990], model parameterizations[*Sambridge*, 1990; *Thurber*, 1983], forward modeling theory [*Dahlen et al.*, 2000; *Hung et al.*, 2000] and inversion methods[*Humphreys and Clayton*, 1988; *Scales*, 1987; *Tromp et al.*, 2005] have resulted in high-resolution global and regional tomographic models (Refer to *Liu and Gu* [2012] for a more detailed review).

The concept of teleseismic tomography is illustrated in Fig. 2.3, where the region of study beneath a seismic array is sampled by the teleseismic waves propagating through the crust and upper mantle. Since the traveltime measured from a recording station is influenced by the geometry of the ray path and velocity distribution along the ray path, the elastic properties of the crust and mantle rocks can be reconstructed by integrating and inverting a projection function between the source and receiver [*Liu and Gu*, 2012]. The basic processing steps of the teleseismic tomographic problem are introduced in the following section.

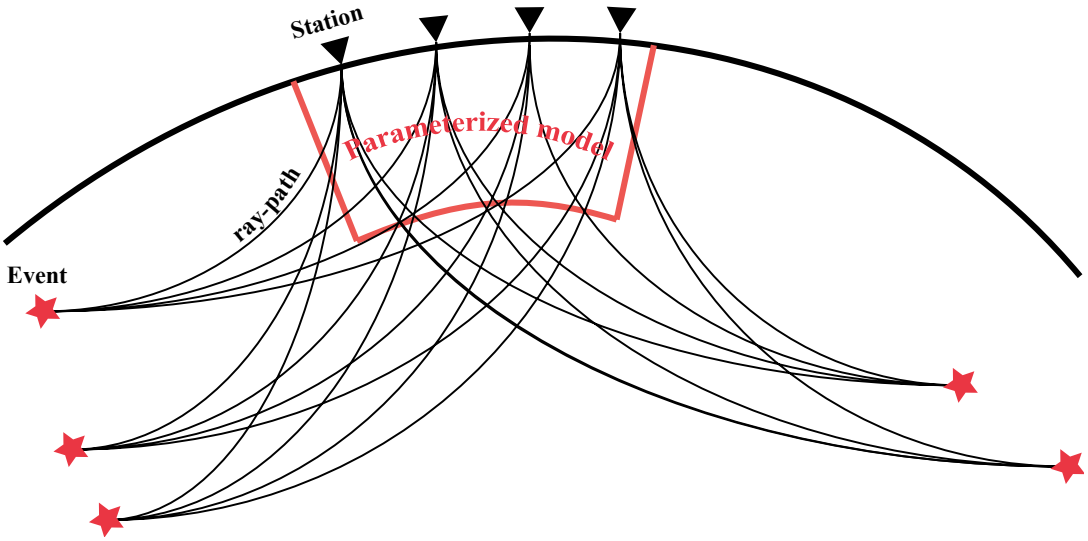

Fig. 2.3 Schematic diagram showing the concept of teleseismic body wave tomography.

2.2.2 Multichannel cross-correlation measurement of relative arrival times of P-waves

Teleseismic traveltime measurement has been the cornerstone of seismic tomography as high quality tomographic images provide a backdrop for a wide range of geological interpretations pertaining to the dynamics, temperature and mineralogy of the Earth's crust and mantle (e.g. review paper*Romanowicz* [1991]; *Liu and Gu* [2012]). Traveltime measurements have evolved from the early stagesof manual picking from smoked paper to efficient automatic routines. Two widely adopted methods are the single-trace phase picking [*Allen*, 1978; *Bai and Kennett*, 2001; *Crosson and Hesser*, 1983; *Earle and Shearer*, 1994] and the multi-station cross-correlation[*VanDecar and Crosson*, 1990]. The latter approach is particularly advantageous due to its sensitivity to the relative, rather than absolute, arrival times between similar seismic waves impinging on a seismic array.

Multi-channel cross-correlation(MCCC) method determines the relative time delay of a station pair by cross-correlating their waveforms with the following equation

$$\phi_{ij}(\tau) = \frac{\delta t}{T} \sum_{k=1}^{T/\delta t} x_i\left(t_i^p + t_0 + k\delta t + \tau\right) x_j\left(t_j^p + t_0 + k\delta t\right), \tag{2.25}$$

where x_i is the seismograph of the i-th trace, t_i^p is the predicted P-wave arrival time based on a reference Earth model (e.g. PREM), t_0 is time difference between the predicated arrival time and the beginning of the time window, t_0 is the time lag, T is the length of the correlation window and δt represents the sample interval. The optimized time lag is the dictated position of the largest cross-correlation value. A quantitative evaluation of the cross-correlation results can be achieved by calculating the correlation coefficients from equation

$$r_{ij} = \frac{\phi_{ij}\left(\tau_{ij}^{\max}\right)}{\sigma_i \sigma_j}, \tag{2.26}$$

where ϕ is the cross-correlation value and σ is the variance of the signal in the selected time window.

Relative delay times for all station pairs are determined by cross-correlation. Although the cross-correlation delay times are relatively precise, inconsistencies do exist in the measurements. In a three-station case, assuming the precise absolute arrival times are t_1, t_2 and t_3 corresponding to stations 1, 2 and 3,the relative delay time between station 1 and 2 is then calculated by $t_1 - t_2 = \Delta t_{12}$, and Δt_{23} and Δt_{13} are defined accordingly. Ideally, the summation of the three relative delay times is 0, but the presence of noise and errors in the cross-

correlation measurements often lead to a non-zero value. Therefore, additional optimization can be applied through a system of linear equations

$$\begin{bmatrix} 1 & -1 & 0 \\ 1 & 0 & -1 \\ 0 & 1 & -1 \\ 1 & 1 & 1 \end{bmatrix} \begin{bmatrix} t_1 \\ t_2 \\ t_3 \end{bmatrix} \cong \begin{bmatrix} \Delta t_{12} \\ \Delta t_{13} \\ \Delta t_{23} \\ 0 \end{bmatrix}, \tag{2.27}$$

where the matrix on the right-hand side of the equation contains the differential times for then given station pairs. The last row of the matrix forces the average of the travel time to zero, i.e., the optimized travel timesshouldsubtract the regional averageof the absolute travel times. Fig. 2.4shows a sample of the MCCC measurement. Data from 29 stations are aligned by the theoretical P-wave arrival time (Fig. 2.4a) and the MCCC optimized P-wave arrival time (Fig. 2.4b), respectively.

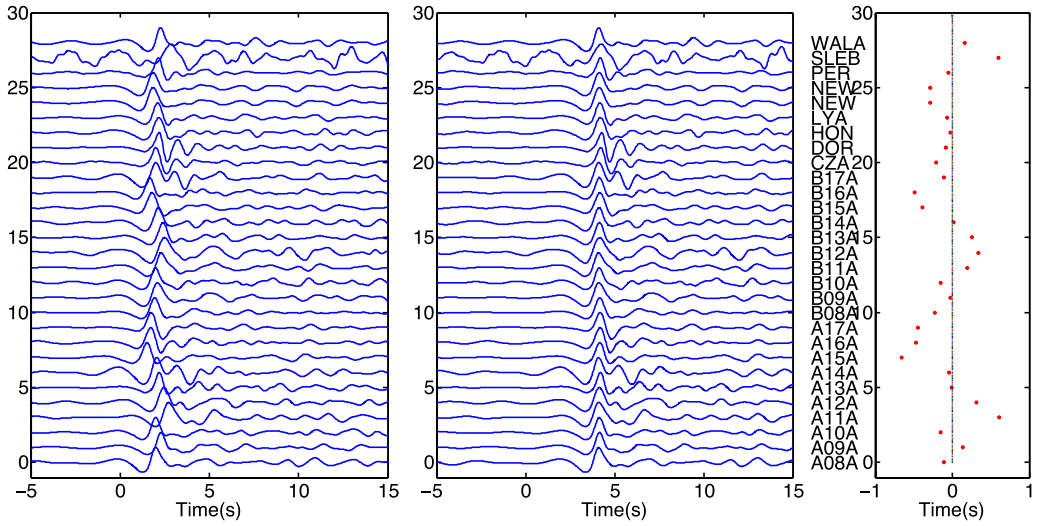

Fig. 2.4 Sample MCCC measurements. (a) Traces aligned by theoretical P-wave arrival time. (b) Traces aligned by MCCC optimized P-wave traveltime. (c)

The amount of time shift for each individual trace relative to the regional average (0 sec).

2.2.3 Ray theory verses finite-frequency theory

In conventional ray theory, seismic wave is assumed to travel solely along the infinitely thin geometrical ray path [*Hung et al.*, 2004], where a velocity perturbation δc causes a perturbation in traveltime δt. The tomographic problem can be expressed as

$$\delta t = -\int_L \delta c(x) c(x)^{-2} dl, \tag{2.28}$$

where $-\delta c(x) c(x)^{-2} = \delta\left(1/c(x)\right)$ is the slowness perturbation $s(x)$, i.e., equation (2.28)can be simplified to

$$\delta t = \int_L \delta s(x) dl, \tag{2.29}$$

where the sensitivity kernel for the travel time inversion is defined as a small segment of path length*dl*.

Unfortunately, equation (2.29) is valid only for infinite frequency seismic waves. In reality, seismic waves with frequencies varying from hundreds of seconds to tens of Hertz are sensitive to 3D volume known as the Fresnel zones off the geometrical ray path[*Dahlen et al.*, 2000; *Hung et al.*, 2004]. According to the finite-frequency theory, heterogeneities with scales comparable to the wave-lengths of the seismic waves within the Fresnel zone can all contribute to the traveltime shift δt, the relationship of which can be formulated into the following equation

$$\delta t = \iiint_{\oplus} K(x)\delta c(x)/c(x)d^3x, \tag{2.30}$$

where $\oplus$ represents the volume for the integration and $K(x)$ is the sensitivity kernel that can be effectively computed byBorn single-scattering approximation[*Hung et al.*, 2004]. Based on Born approximation, the advance or delay of the waveform δt is assumed to caused by the point scatters off the ray path, which can be calculated by integrating the product of the sensitivity kernel $K(x)$and velocity perturbation over the entire Earth where there is non-zero wave speed perturbations [*Dahlen et al., 2000*]. A detailed derivation of the sensitivity kernel is beyond the scope of this thesis and the knowledge level of the author. For detailed explanations of the finite-frequency theory, the readers are encouraged tostudies by *Marquering et al.* [1999], *Dahlen et al.* [2000]and *Hung et al.* [2000].

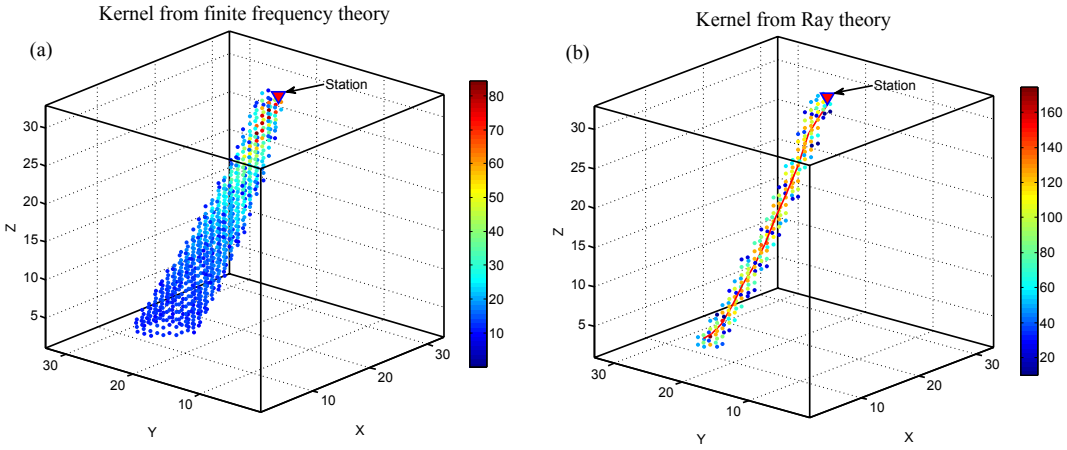

Fig. 2.5Inversion kernels derived from (a) finite-frequency theory and (b) traditional ray theory.

The sensitivity kernel $K(x)$ is a frequency-dependent variable as reflected by variable shapes/dimensions of the volumetric Fresnel zones corresponding to the seismic waves with different dominant frequencies. The width of Fresnel zone varies with respect to the propagation distance (Fig. 2.5a), which is thinner near the source and receiver butattains the maximum width at the turning point of the ray, resembling the shape of a banana. Surprisingly, along the ray path where the ray theory renders the maximum sensitivity (Fig. 2.5b), the finite-frequency kernel actually achieves the minimum sensitivity, which makes the kernel a hollow banana shape. Hence, the finite-frequency kernel is also nicknamed the'Banana-Donut kernel'.

There are lingering debates over the merits of finite-frequency theory[*Van Der Hilst and Maarten*, 2005]. In theory, the finite-frequency kernels are more accurate than the ray-theory counterpart especially at teleseismic frequencies. However, the sparseness of data coverage and effects associated with noise and imperfect measurements could overshadow the intrinsic improvements associated with the use of finite-frequency kernels[*Van der Hilst et al.*, 2007].Comparisons of global tomographic images based on ray and finite-frequency theories usually result in minordifferences in image resolution [*Liu and Gu*, 2012], which could easily be reproduced by varying the regularization parameter in the inversion approaches [*Montelli et al.*, 2006].

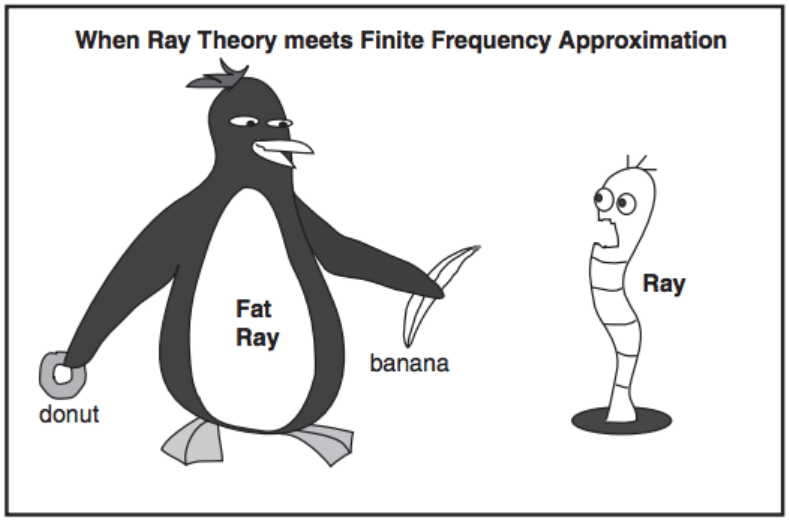

Fig. 2.6A cartoon that underscores the heated debate centered on the resolution improvement of global tomographic models based on finite-frequency sestivity kernels vs. simple ray approximation. Authorization to use the cartoon is granted by Yu Jeffrey Gu.

While the ray vs.finite-frequency debate exists (Fig. 2.6), the latter approach is indeed more accurate due to its proper treatments of volumetric interference effects around the geometrical ray paths. Hence, despite being more computationally expensive, chapter 4 centers on the results of finite-frequency inversions.

2.2.4 Inversion

To invert for the velocity structure, equation (2.30)can be re-written into a matrix form

$$\mathbf{Gm} = \mathbf{d}, \tag{2.31}$$

where $\mathbf{G}$ is the 3D finite-frequency kernel, $\mathbf{m}$ is the parameterized model with a length M and $\mathbf{d}$ contains the N measured relative travel time shifts. More discussions regarding model parameterization and regularization schemes will be provided in Chapter 4.

Chapter 3 Crustal Imprints of Precambrian Orogenesis in Western Laurentia

3.1. Introduction

Crustal Low Velocity Zones (LVZs) have been widely reported based on geophysical observations from various disciplines, most notably wide-angle seismic reflection and refraction [*Masson et al.*, 1998; *Nelson et al.*, 1996], ambient noise tomography[*Li et al.*, 2010; *Yang et al.*, 2012], magnetotelluric (MT) [*Unsworth et al.*, 2005; *Wei et al.*, 2001]and earthquakes from teleseismic distances[*Beck and Zandt*, 2002; *Kind et al.*, 1996]. Their formation has been attributed to a number of plausible mechanisms depending on the genesis and evolution of the resident tectonic province[*Li et al.*, 2003; *Ward et al.*, 2013; *Yang et al.*, 2012]. In active orogens such as the Central Andes and the Tibet plateau [*Nelson et al.*, 1996], crustal LVZ could signify the presence of magma body [*Chmielowski et al.*, 1999] or zones of partial melting in thickened crust[*Kind et al.*, 1996; *Yuan et al.*, 1997]. The presence of fluid-filled cracks [*Stern et al.*, 2007]and aquifer layers [*Li et al.*, 2003; *Yang et al.*, 2012] due to metamorphic dehydration, as well as large bodies of serpentinite in the forearc mantle wedge [*Bezacier et al.*, 2010] and serpentine channels atop slabs [*Abers*, 2005], are also capable of reducing the seismic velocities. Under favorable pressure and temperature conditions, these magmatic and metamorphic processes often alter the composition of the protolith and induce low-velocity, felsic granite intrusion into mid-to-upper crustal depths [*Petford et al.*, 2000]. Some of these low-velocity granite bodies have been identified through surface exposures, as in the case of Aletschhorn Mountain, New Zealand[*Mueller*, 1977], while the majority are embedded in the basement rocks resembling those beneath Variscan,

southwest Ireland [*Masson et al.*, 1998] and Guangdong, southeast China [*Chen and Grapes*, 2007].

Crustal LVZs are generally the byproduct of collisional tectonics, manifested either by the subduction of oceanic crust [*Yuan et al.*, 2000] or by continent-continent convergence that forms impressive mountain ranges. A contemporary example of the latter scenario is Himalaya-Karakoram-Tibetan Orogen (HKTO, *St-Onge et al.* [2006]), where LVZs at middle crustal depths effectively delineate the Cenozoic suture zone between the Indian and Eurasian plates. LVZs can also provide forensic evidence for the formation of the Precambrian crust during tectonomagmatic episodes [*James et al.*, 2003]. One prime example is the Trans-Hudson Orogen (THO) in North America. As the largest orogen in the early Proterozoic, the THO extends more than 1000 km from the western Superior province to the Snowbird tectonic zone (STZ) [*Ross et al.*, 1995] and 3000 km along strike from South Dakota to the Ungava Peninsula in northern Quebec [*Corrigan et al.*, 2009]. With comparable scale, duration and characteristics to the Cenzoic HKTO, the THO potentially marks the collisional suture that welded several Precambrian plates together during the assembly of North American craton [*Hoffman*, 1988]. Extensive crustal shortening and thickening, as well as tectonothermal activities of metamorphism and magmatism[*St-Onge et al.*, 2006], have been suggested to take place around the THO in a similar fashion to more recent events surrounding the HKTO. However, a Himalayan-scale LVZ has not been documented to reside beneath the Precambrian crust in the vicinity of the Paleoproterozoic THO. This paper introduces new seismological constraints on the crustal structure beneath central Alberta, a region strongly influenced by the tectonic events surrounding the THO. The region of study (Fig. 3.1a) is a complex assembly largely consisted of the southern Hearne and Rae provinces [*Ross et al.*, 1991]. Bounded by the THO (east) and the STZ (west), a possible suture zone along the Rae province [*Berman et al.*, 2007], the Archean Hearne craton is generally regarded as a broad reworked hinterland [*Lucas et al.*, 1993]

that stretches northeasterly from the foothills of Rockies to Hudson Bay. A large-scale batholith (Wathaman-Chipewyan Batholith) has been discovered in northeastern Hearne province [*Lewry et al.*, 1981]and attributed to the emplacement of crystallized, felsic plutonic rocks in connection with the Proterozoic collision between the Hearne craton and accreted terranes [*Corrigan et al.*, 2009]. In comparison, the tectonic evolution of southwestern STZ and Hearne province, the focus of this study (Fig. 1a), remains debated due to the thick Phanerozoic cover in the Western Canadian Sedimentary Basin (WCSB) [*Shragge et al.*, 2002]. Domain definitions in central Alberta predominantly relied on aeromagnetic signatures and a limited number of drill core samples from shallow depths of the Precambrian crystalline basement [*Ross et al.*, 1991].

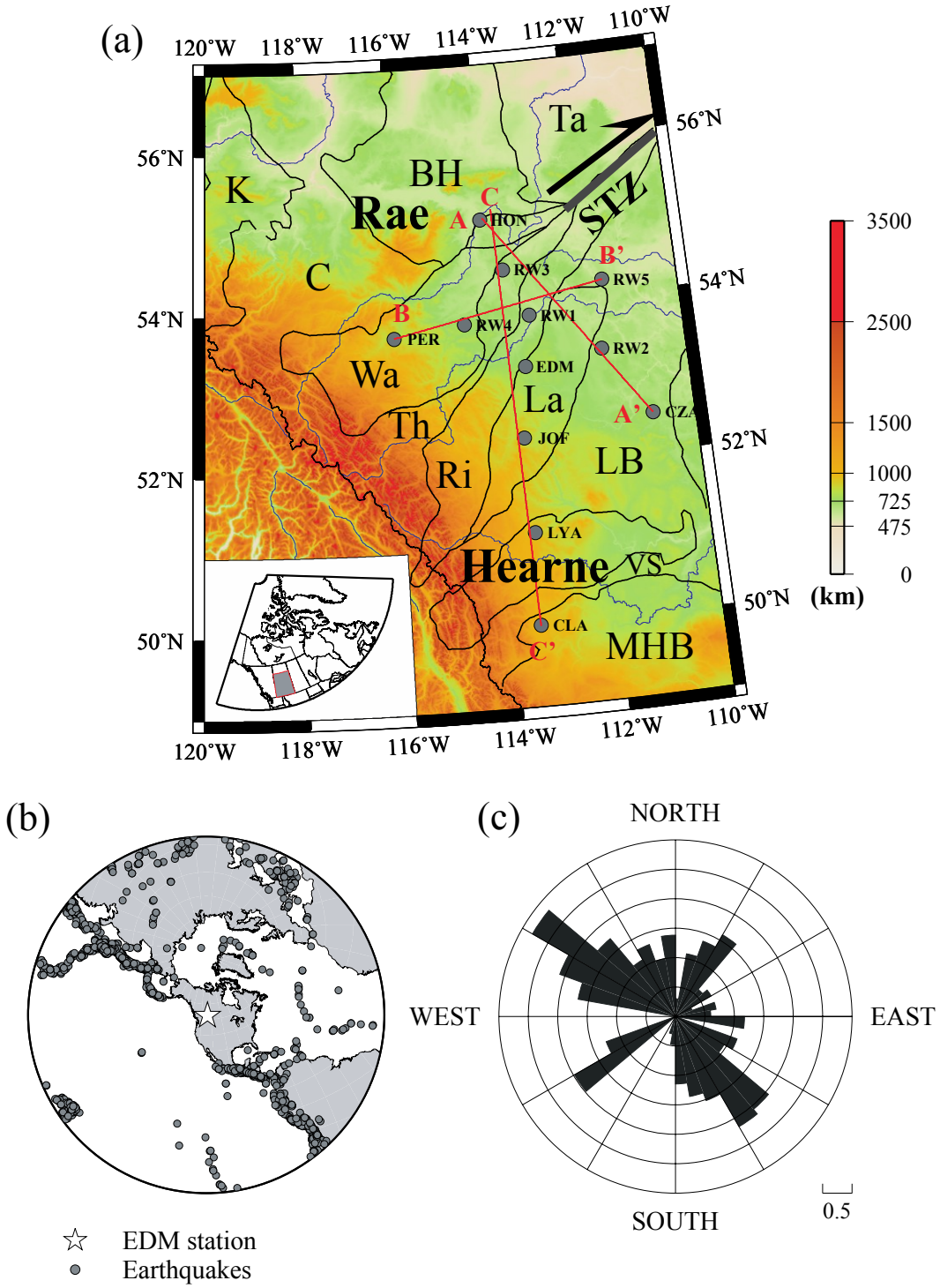

Fig. 3.1The topography map of the study region and station distribution. A-A′, B-B′ and C-C′ are three cross-sections for detailed comparisons of velocity

variations across the array (see Fig. 3.5). LB, Loverna block; La, Lacombe domain; Ri, Rimbey domain; Th, Thorsby domain; Wa, Wabamun domain; MHB, Medicine Hat block; VS, Vulcan structure; BH, Buffalo Head; Ta, Taltson; C, Chinchaga; K, Ksituan; STZ, Snowbird Tectonic Zone(b) Epicenter locations for all events used in this study. The star marks the location of station EDM. (c) A Rose diagram showing the distribution of station azimuths in logarithmic scale.

The understanding of the assembly and evolution of the basement structure in southwestern Laurentia greatly benefited from regional seismic surveys such as deep-sounding reflection experiments (e.g., Central Alberta Transect [*Clowes et al.*, 1996] and Southern Alberta Lithospheric Transect [*Eaton et al.*, 1999], teleseisms [*Eaton and Cassidy*, 1996; *Shragge et al.*, 2002] and controlled source refraction experiments [*Clowes et al.*, 2002]. The success of these surveys are unquestioned, as are the glaring caveats such as 1) limited duration and receiver coverage, 2) linear source-receiver path geometries, and 3) relatively narrow frequency bands. The lack of broad seismic stations prohibits systematic, three-dimensional (3D) constraints on the regional crustal/mantle structures. Consequently, the origin of the STZ and the delamination of the lithospheric root beneath southwestern Laurentia remain debated[*Berman et al.*, 2007; *Flowers et al.*, 2006; *Ross et al.*, 2000; *Shragge et al.*, 2002].

The establishment of Canadian Rockies and Alberta Network (CRANE) [*Gu et al.*, 2011], which began in mid 2006, represents a major advance in seismic monitoring [*Gu et al.*, 2009; *V Stern et al.*, 2013] and analysis [*Gu*, 2010; *Schultz et al.*, 2014] in Alberta. With an average station spacing of ~250 km, CRANE offers semi-uniform, broadband data coverage in central Alberta and enables a 3D survey of its underlying crust and mantle [*Gu et al.*, 2011]. In this study we combine teleseismic data from CRANE and a Canadian National Seismic Network (CNSN) station to provide improved constraints on the crustal structure of southern WCSB. Our new findings offer compelling evidence for a broad mid-

crustal LVZ, which we interpret as a previously undisclosed granitic body, formed by syn-collisional and/or post-collisional magmatic activities during the Proterozoic eon. This orogenic imprint lends new insights into the Proterozoic tectonic evolution of the North American craton.

3.2. Data and method

Our dataset consists of continuous waveforms from EDM, a permanent broadband seismic station from CNSN, and 11 CRANE stations in central and southern Alberta (Fig. 3.1(a)). Since the deployment of the first station in 2006, CRANE has recorded 1500 Mw>5.5 earthquakes in the epicentral distance range of 30 to 90 degree, which is ideal for RF analysis where teleseismic P waves can produce observable S conversions at the base of the crust and upper mantle interfaces[*Beck and Zandt*, 2002; *Cassidy*, 1992; *Owens et al.*, 1984].

Our data processing schemes are similar to those of *Crotwell and Owens* [2005]. After isolating the P wave coda using a time window of 150 sec, we rotate the three component data to the great-circle coordinate system and apply a Butterworth bandpass filter at corner frequencies of 0.3 and 5 Hz. The signal-to-noise ratio (SNR), which is defined by the ratio between the variance of signal window (1 sec before and 5 sec after predicted P arrival time) and that of noise window (105 to 5 sec prior to P), is used as a criterion for quality control; a total of 3874 seismograms with SNR>2 are retained for further RF processing. To estimate RFs we deconvolve the vertical component from radial component seismograms using the water-level deconvolution method[*Clayton and Wiggins*, 1976; *Mangino et al.*, 1993; *Owens et al.*, 1984]. High frequency noise embedded in the RFs is subsequently minimized through a Gaussian filter where the filter width parameter controls the frequency content. To resolve structures at different wavelengths and ensure self-consistency, we subject each RF to Gaussian filters at 0.6 and 2.4 Hz, which correspond to filter width parameters of 1.25 and 5,

respectively. The last step of pre-processing is manual quality control where all RFs are visually inspected; RFs exhibiting high pre-signal noise or abnormally high-amplitude reverberations are eliminated.

For further noise reduction we apply a moveout correction to each trace by aligning its Moho converted phase (Pms) to that of a reference RF (60 degree). The amplitude of RF is normalized by multiplying by the ray-parameter of the reference RF and dividing by the ray-parameter of the RF to be corrected [*Chen and Niu*, 2013]. After time and amplitude correction of all RFs, we stack all aligned RFs to produce a single RF for each station. These stacked RFs are then inverted for shear velocity structures based on the iterative linear inversion approach of *Ammon et al.* [1990] and a starting crustal structure that combines different regional models[*Bouzidi et al.*, 2002; *Eaton and Cassidy*, 1996; *Shragge et al.*, 2002; *Zelt and Ellis*, 1989]. The upper 80 km of the starting model consists of the sedimentary layers (0-3 km) in *Eaton and Cassidy* [1996], which are interpreted from an earlier RF analysis of EDM station. The crystalline basement (4-80 km) is modified after *Bouzidi et al.* [2002], and a lithosphere in the 80-200 km depth range is represented by the AK135 model [*Kennett et al.*, 1995]. It is worth noting that despite our best efforts to construct a reasonable starting model, linear inversions of RFs are inevitably affected by the non-uniqueness of the inversions [*Ammon et al.*, 1990]. Hence, we perform a series of inversions with different starting models obtained by adding 20% cubic velocity perturbation and up to 0.5 km/sec random velocity perturbation [See *Ammon et al.*, 1990] to the initial model. The resultant models are selected based on the fitness of the synthetic waveform to the observed waveform and the characteristics of the models: models fit less than 20 percent of the energy of the observed high frequency waveform and with abnormal features, e.g., unrealistically high average shear velocities (>4 km/sec) in the upper crust are subsequently eliminated. The remaining models are stacked to estimate an average model, which is adopted as the optimal starting model for the RF inversion for each station.

3.3 Results

The stacked RFs, especially the low frequency RFs, exhibit similar waveforms (Fig. 3.2) across the array. Moho conversions (Pms) are clearly identified at ~5 sec after P wave signal. We assume a Poisson ratio of 1.73[*Gu et al.*, 2014, manuscript in preparation], which is a reasonable estimation for this region, and an average crustal P velocity of 6.5 km/sec. The timing of the Moho conversions translates to approximately 38 km depth, which in excellent agreement with the regional average depth obtained by *Bouzidi et al.* [2002](40 km) from seismic reflection profile and *Shragge et al.* [2002](38.5 km) from teleseismic RFs. In addition to Moho conversions, the vast majority of the lower-frequency RFs show a negative phase at 3-4 sec, which suggests zones of velocity reversal above the Moho[*Kumar et al.*, 2002; *Monsalve et al.*, 2013]. In comparison, high frequency RFs exhibit more complex waveforms in general, though. Still, similar downswings can be identified on a number of RFs (e.g. RW4, RW5, JOF). It is also worth noticing that direct P waves at higher frequencies are variably offset from zero at most stations due to the existence of conversions and reverberations within the sedimentary basin[*Cassidy*, 1995; *Sheehan et al.*, 1995]. With the exception of station CLA, Pms on all RFs are visible in the time range of 5-6 sec.

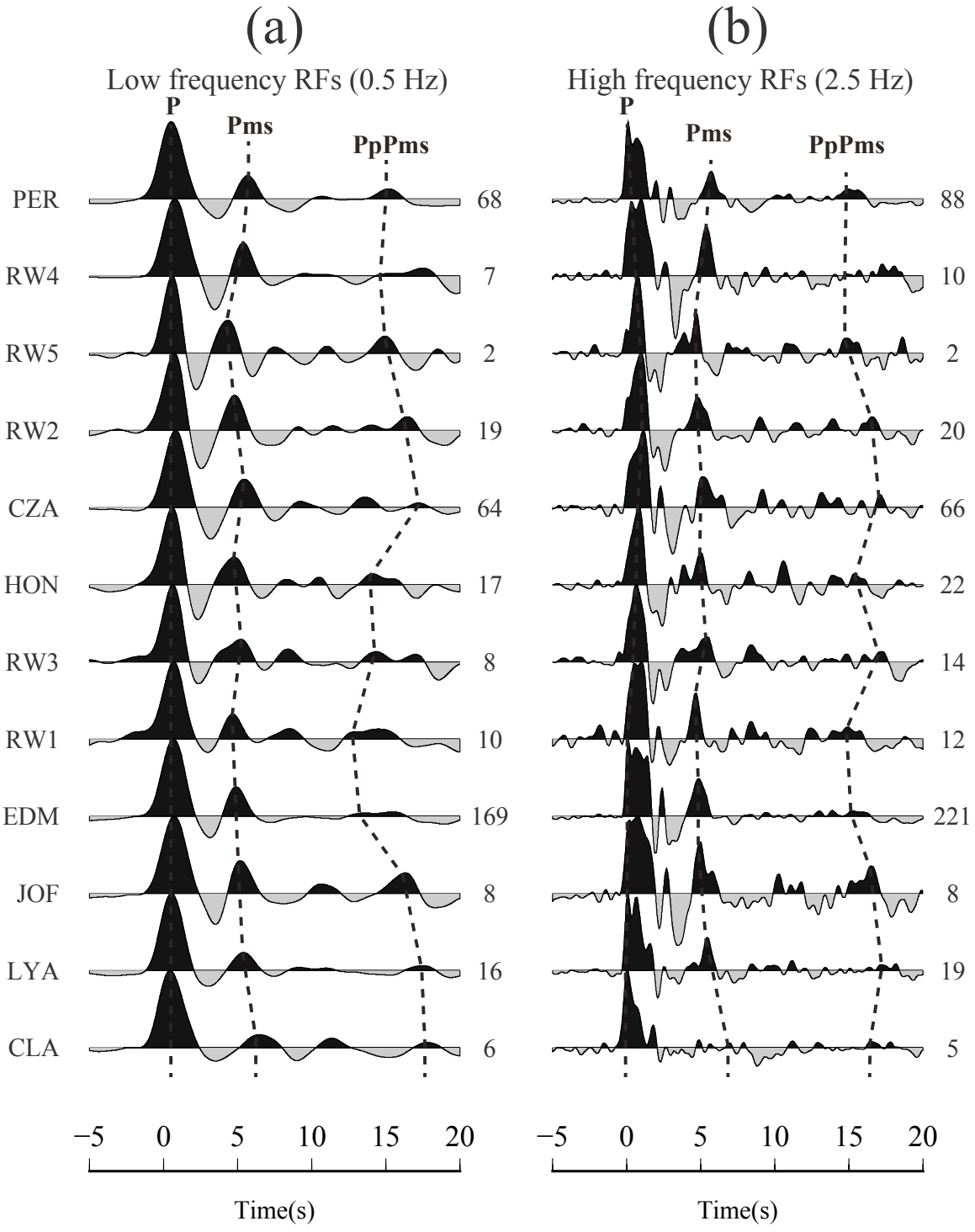

Fig. 3.2Waveforms in the panel (a) and (b) are low (0.6 Hz) and high (2.4 Hz) frequency stacked RFs, respectively. The numbers beside the RFs indicate the

fold of a respective station. The dotted lines mark the direct P, Pms converted phases and PpPms reverberation phases.

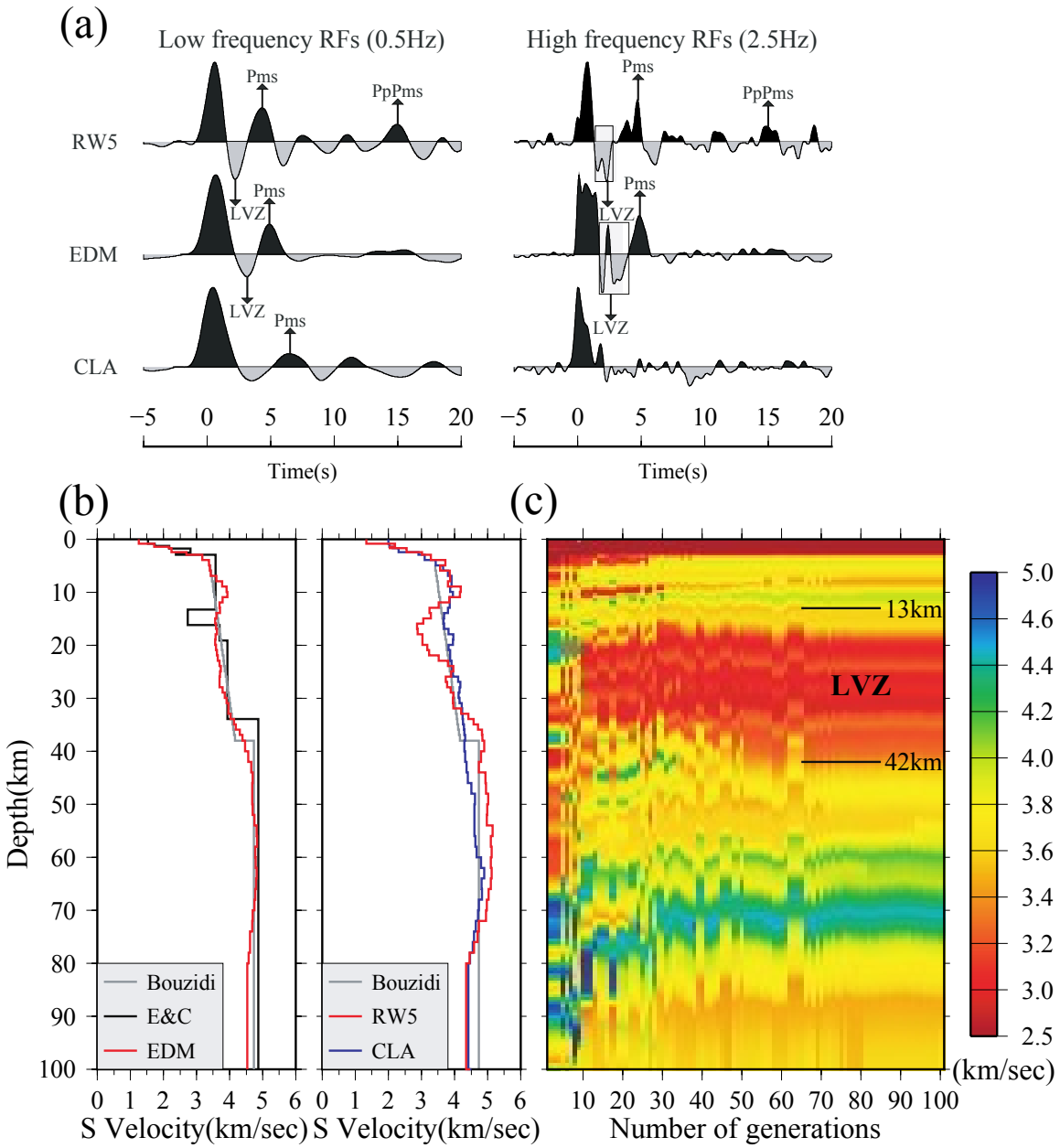

Fig. 3.3Sample RFs showing the waveform characteristics of strong, moderate and weak LVZs. Pms and PpPms and phases related with LVZ features are indicated by arrows. (b) Shear velocity models from this and previous studies.

(c) Non-linear inversion results from station EDM based on genetic algorithm. The x-axis denotes the generation number and the colors represent different velocities.

We classify our RFs dataset into three categories based on the strength of the negative phase preceding Pms. Fig. 3.3a shows a representative RF from each class, among which RW5 exhibits the largest downswing at ~2.2 sec. The Moho conversion and reverberation (PpPms) arrive at ~4.3 sec and ~15.0 sec, respectively, after the P wave arrival. RF from EDM shows a moderate-sized negative phase at ~3.2 sec, followed by a Pms at ~4.9 sec. On the other hand, CLA shows minimal energy at the expected times of ~3.5 sec and Pms at ~6.4 sec is also less prominent than those of RW5 and EDM.

High frequency RFs show similar trends as the low frequency counterparts despite waveform complexity. RFs from RW5 and EDM both contain broad negative phases preceding Pms. In the latter case, distinct arrivals at ~2 sec (negative) and ~2.5 sec (positive) are consistent with the corresponding phases in *Eaton and Cassidy* [1996]. These two arrivals were attributed to top and bottom reflections from a sharp mid-crustal low-velocity layer. The modeling and interpretation of these phases are non-unique but vital for the estimation of the LVZ scale (i.e., width, depth and strength), especially the later arrival that piggy-backs on a strong negative phase. P wave conversions and reverberations at station CLA are exceptionally weak, which suggest relatively smooth, gradational velocity variations in the underlying crust.

The presence of a first-order crustal LVZ beneath central Alberta is substantiated through iterative inversions of RFs. The optimum damping parameter which tradeoffs the RFs fitting results and the model smoothness is chosen based on the turning points of the misfit-roughness norm curves [*Ammon et al.*, 1990]. The RFs from two frequency ranges are weighted equally. The

misfit between observed and synthetic RF decreases with the increasing number of iteration and we stop the iteration while the misfit curve is convergent. The best-fit model for EDM (Fig. 3.3b) shows a broad LVZ at middle-to-lower crustal depths. To define the boundaries of LVZ we fit the depth-velocity curve using a higher order polynomial. The turning points, which translate to zeros in the second derivative, provide effective upper (at 12 km) and lower bounds (at 30+ km) of the LVZ at EDM. The crust-mantle transition is represented by a velocities gradient based on synthetic tests (not shown), resulted from averaging due to the imperfect vertical resolution. The actual Moho depth is more accurately reflected by the mid points of major velocity increases at the base of the crust. Under this criterion, the Moho depth beneath EDM is 38 ± 2 km, which is in excellent agreement with reported values of 38-40 km[*Bouzidi et al.*, 2002; *French et al.*, 2009]. Moho depths from all three studies are approximately 4 km thicker than the proposed model by *Eaton and Cassidy* [1996](from here, EC96).

The most significant difference between EC96 and our model of EDM (see Fig. 3.3) is the scale of the LVZ. In the former study, a thin LVZ was identified between 13 and 16 km with an average shear velocity of ~2.9 km/sec. This is inconsistent with our model LVZ, which resides between ~12 km and 30 km depth with an average shear velocity of ~3.65 km/sec. The non-uniqueness of the RF inversions contributes to the difference in the models. Discriminating between these two models requires associating the interpretation of the LVZ features to a regional tectonic model as will be detailed in the discussion. The structures beneath stations RW5 and CLA highlight the two end-member models of the middle crust in Alberta. The crust beneath station RW5 (Fig. 3.3(b)) contains a strong LVZ in the depth range of 12-25 km and a relatively sharp Moho interface at 36 km depth. The minimum shear velocity is 0.35 km/sec slower than that beneath EDM. The crust beneath CLA is nearly polar opposite, where velocities increase monotonically with depth and only a slight velocity reverse resides at ~16 km depth. The Moho is also much less well defined.

Non-uniqueness is a well-documented pitfall of linear inversion of RFs. The solution of the inverse problem can be affected by the starting model [*Ammon et al.*, 1990]: an improper choice of starting model may steer the solution toward a local minimum. In addition to performing a series of inversions with perturbed starting models[*Ammon et al.*, 1990; *Mangino et al.*, 1993; *Wilde-Piórko and Grad*, 2002], we use genetic algorithm (GA) [*Shibutani et al.*, 1996] to perform a global solution search in the model space. This method simulates the gene evolution process of biological systems and solves non-linear inverse problems via a complete global optimization [*Sambridge and Drijkoningen*, 1992]. The emergence (at 10th generation) and stabilization of a strong middle crustal LVZ (Fig. 3.3c) is clearly demonstrated in the case of EDM. Despite minor differences (e.g., a slightly lower average velocity and deeper LVZ depth), the resulting optimization-based model clearly requires a LVZ to fit the observed RFs. The consistency between two different inversion techniques increases our confidence in the results of the linear inversions.

The results of waveform inversions for all available stations in central Alberta are superimposed on a regional heat flow map [*Majorowicz and Grasby*, 2010] and summarized in Fig. 3.4.All stations exhibit satisfactory results where at least 90% of the energy of the observed P-to-S converted waveforms can be recovered using the final models. The depth and strength of the LVZ vary significantly in central Alberta, as indicated by the cross-sections (Fig. 3.5, also see Fig. 3.1a). Along the southeast trending A-A' profile (Fig. 3.5a) from HON to CZA, the LVZ show a southeast dipping morphology. The apparent difference in LVZ thickness, obtained by taking the depth range between 3.5 km/sec contour lines, between RW1 (8 km) and RW2 (12 km) marks an effective transition from shallow to deep LVZ initiation depths. Along the B-B' profile (Fig. 3.5b), LVZ is weak beneath PER station and increases its significance toward the east. Along north-south orientation profile (Fig. 3.5c) the mid-crustal LVZ is the most pronounced beneath HON but it gradually weakens toward central Alberta (EDM

and JOF). It is worth noting that the large negative phase preceding Pms for station JOF is poorly fitted by the inversion. This implies that the scale of the LVZ in southern central Alberta may be slightly underestimated. On average, the LVZ is best observed in the depth range of 12-27 km with a minimum velocity of 3.4 km/sec at 17 km (Fig. 3.5d).

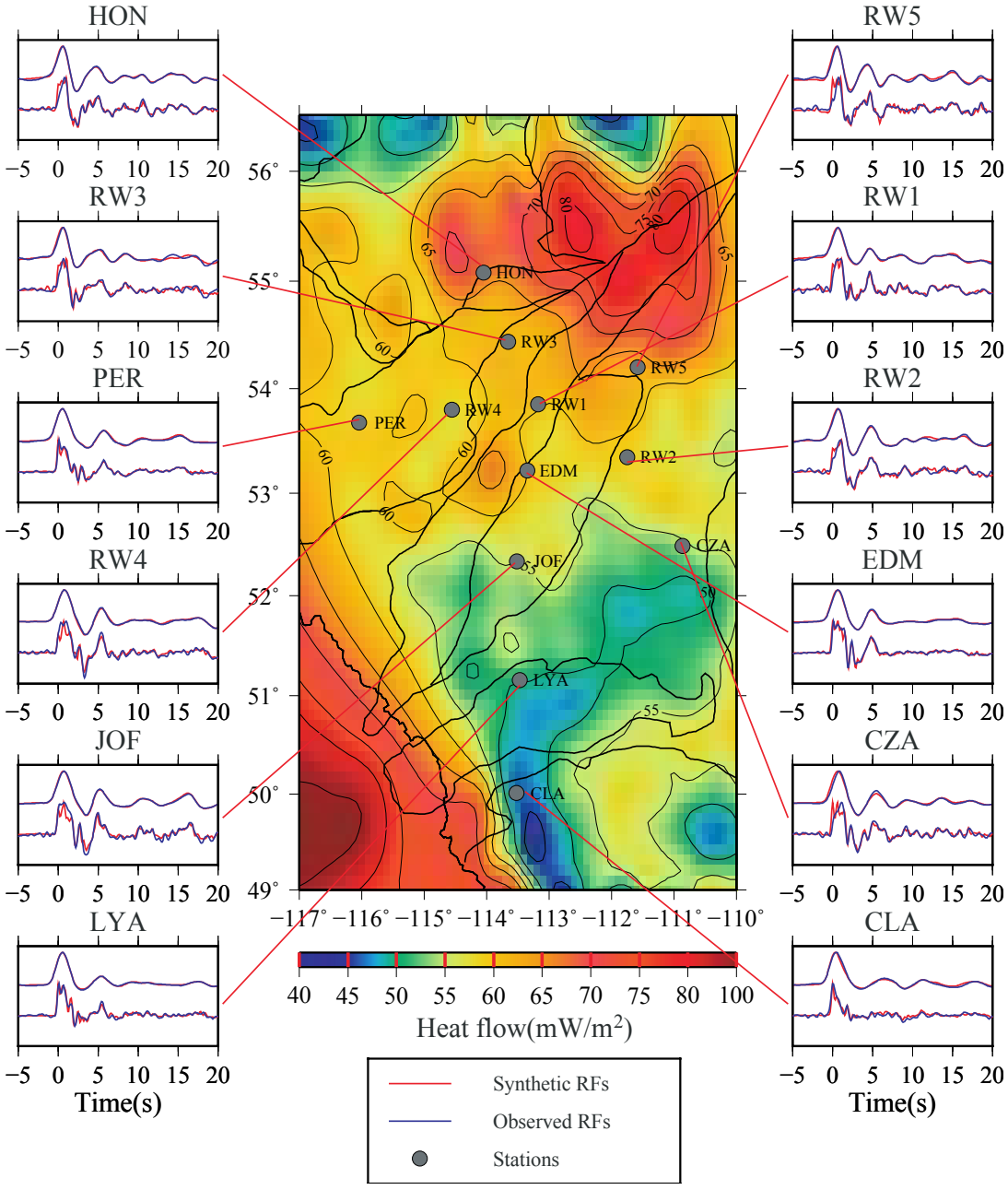

Fig. 3.4Waveform fitting results of all stations displayed on a regional heat flow map. Stations with prominent LVZs are generally located within zones of enhanced heat flow.

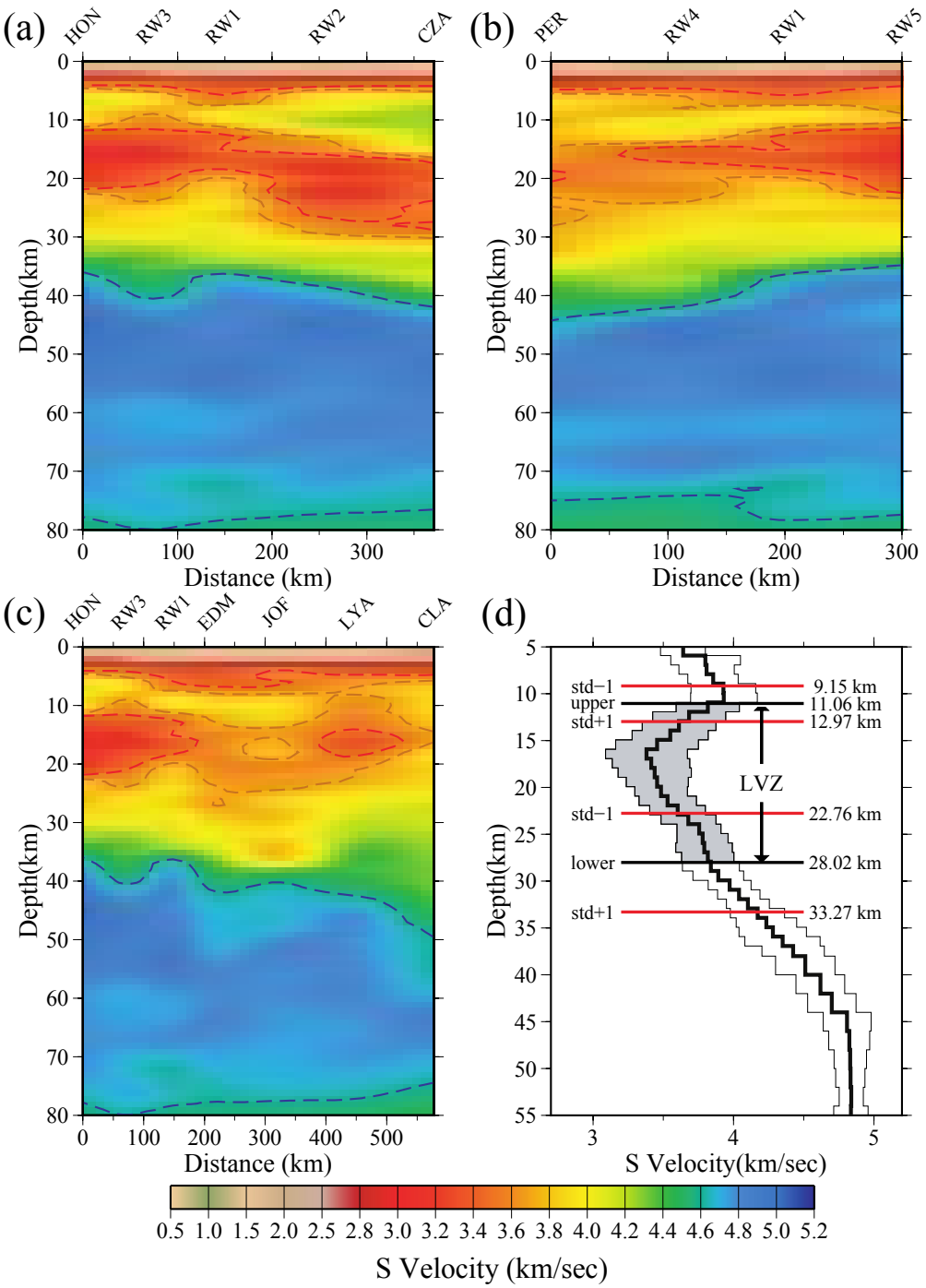

Fig. 3.5Panels (a), (b) and (c) demonstrate crustal structures beneath cross-sections A-A′, B-B′ and C-C′, respectively. The color-coded LVZ distribution shows shear velocities ranging from 2.5 to 3.7 km/sec in the middle crust.

The lower crustal velocities are represented by yellow to green colors ranging from 3.7 to 4.7 km/sec. Upper mantle velocities in excess of 4.7 km/sec are indicated by dark blue colors. The blue dashed line marks the Moho depth based on a threshold Vs = 4.6 km/sec. The red solid lines and orange dashed lines mark 3.5 km/sec and 3.7 km/sec contours, respectively. (d) The averaged shear velocity model for the entire array. The shaded region shows the extent of LVZ. The thick black lines mark the upper and lower boundary of LVZ and their one standard deviation is denoted by the thick red lines. Thin black lines along the profile indicate one standard deviation of the average velocity at each depth.

The thickness and velocity variations of the LVZ are demonstrated on the regionally tectonic map in Fig. 3.6.The most prominent LVZs, as indicated by a shear velocity <3.5 km/sec and a thickness value larger than 10 km, are observed at HON, RW2, RW3, RW4 and RW5 in the vicinity of the STZ and Proterozoic magmatic arcs. The remaining stations in central Alberta (EDM, PER, JOF) feature a LVZ with shear velocities greater than 3.6 km/sec and thicknesses in excess of 15 km. The southernmost station, CLA, which is located on the Archean crust, shows an anomalously thin LVZ with shear velocities of ~3.5 km/sec. Combining the cross-sections and the lateral variations of the LVZs, it is reasonable to suggest that mid-crustal LVZs are well developed in central Alberta with an average thickness ~12 km and a lateral span up to 200 km.

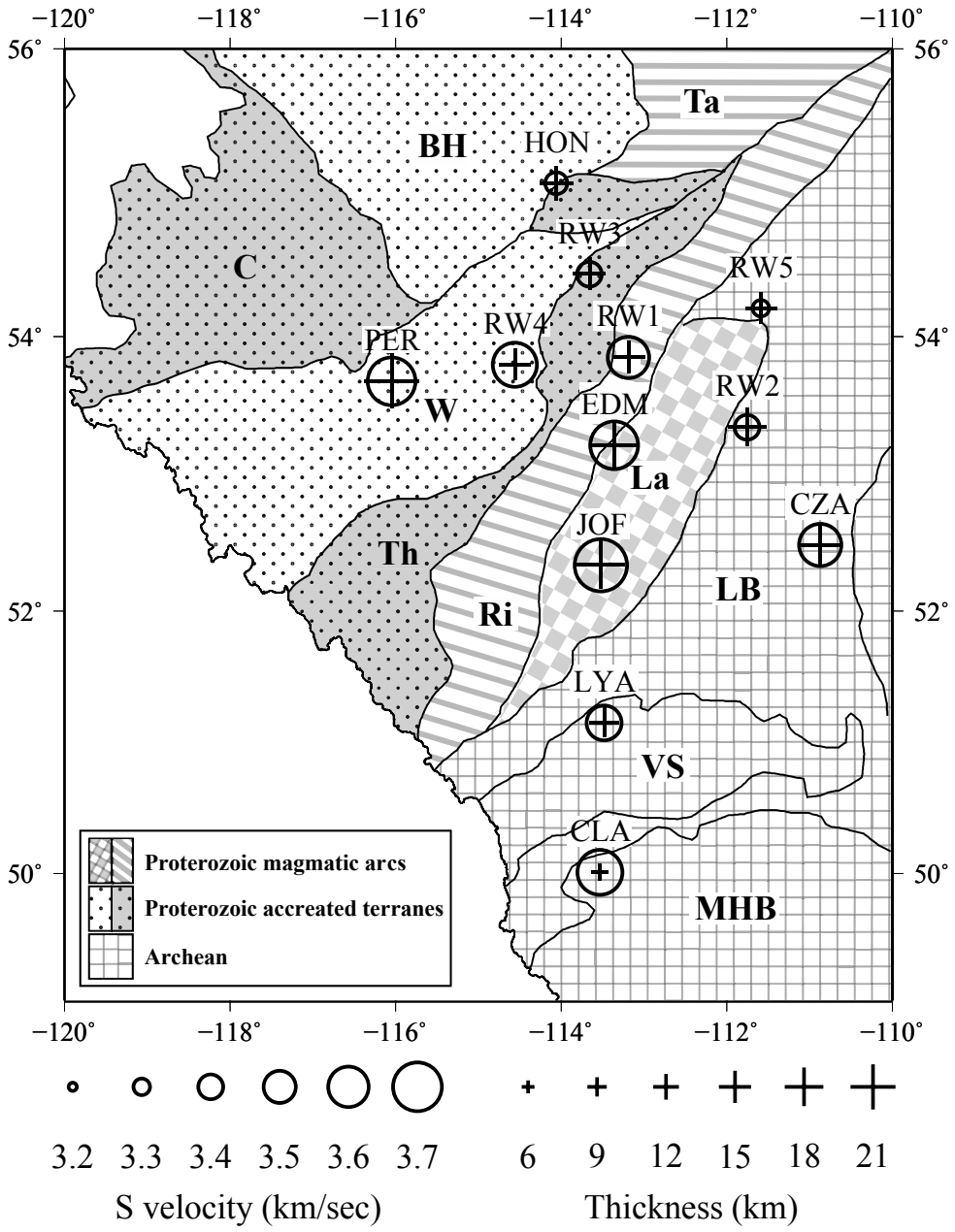

Fig. 3.6Variations of LVZ velocity and thickness superimposed on a regional tectonic domain map[*Ross et al.*, 1991]. The velocities are obtained by averaging the velocities between the upper and lower boundaries of the LVZ. The circles indicate the varied LVZ velocities and the plus symbols show the change in LVZ thickness. LB, Loverna block; La, Lacombe domain; Ri, Rimbey domain; Th,

Thorsby domain; W, Wabamun domain; MHB, Medicine Hat block; VS, Vulcan structure; BH, Buffalo Head; Ta, Taltson; C, Chinchaga; K, Ksituan.

3.4. Discussion

Crustal LVZs have been observed in several tectonically active or Cretaceous orogens, such as the Tibet Plateau [*Kind et al.*, 1996], Alps (Mueller [*Mueller and Landisman*, 1966], Andes [*Schmitz et al.*, 1997] and Apennines [*Ökeler et al., 2009*], where LVZ are characterized by continuous lateral extensions spanning hundreds of kilometers. In contrast, cratons consisting of old and stable continental crusts [*Grotzinger and Jordan*, 2010] are nearly unaffected by tectonothermal events since the Precambrian and generally exhibit little geophysical or geological signatures of a thick, definitive LVZ. An exception is the North China craton, where LVZ has been documented as two westward dipping layers and interpreted as the remnant of subducted upper-to-middle continental crust beneath the Ordos Basin [*Zheng et al.*, 2009]. In comparison with the crustal structure beneath the North China craton, our observed LVZ in central Alberta is distinctively thicker (by 10+ km) and wider (by ~200 km), more resembling the scale of the LVZ beneath active tectonic regions. Despite the age difference between young orogens and the Precambrian central Alberta, the presence of crustal LVZs with comparable strengths and scales in both tectonic provinces offers important clues about the possible links in their genesis. The remainder of this section will review and differentiate between four candidate mechanisms for the generation of crustal LVZs beneath the Proterozoic Alberta basin, which include 1) partial melting of the crust[*Kind et al.*, 1996; *Nelson et al.*, 1996]; 2) serpentinite coupled with subduction process [*Eaton et al.*, 1999; *Li et al.*, 2003]; 3) anisotropy [*Zorin et al.*, 2002] and 4) the existence and intrusion of crystallized granitic bodies [*Masson et al.*, 1998].

In the first scenario, partial melting in the crust has been revealed by multi-disciplinary studies of the Tibet plateau, where the ongoing collision between the Indian and Eurasia plates triggers massive magmatic activities that are manifested in both surface geology and crustal structure. The LVZ covers most of the Tibetan middle crust at the depths between 20 and 40 km [*Yang et al.*, 2012]. Its existence has been attributed to crustal thickening [*Nelson et al.*, 1996] and the presence of aqueous fluids or high H_2O contents [*Caldwell et al.*, 2009; *Rapine et al.*, 2003] all of which could effectively lower the melting temperature, initiate the partial melting process and significantly decrease seismic wave velocity [*Sato et al.*, 1989]. In theory, the presence of partial melts would offer a simple explanation for the crustal LVZ, including the observed anomaly beneath central Alberta. However, regional electromagnetic surveys [*Boerner et al.*, 2000] and seismic reflection explorations [*Bouzidi et al.*, 2002; *Lemieux et al.*, 2000; *Ross et al.*, 1995] have discovered no evidence of a potential partial melting zone. Major tectonic events, e.g., continent-continent collision and post-collisional magmatism [*Ross et al.*, 2000; *Ross et al.*, 1995; *Ross et al.*, 1991], occurred during the assembly of western Canadian Shield in the Proterozoic eon. Without significant reactivation of the basement crust in the Phanerozoic eon [*Ross and Eaton*, 1999], residual melt and its thermal imprints are unlikely to survive over one billion years of lithosphere cooling in western Laurentia[*Ross*, 2002].

An alternative explanation is the presence of serpentinites, which can originate either from subducted oceanic crust containing subducted abyssal serpentinites or serpentinized layer formed at the subduction plane interface [*Deschamps et al.*, 2013]. *Eaton and Cassidy* [1996]interpreted a thin, 3-km-thick LVZ in central Alberta as a serpentinized peridotite layer associated with obducted oceanic plate due to its comparable shear velocity (2.9 ± 0.2 km/sec) with that of serpentinite (2.79 ± 0.44 km/sec) at 15 km depth. In comparison with this earlier model, the observed LVZ in our study is 15 km thicker and 0.7 km/sec faster. Aside from the velocity mismatch, the broad spatial scale of LVZ (15 km ×

200 km) is inconsistent with that of a localized serpentinite layer[*Eaton and Cassidy*, 1996]. Perhaps more importantly, serpentinite breaks down at temperatures above 600-700 °C [*Deschamps et al.*, 2013] while geochemical evidence from Chipman mafic dikes reveals temperatures in excess of 750 °C along the STZ ca. 1.9 Ga[*Flowers et al.*, 2006]. Serpentinite is unlikely to remain stable during craton evolution since its formation from the Paleoproterozoic subduction.

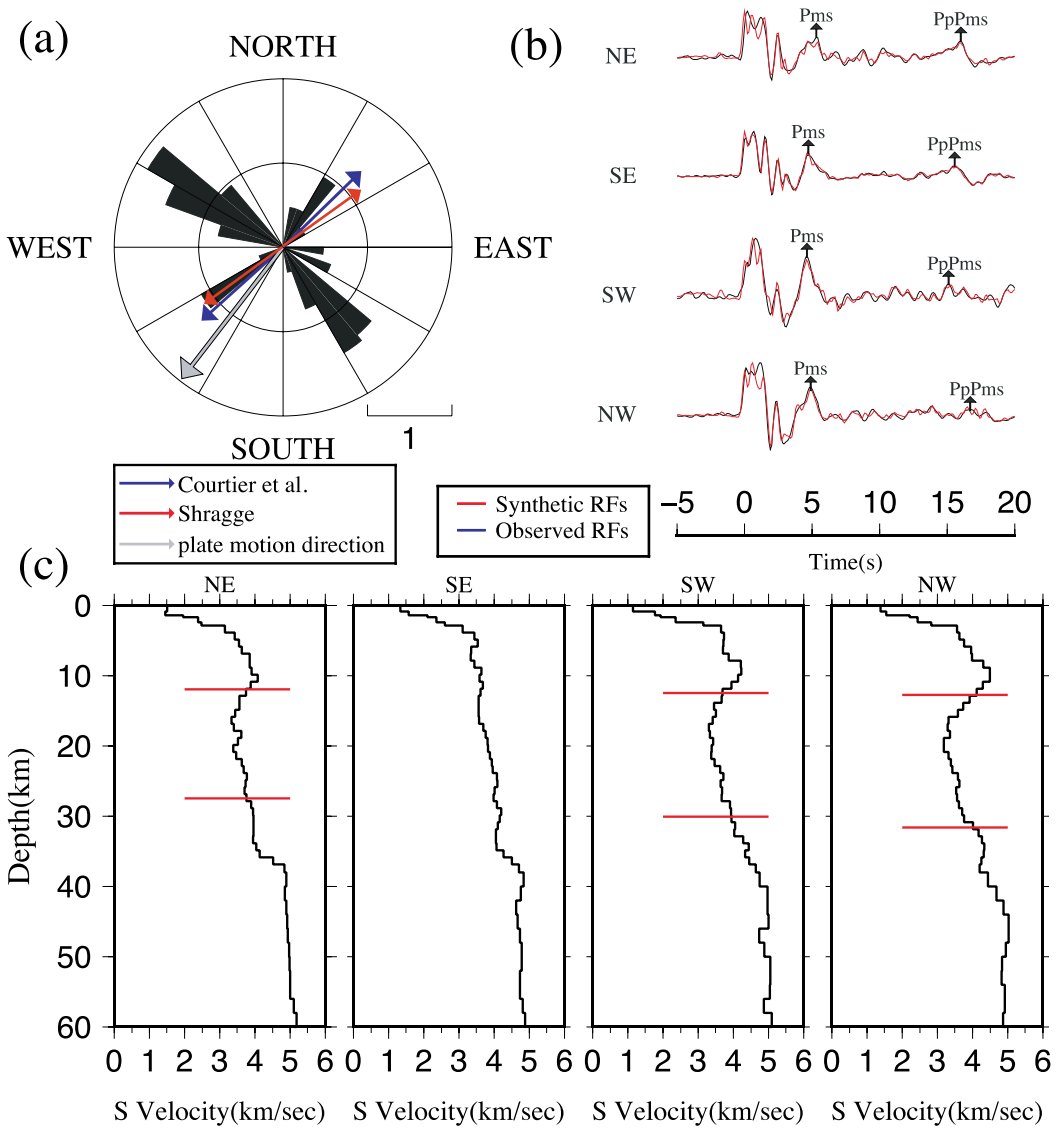

Fig. 3.7(a) A rose diagram showing the back-azimuths of data recorded by station EDM in logorithmic scale. The red and blue arrows show the shear wave splitting measurements by *Shragge et al.* [2002] and *Courtier et al.* [2010], respectively, beneath the station EDM. The grey arrow indicates the plate motion direction. (b) Observed and simulated RFs for four back-azimuth quadrants for station EDM. (c) The inverted models for quadrants showing in (b). LVZs are evident in three out of four back-azimuth quadrants; the lone exception is along the SE direction. The red lines mark the boundaries of LVZ.

Anisotropy has also been cited as a possible mechanism of the LVZs [*Zorin et al.*, 2002]as the re-orientation of minerals under regional stress field could reduce the seismic velocity in certain orientations. Earlier studies of seismic anisotropy have suggested dominant (fast) orientations of 33-43 degrees in the mantle (Fig. 3.7a,*Currie et al.* [2004]; *Shragge et al.*, [2002];*Courtier et al.* [2010]) beneath Alberta. These values are in rough alignment with the present-day plate motion (see Fig. 3.7a). While our source-receiver paths are mainly oriented in northwest-southeast direction, which coincide with the expected slow shear wave direction, the consistent waveforms (Fig. 3.7b) as well as inverted models (Fig. 3.7c) based on stacked RFs from four quadrants show little, if any, directional dependence of crustal velocities. Similar results are obtained for other stations in the region of study. In other words, anisotropy should not play a major role for the presence of the observed mid-crustal LVZ.

Based on evidence from regional heat flow, observed seismic velocities and tectonic history, we propose that a regional scale granitic body formed in a compressional tectonics setting is the most probable explanation for the observed LVZ. The heat flow in central and southern Alberta (see Fig. 3.4) is, to first order, spatially correlated with the LVZ strength. Regions underlain by a strong LVZ generally reside in high heat flow (>60 mW/m^2) regions associated with accreted terranes and magmatic arcs, while two stations without distinctive LVZ signatures (LYA and CLA) are both confined within an anomalously low heat flow (<50 mW/m^2) zone in the Archean southern Alberta. This trend is consistent with earlier reports of increased heat flow from Archean craton to surrounding younger Precambrian terrains[*Ballard and Pollack*, 1987; *Rudnick and Fountain*, 1995]. Variable radiogenic heat generation in different tectonic provinces likely contributes to the observed heat flow variation in Alberta [*Bachu*, 1993]. It has long been suggested that the spatial variation of heat flow, as manifested by regional thermal anomalies, could reflect the variable amount of granite intrusion into the basement [*Bachu*, 1988]. This hypothesis is supported by the abundant

granite-granitoids discovered in the drill core samples along the Rimbey magmatic arc [*Ross et al.*, 1991].Granite contains a greater amount of heat producing elements (e.g. U, Th, K) in comparison with the average continental crust [*Turcotte and Schubert*, 2014], the associating radioactive decayleads to an increasedheat generation in the crust as well as an enhanced heat flow.As a result, a crust model containing a granite-rich layer provides a simple explanation both for the observed heat flow variation and for the LVZ in Central Alberta. A statistical analysis of the heat flow with the average crustal velocities beneath each station site shows an overall correlation coefficient of 0.79 (Fig. 3.8).Highly correlated crustal velocities and heat flow values would suggest that a common mechanism involving granite might be responsible for both observations.

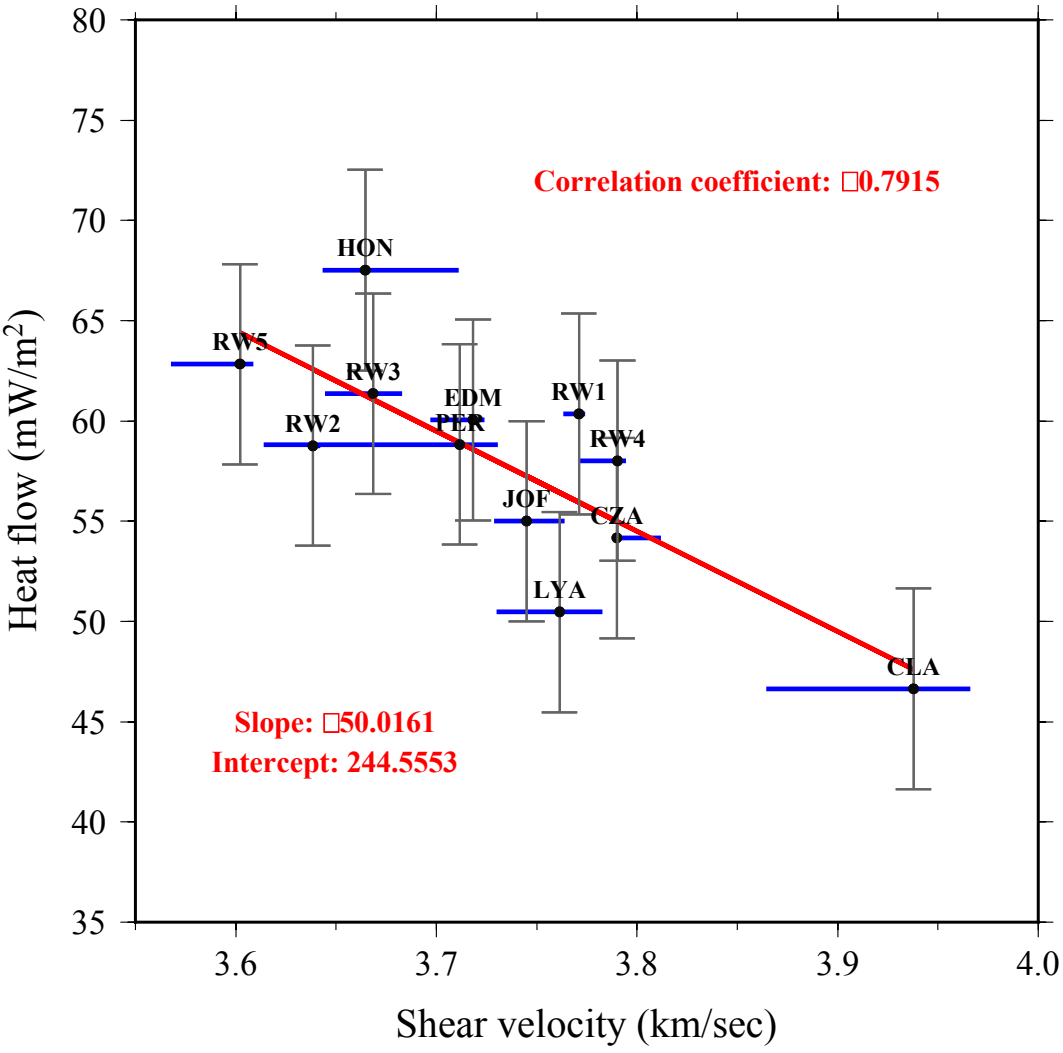

Fig. 3.8The correlation between heat flow[*Majorowicz and Grasby*, 2010] and average crustal shear velocity. The red line shows the computed linear regression. The blue line at each data point represents the range of average shear velocity for inverted models from 1 to 20 iterations. Grey line shows the error of heat flow.

The hypothesis of granite intrusion is supported by the average shear velocity (3.45 ± 0.30 km/sec) of the observed mid-crustal LVZ. Based on the average reported compressional velocities of crustal rocks (e.g., *Christensen and Mooney* [1995]), we obtain the average shear velocities of granite-granodiorite at 15 and 20 km depths of 3.599 km/sec and 3.593 km/sec, respectively, assuming an average Poisson ratio of 0.25. These values are well within the uncertainties of average velocity of the observed LVZ (see Fig. 3.5d) in this study, a robust measurement that is only marginally affected by the non-uniqueness of inversions. In other words, a model containing a granitic mid-crustal LVZ is favored by the observed seismic velocities in western Laurentia.

The entrapment of Hearne province [*Ross et al.*, 2000] within the southern WCSB [*Ross et al.*, 1995] during the Paleoproterozoic eon provides a rich tectonic environment for the formation of a granite-rich crustal layer. It has been long documented that the Hearne province was bounded by the coeval subduction of oceanic lithosphere along the STZ and continental lithosphere in the Trans-Hudson orogen [*Ross et al.*, 2000; *Ross et al.*, 1995]. The STZ is a NE trending gravity and magnetic anomaly [*Flowers et al.*, 2006], splitting the western Churchill province into the Hearne and Rae domains. The role of the STZ during the assembly of Churchill province remains debated, as it has been interpreted both as an intercontinental suture [*Berman et al.*, 2007; *Hoffman*, 1988; *Ross et al.*, 2000] and as an intracontinental fault/shear zone[*Hanmer et al.*, 1995; *Lewry et al.*, 1981]. In the former (and more accepted) hypothesis, the intercontinental origin indicates a ca. 1.9 Ga collisional event between the Hearne and Rae provinces [*Berman et al.*, 2007]. Central Alberta covers the southern extension of the STZ, where the Thorsby domain was formed as a marginal basin in the Proterozoic eon and eventually subducted beneath the Hearne province due to basin closure [*Ross et al.*, 2000]. During subduction, the descending oceanic crust underwent dehydration, which triggered partial melting within the mantle wedge. Magma would propagate upward and underplate the lower crust, as is

evident in the Cree Lake Zone [*Annesley et al.*, 2005]and southern Alberta [*Clowes et al.*, 2002]. The magma underplating causes large-scale mid-crustal melting, which produces leucogranite discovered in Rimbey magmatic belt [*Ross et al.*, 1991]. To the east of the Hearne province, the THO collided with Hearne ca. 1.80 Ga and initiated extensive NW-SE crustal shorting, thickening and deformation. The syn-collisonal or post-collisional tectonothermal activities associated with crustal thickening significantly increased the radiogenic heat production in the crust, which could elevate the temperature sufficiently to cause the anatexis process at mid-to-upper crustal depths [*Chen and Grapes*, 2007] and induce granitic intrusions. Lithosphere delamination due to shortened and gravitationally unstable mantle lithosphere [*Ross et al.*, 2000] may further enhance crustal melting. In the event of lithosphere delamination [*Ross et al.*, 2000], increased mantle heat flux could induce partial melting near the base of the crust and enlarge the volume of the partial melting zone.

Orogeny with ongoing subduction and extensive LVZ in central Andes presents a modern analogy for the Paleoproterozoic events in central Alberta. A regional mid-crustal low-velocity layer has been observed beneath broad areas in central Andes, which was interpreted as brittle/ductile transition between the upper and lower crust in the presence of partial melt [*Beck and Zandt*, 2002]. The crust beneath the mountain belt exhibits lower-than-average velocities and a felsic granite composition[*Beck and Zandt*, 2002; *Zandt et al.*, 1994]. The similarity between the tectonic settings of the Hearne province and Andes, despite the apparent age difference, favors a common model of tectonic evolution with episodes of subduction, crustal shortening and elevation, as well as a possible delamination of the mantle root.

(a)

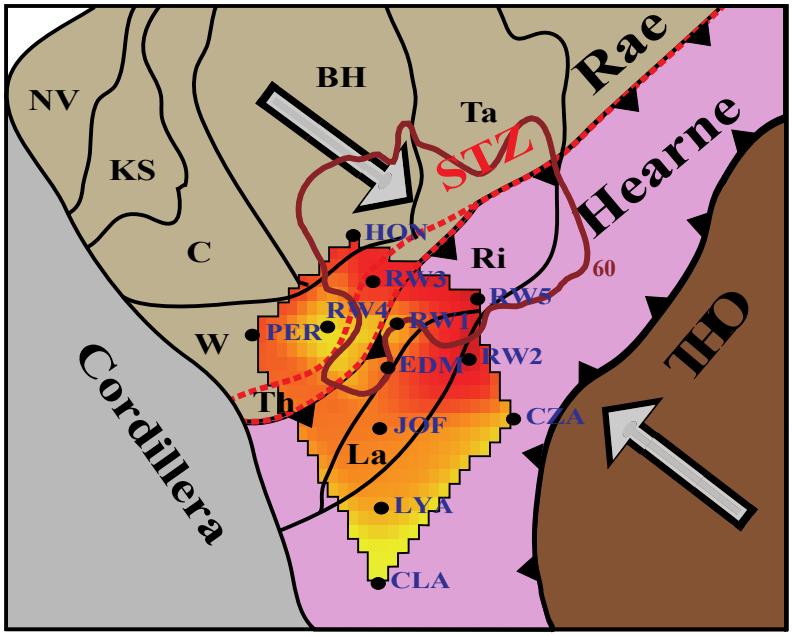

Shear velocity (km/sec)

Thrust fault ● station

Snowbird tectonic zone

60 mW/m² heat flow contour

(b)

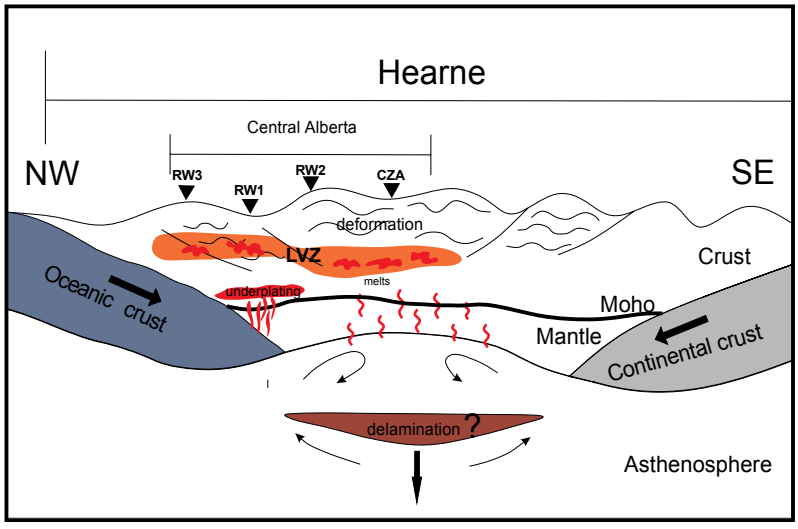

Fig. 3.9(a) A schematic regional tectonic map showing a possible tectonic framework that facilitates the generation of a crustal LVZ. The average shear velocities for all stations are displayed using a color map. The 60 mW/m^2 heat flow contour highlights the overlap between high heat flow regions and areas of below-average shear velocities. (b) A schematic diagram to demonstrate major tectonic events including the subuction of oceanic crust, collisional crustal thickening and lithosphere delamination; all three mechanisms could contribute to the presence of crustal LVZ in Alberta. The vertical scale of the crust been exaggerated for a better visual inspection.

In summary, the presence of granitic body within the middle crust beneath central Alberta is favored by 1) heat flow and crustal shear velocity correlation, 2) comparable average velocity of LVZ with that of granite in the middle crust and 3) ideal dual-subduction tectonic setting (Fig. 3.9a) for the generation of regional scale partial melting. The schematic diagram (Fig. 3.9b) summarizes the tectonic processes leading to the formation of LVZ. The middle crust underwent partial melting due to 1) magma and underplating initiated by the subduction of the oceanic plates; 2) increased heat generation due to the thickened crust, and 3) protracted heating after the delamination of mantle lithosphere. The region of partial molten zone could be further enlarged by intrusion of melts into the country rock, or even through the process of decompression melting in response to lithosphere exhumation. During the millions of years of lithosphere cooling since Precambrian, the molten crust crystallizes to solid rocks and eventually formed a granite-rich mid-crustal LVZ.

3.5. Conclusions

Orogens are the attestations of the most striking collisional events in the Earths tectonic history. The resultant crustal deformation, which is generally recognizable from magnificent mountain ranges (e.g., Himalayan mountain belt),

can cause partial melting and the formation of intrusive bodies with a granitic composition. Over 1.7 billion years ago, Himalayan-scale orogenesis and crustal deformation mostly likely transpired near the THO, a Precambrian orogen with residual imprints of crustal magmatism in the form of LVZ in spite of erosion and subsequent tectonic events. The detailed composition of the crustal LVZ remains speculative, though its existence and scale (200-km wide, 10-km thick) beneath the southern WCSB are strongly supported by the heat flow observations, the elastic properties of granite, and inversions of RFs computed from thousands of teleseismic events in this study. The presence of LVZ will undoubtedly lend new insights on the early assembly and evolution of Laurentia.

Chapter 4 Finite-Frequency Traveltime Tomography of Lithospheric and Upper Mantle Structures Beneath the Cordillera-Craton Transition in Southwestern Canada

4.1 Introduction

Alberta basin is a foreland basin east of the Canadian Rockies with an origin closely related to the orogenic deformation of Cordillera [*Porter et al.*, 1982]. The topographic relief from Canadian Rockies to the Alberta sedimentary basin is as much as 3 km, which is the surface manifestation of the interaction between the North American craton and adjacent younger lithospheric plates Price[*Price*, 1994]. Beneath the surface layer, much of the tectonic evolution history of the Cordillera-craton transition can be inferred from the present state of the crust and mantle lithosphere. The subsurface crust is strongly deformed, as evidenced by the thrust and fold belts within the Cordillera[*Price*, 1981; *Price and Mountjoy*, 1970], after recent (Mesozoic) plate convergence. The upper mantle holds different signatures from the crust, such as distinctive seismic velocities, for the Phanerozoic Cordillera and Precambrian craton. Studies of the upper mantle structure of western Canada have been conducted since the 1970s in both regional and continental scales [*Mercier et al.*, 2009]. In these studies, surface and body-wave tomography have been instrumental in formulating the structures of the crust and mantle, which include 1) contrasting velocities beneath craton (high) and Cordillera (low) [*Van Der Lee and Frederiksen*, 2005]; 2) a relatively sharp Cordillera-to-craton transition [*Mercier et al.*, 2009], and 3) relatively well preserved lithosphere mantle beneath the Hearne craton [*Shragge et al.*, 2002].

Though some consensus have been reached among different research groups, debates on the aforementioned observations and subsequent interpretations remain. The boundary zone where the Cordillera transforms to the craton in northern Cordillera has been suggested to coincide with the Cordilleran deformation front (CDF) [*Mercier et al.*, 2009], though others favor a more westerly position toward the Cordillera [*Frederiksen et al.*, 2001; *Frederiksen et al.*, 1998]. The fate of the lithosphere mantle is also the key issue of contention. *Ross et al.* [2000]proposed a tectonic entrapment model of the Archean Hearne province, where the lithospheric keel is suggested to be delaminated due to the gravitational instability of the thickened lithosphere. However, the body-wave tomography of the southern Alberta upper mantle [*Shragge et al.*, 2002] showed continuous high P-wave velocities extending to, at the minimum, a depths of 200-250 km, suggesting a relatively intact lithospheremantle that was not severely deformed during the Proterozoic subduction and orogenesis.

The aforementioned discrepancies are generally the consequence of interpretations based on geophysical data with limited coverage and sensitivities. Earlier studies are highly relied upon temporal seismic array deployments, e.g. Canadian Northwest Experiment (CANOE) array[*Mercier et al.*, 2009] and a limited number of portable stations[*Shragge et al.*, 2002], which suffered from linear station geometry as well as short deployment durations and narrow frequency ranges. Insufficient resolving power of the ray-theory based tomographic techniques further contributes to the uncertainties in the interpretations. This study takes the advantages of three years of continuous broadband seismic recordings from the Canadian Rockies and Alberta Network (CRANE) and the excellent resolving power of finite-frequency tomographic method. We aim to improve the data resolution on the Cordillera-craton transition in the upper mantle and the craton structure beneath the southwestern Canadian Shield. By inverting the relative traveltime difference for P waves between all available station pairs, we are able to resolve P-velocity structures down to 400-

km in central-southern Alberta and southeastern British Columbia. Our results provide new evidence for a locally sharp P-wave velocity gradient beneath the southern Canadian Rockies and two Archean-aged lithospheric plates under Hearne and MHB.

4.2. Data and method

4.2.1 Station and Event Distributions

Eleven stations from CRANE play the key role in resolving the subsurface structure in central Alberta. The most useful data were recorded between 2006 and 2008, during which the transportable array (TA) from the USArray experiment swept across Montana and North Dakota (Fig. 4.1) directly south of Alberta. The dense station deployment along the Canada-US border enable uniform correlations between stations, which provide strong data sensitivities in the southernmost Alberta. Three Canadian National Seismic Network (CNSN) stations (EDM, SLEB and WALA) are also included in tomographic analysis (see Fig. 4.2a for locations).

Fig. 4.1 The deployment plan of the US Transportable Array. Twenty-one transportable stations from this experiment were used to constrain the seismic structure in southern Alberta and northernmost Montana. Source: USArray website http://www.usarray.org/maps

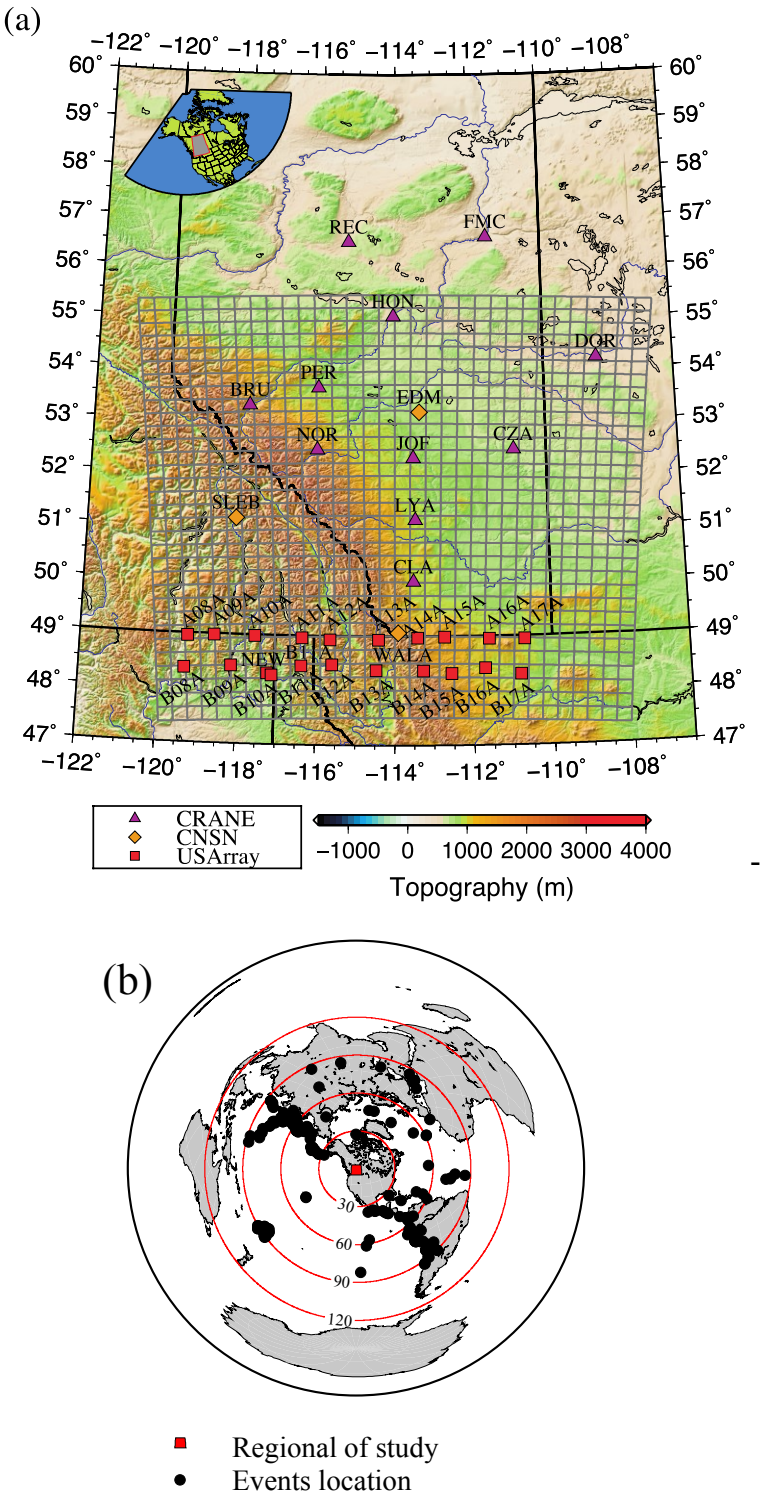
(a)
−122° −120° −118° −116° −114° −112° −110° −108°
60° 59° 58° 57° 56° 55° 54° 53° 52° 51° 50° 49° 48° 47°
REC
FMC
HQN
DQR
PER
BRU
EDM
NOR
JOF
CZA
SLEB
LYA
CLA
WALA
NEW
CRANE
CNSN
USArray
−1000 0 1000 2000 3000 4000
Topography (m)
(b)
30
60
90
120
Regional of study
Events location

Fig. 4.2a) Station distribution superimoposed on a regional topography map. b) Epicenter locations for 232 events used in this study. Red at the center of the plot indicate our region of study. Traveltime measurements from the teleseismic P wave are restricted between 30 and 90 degree epicentral distances.

4.2.2 Data processing

In contrast to the traditional ray theory tomography that treats the seismic wave as infinite frequency wave, finite-frequency theory considers the intrinsic volumetric zones of interference along the path of a seismic wave. The traveltime delays are frequency dependent [*Hung et al.*, 2004]because a long wavelength (low frequency) seismic wave is less sensitive to diffractions caused by velocity anomalies with scales comparable to the wavelength.

(a)

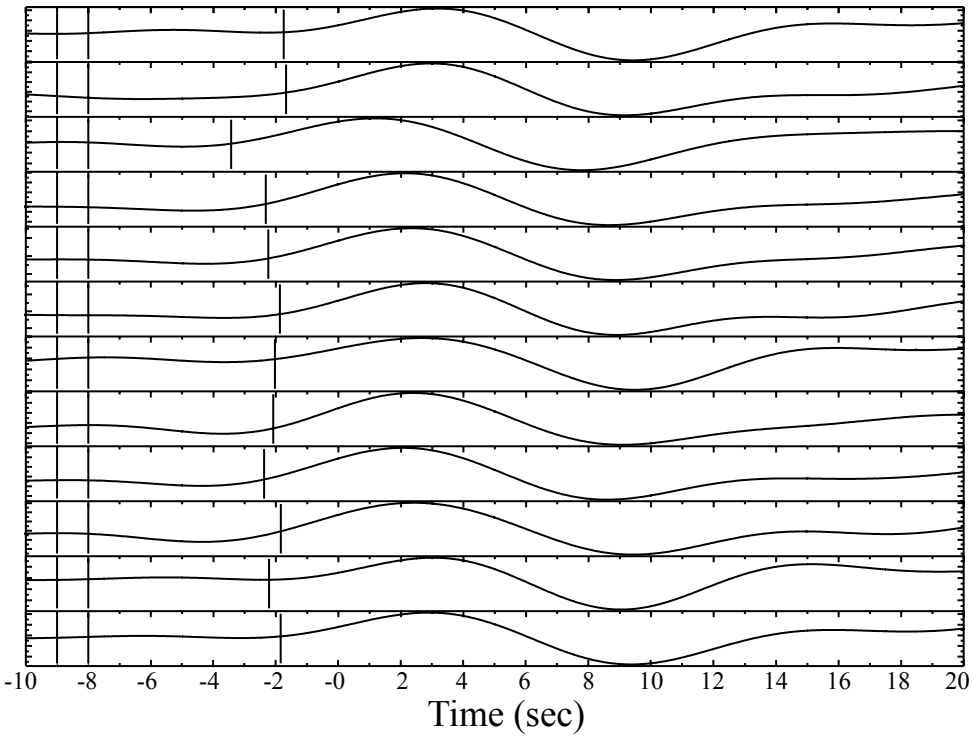
-10 -8 -6 -4 -2 -0 2 4 6 8 10 12 14 16 18 20
Time (sec)

(b)

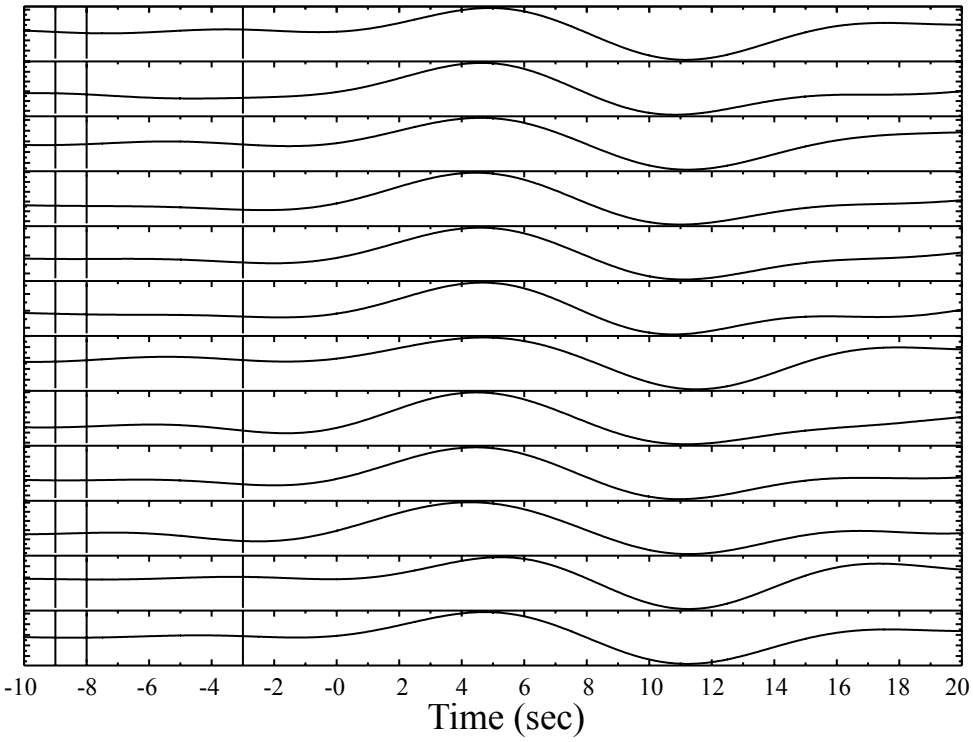
-10 -8 -6 -4 -2 -0 2 4 6 8 10 12 14 16 18 20
Time (sec)

Fig. 4.3 Broadband records filtered at intermediate frequency (0.03 – 0.125 Hz) for MCCC travel time measurements. (a) Seismograms aligned by theoretical P wave arrival time. (b) Seismograms aligned by MCCC measured arrival time.

(a)

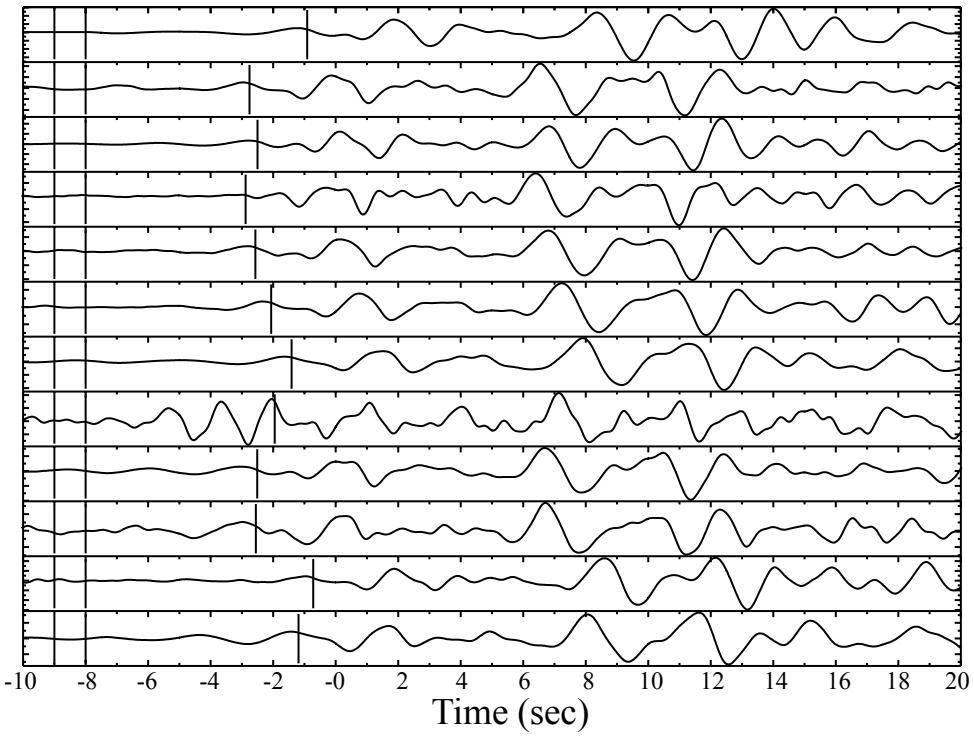
-10 -8 -6 -4 -2 -0 2 4 6 8 10 12 14 16 18 20
Time (sec)

(b)

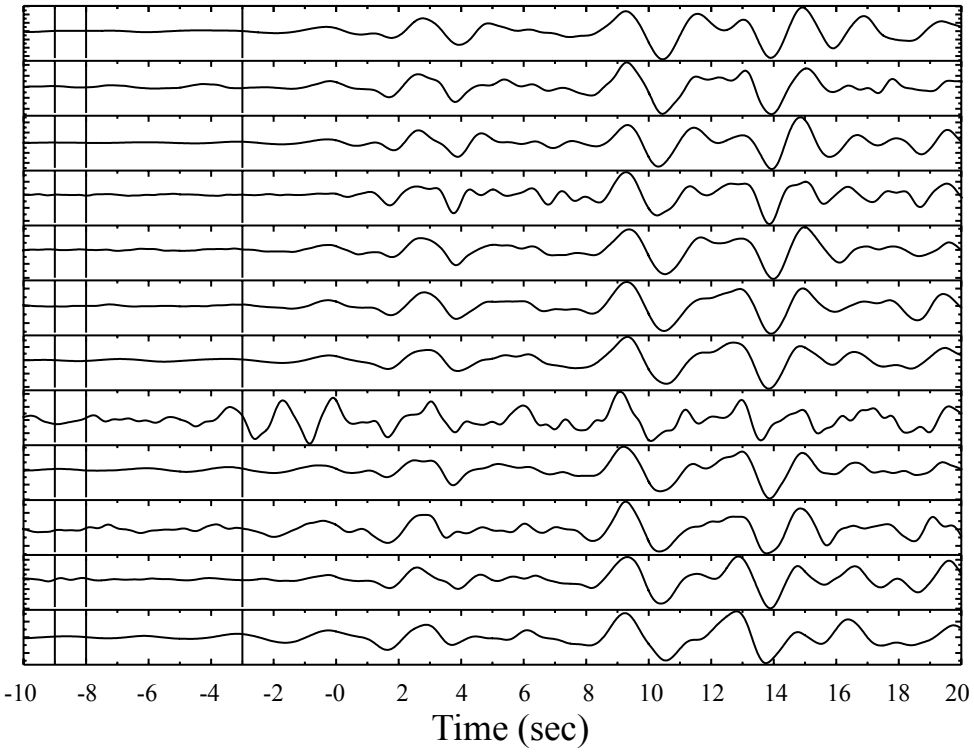
-10 -8 -6 -4 -2 -0 2 4 6 8 10 12 14 16 18 20
Time (sec)

Fig. 4.4 Broadband records filtered at high frequency (0.03 – 0.125 Hz) for MCCC travel time measurements. (a) Seismograms aligned by theoretical P wave arrival time. (b) Seismograms aligned by MCCC measured arrival time.

Furthermore, the wave front of low-frequency (long-period) seismic wave is healed more quickly than the high-frequency (short-period) ones sharing the same theoretical ray-path. As a result, the measured traveltime differences are usually smaller for the long-period event than its short-period counterpart, as illustrated by comparing the relative time shifts in Fig 4.3 with that in Fig. 4.4.

We filter the data into two different frequencies categories in order to fully utilize the added data constraints brought by the broadband records. P-wave arrival times for data of high frequency (0.125 – 2.0 Hz) and intermediate frequency (0.03 – 0.125 Hz) are measured with the multichannel cross correlation method (MCCC, *VanDecar and Crosson* [1990]). Precise traveltime differences are determined as the time delay that leads to the maximum cross correlation coefficient. The number of the measured P-wave delay times for high and intermediate frequency data are 4012 and 3797, respectively.

The measured traveltime differences δt are inverted for the fractional wave speed perturbation δc/c (δlnc) given the Frechet kernel $\mathbf{G}$ derived based on the Born single-scatter theory [*Hung et al.*, 2000]and ray paraxial approximation [*Dahlen et al.*, 2000]. The inverse problem of finite frequency tomography, similar to other geophysical inverse problems, could be expressed in concise matrix format as

$$\mathbf{Gm} = \mathbf{d}\,, \tag{4.1}$$

where $\mathbf{m}$ is model vector parameterized by discretizing the model into 33*33*33 nodes, $\mathbf{d}$ is the data vector that contains 7809 relative travel time measurements.

Equation (4.1) is an ill-conditioned linear system that could be solved by the LSQR algorithm [*Paige and Saunders*, 1982]. The model is parameterized in terms of regular nodes with a fixed scale, which requires proper norm damping schemes. We apply model smoothness and roughness constraints to stabilize the inversion due to the poor constraints to some of the model parameters [*Hung et al.*, 2011]. Such regularization schemes are effective in reinforcing the robust long-wavelength feature in sparse sampled regions but may degrade the spatial resolution where the model has sufficient data constraints[*Hung et al.*, 2011]. An alternative regularization method to balance the resolution in sparse- and dense-sampled region is the multi-scale parameterization method [*Chiao and Kuo*, 2001; *Hung et al.*, 2010]. In general, multi-scale parameterization adjusts the scale of model parameters according to the density of the data coverage in the model to ensure a spatially varying resolution[*Hung et al.*, 2011]. To accomplish this, model vector $\mathbf{m}$ is expanded into a wavelet basis function[*Li et al.*, 1996]

$$\widetilde{\mathbf{m}} = \mathbf{W}\mathbf{m}, \tag{4.2}$$

where $\mathbf{W}$ is the wavelet transform operator maps the model vector into the wavelet space. An inverse operator $\mathbf{W}^{-1}$ is used to recover the model vector $\mathbf{m}$. To associate the wavelet transformed model vector $\widetilde{\mathbf{m}}$ with the data vector, a modified kernel $\widetilde{\mathbf{G}}$ is introduced by

$$\widetilde{\mathbf{G}} = \mathbf{G}\mathbf{W}^{-1}. \tag{4.3}$$

We solve the new linear system equations in wavelet domain where

$$\widetilde{\mathbf{G}}\widetilde{\mathbf{m}} = \mathbf{d}, \tag{4.4}$$

and the form of the damped least square (DLS) is:

$$\widehat{\mathbf{m}} = \mathbf{W}^{-1}\left(\left(\left(\mathbf{W}^{-1}\right)^T \mathbf{G}^T\mathbf{C}^{-1}\mathbf{G}\mathbf{W}^{-1} + \mu\mathbf{I}\right)^{-1}\left(\mathbf{W}^{-1}\right)^T \mathbf{G}^T\mathbf{C}^{-1}\mathbf{d}\right), \qquad (4.5)$$

where $\mathbf{C}$ is the data covariance matrix, $\mathbf{I}$ is the identity matrix and μ is the damping parameter that adjusts the tradeoff between the misfit and model norm.

4.3 Results

4.3.1 Sensitivity test

We assess the resolution of the inversion through $\mathbf{G}^T\mathbf{G}$ matrix, for which the i-th diagonal element is the sum of squares of kernels contributing to the i-th node[*Hung et al.*, 2004; *Yang et al.*, 2006]. Thus, the value of $\mathrm{diag}\left(\mathbf{G}^T\mathbf{G}\right)$ could reflect the overall sensitivity of P-wave data contributing to each cell. The higher the $\mathrm{diag}\left(\mathbf{G}^T\mathbf{G}\right)$ value is, the better the corresponding cell is constrained.

The $\mathrm{diag}\left(\mathbf{G}^T\mathbf{G}\right)$ elements are computed for both ray and finite-frequency theory. The effect of the different theories on the path coverage of the model can be intuitively demonstrated by visualizing the spatial distribution of the $\mathrm{diag}\left(\mathbf{G}^T\mathbf{G}\right)$ elements. All nodes are fully covered (without any zero values in the model) at 8 individual depths based on finite-frequency approach (Fig. 4.5, left) while in the case of ray-theory, the "holes" in the model become evident at shallow depth due to incomplete sampling of the model space (Fig. 4.5, right). For instance, at 66 km depth, the ray is only sensitive to the model beneath the recording station where the seismic waves are convergent.

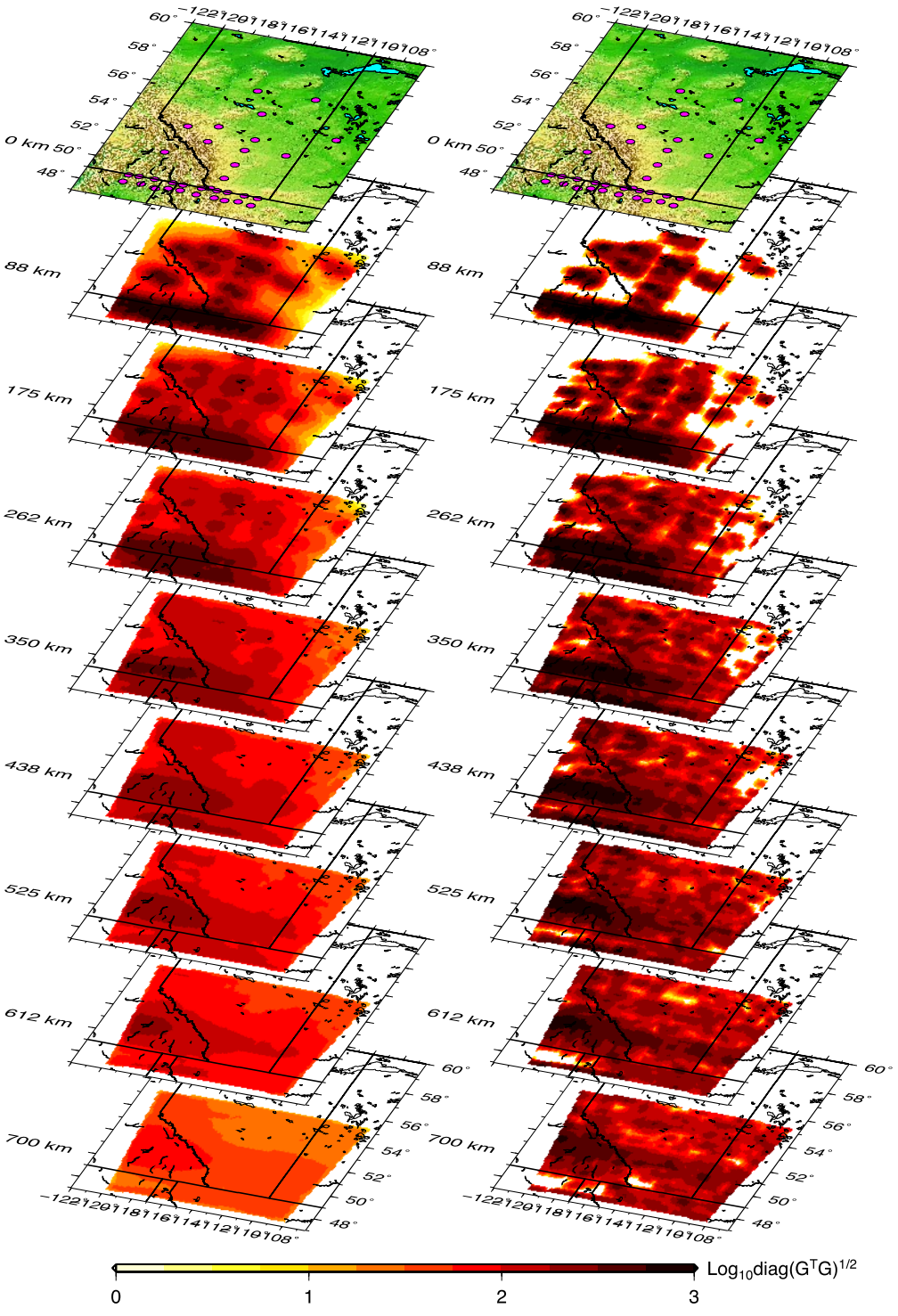
0 km
88 km
175 km
262 km
350 km
438 km
525 km
612 km
700 km
Log10diag(GTG)1/2
0
1
2
3

Fig. 4.5 The horizontal slices of $\mathrm{diag}\left(\mathbf{G}^T\mathbf{G}\right)$ show the differences between finite-frequency theory (left) and ray theory (right)

The path coverage for the ray theory resembles the geometry of the ray path (see Fig. 4.6 a). On the other hand, finite-frequency theory results in larger sampled region due to the broad sensitivity of the banana-donut (rather than 'wiry') kernel (see Fig. 4.6b for comparison)[*Hung et al.*, 2004].

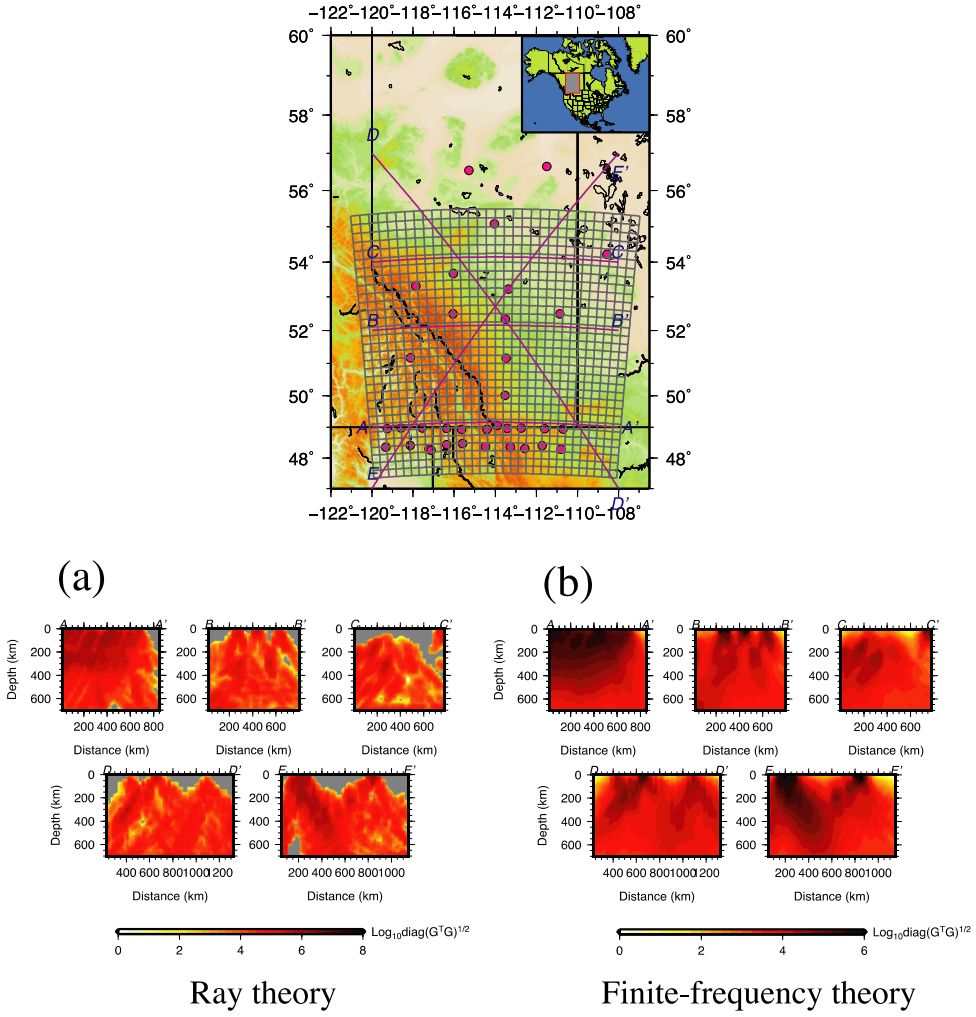

Fig. 4.6 Five cross-sections showing $\mathrm{diag}\left(\mathbf{G}^T\mathbf{G}\right)$ for (a) ray theory and (b) finite-frequency theory

The amplitude of $\mathrm{diag}\left(\mathbf{G}^T\mathbf{G}\right)$ for ray theory is higher than that of finite-frequency theory. The difference is attributed to the latter approach where the wave front healing effects on the cross-correlation determined traveltimeare properly considered. Under the finite-frequency assumption of the seismic wave, a velocity anomaly with the size close to or smaller than the wavelength of the

seismic wave would cause diffractive wave front healing[*Hung et al.*, 2004], which diminishes the authentic traveltime difference. On the other hand, ray theory assumes infinite frequency;hence the sizes of all anomalies are smaller than the wavelength. In other word, ray approximation usually overestimates contribution of an anomaly, as is evident in the relatively large value of $\mathrm{diag}\left(\mathbf{G}^T\mathbf{G}\right)$, to the observed traveltime shift.

4.3.2 Checkerboard test

To evaluate the robustness of the traveltime inversion results, we conduct a checkerboard test by constructing a synthetic model with 2.5% alternating positive and negative P velocity perturbations relative to the reference model. Each cubic cell possesses 5 nodesin latitude, longitude and depth directions forming a volume of $139 \times 208 \times 110$ km^3.

Synthetic data are calculated with the same event-station geometries as the observed data. Gaussian noise of 0.05 sec is subsequently added to the synthetic data. The results of the synthetic test are plotted on 5 cross-sections shown in Fig. 4.7.

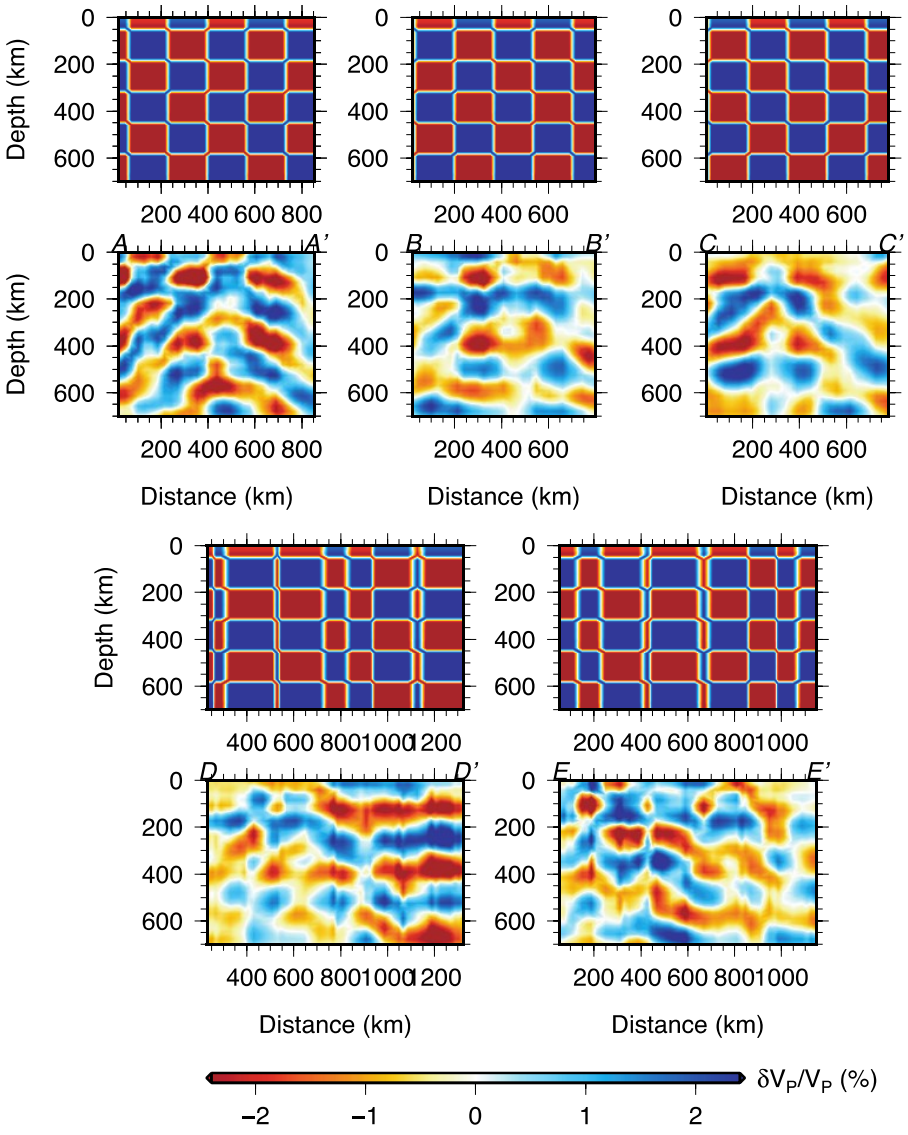

Fig. 4.7Checkerboard test for five cross-sections, the locations of which are shown in Fig. 4.6.

In the depth range from 50 to 400 km, the recovered model can clearly distinguish between the alternating velocity anomalies, especially in the vertical direction, despite minor lateral and oblique smearing effects. The level of maximum amplitude recovery is 80%.

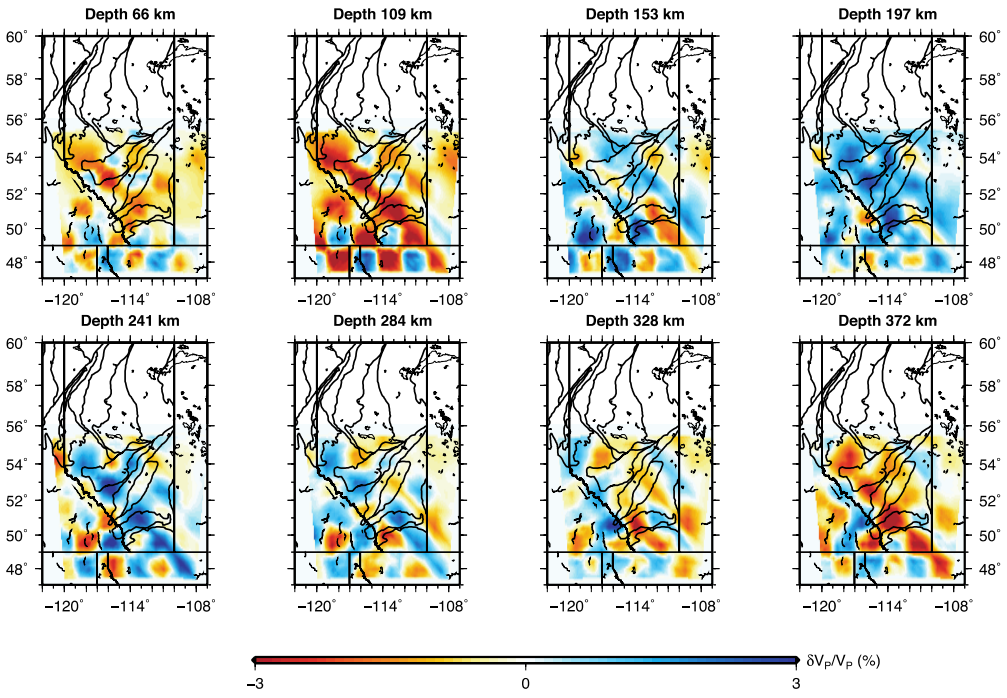

Fig. 4.8Checkerboard test results of horizontal slices for 8 depths.

The horizontal slices in the aforementioned depth range (50 to 400 km) show optimal resolution. For the regions with dense path coverage, e.g. southern Alberta (49° N to 51° N) near the USArray stations, the quality of model recovery is nearly 80% in maximum amplitude. Central Alberta between 51° N and 54° N displays acceptable resolution, with the exception of depth at 197 km that is dominated by the fast anomalies due to severe lateral smearing effects. The recovered model north of 54° N exhibits continuous velocity structures due to relatively sparse data coverage, hence caution must be exercised in the interpretation of observations in this region. In general, the vertical resolution is the highest at the depth below the crust andabovethe transition zone. The maximum lateral resolution is observed in the southwest along the Rocky Mountains where relatively dense station coverage is available. The amplitude of the recovered anomaly is ~80% of the input model in the

southwest but is reduced to ~50% in the northeast. Accordingly, only model values in the top 400 km will be discussed in the subsequent sections.

4.3.3 Upper mantle structure

We construct the five cross-sections (Fig. 4.9) with the same locations as those shown in the synthetic test. As the resolution of the model degrades northeastward, hence profile AA', BB' and CC' represent the cross-section with relatively high, intermediate and low model resolutions, respectively. AA' along the US-Canada border shows a major velocity gradient between a negative (west) and a positive (east) anomalies. The negative anomaly beneath the Canadian Rockies is interpreted to be hot upper mantle in connection with a relatively young Cordillera, while the positive anomaly that extends down to ~180 km represents the cratonic lithosphere of the Precambrian Canadian Shield. The patterns of heterogeneities on profiles BB' and CC' are generally well resolved suggesting positive anomalies beneath the approximate depth range of 50-180 km.Profile DD' enables a direct comparison with a similar cross-section by *Shragge et al.* [2002](hereinafter, Shragge02), showing the high velocity anomaly beneath Hearne. Profile EE', which shows a SW-NE geometry roughly parallel to present-day plate motion, aims to provide a broader view of the Cordillera to craton transition.

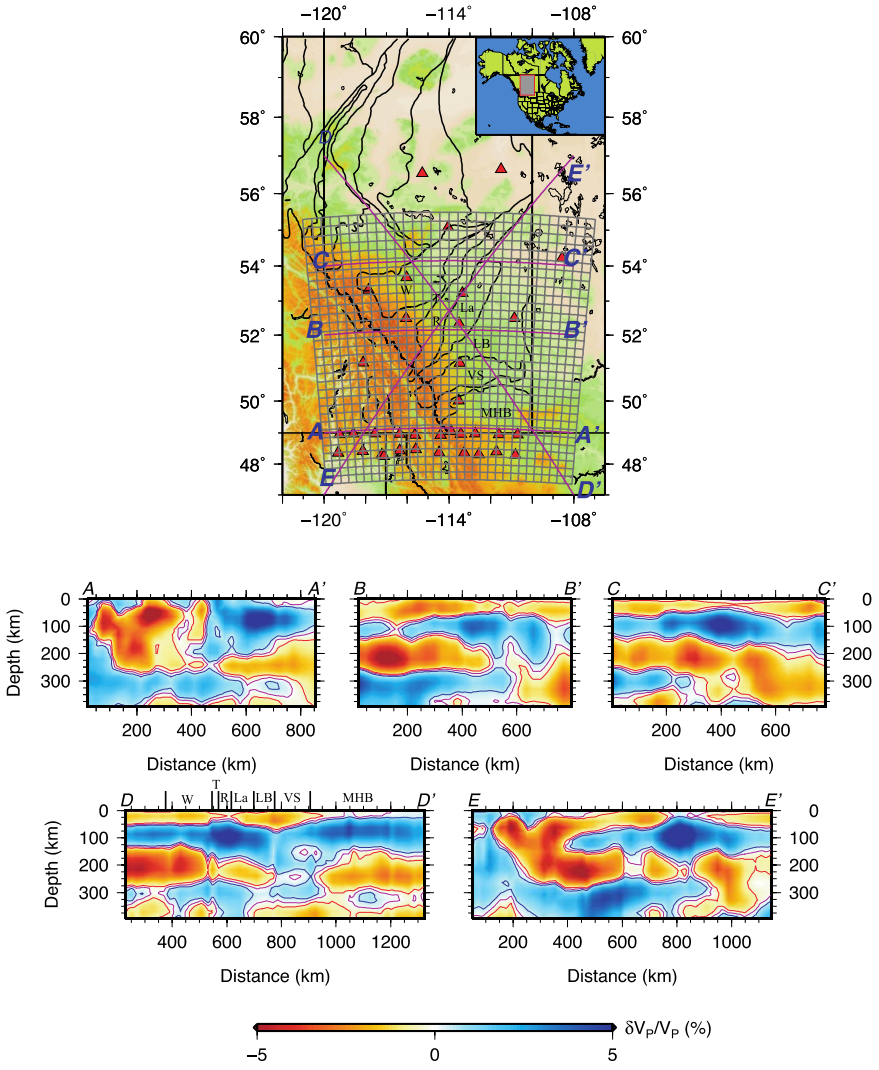

Fig. 4.9Cross-sections show the tomographic image from the inversion of the real data. Labelled domain: W, Wabanum Domain; T, Thorsby domain; R, Rimbey domain; La, Locombe domain; LB, Loverna block; VS, Vulcan structure; MHB, Medicine Hat Block.

4.5. Discussions

4.5.1 Cordillera-craton transition

Cordillera-craton transition is clearly imaged along AA' and EE' profiles. The upper mantle beneath the Cordillera is characterized by the velocity 0.5% lower than the regional average (0%), which is dominantly controlled by a high temperatures due to the thermal regime of the backarc region of a tectonically "young" North American Cordillera [*Hyndman*, 2010; *Hyndman and Currie*, 2011]. The temperature-depth relationship for southern Canadian Cordillera derived from S-wave velocity tomography and laboratory measurements of mineral properties indicates a temperature of ~1200 °C at 60 km depth [*Hyndman*, 2010]. East of the Cordillera, this high velocity anomaly potentially extends down to ~200 km, which suggests the bottoming depth of the old cratonic structure beneath Hearne. The vast area of the craton has undergone more than two billions of year's tectonic evolution including, but not limited to, collisional assembly, subduction, orogenesis and the accompanying tectonothermal events [*Ross*, 2002]. It has been suggested that the cratonic lithosphere gradually cooled during the inactive geologic periods after the Precambrian, showing minimal perturbation in the thermal structure of the upper mantle even during the most recent tectonic event in the Phanerozoic era [*Ross and Eaton*, 1999]. The temperature at 100 km depth in the craton region is ~800 °C[*Hyndman*, 2010]. The craton structure with a root at ~200 km is possibly terminated by the lithosphere-asthenosphere boundary (LAB), the depth of which is within the range of depth of LAB (170-260 km) reported by *Miller and Eaton* [2010]. The P velocity perturbation ranges between -0.5% and 0.5% down to ~200 km within a lateral distance of 50 km between the foothills and the adjacent Alberta basin, which suggests a sharp structural gradient in connection with the proposed Cordillera deformation front (CDF).

To evaluate the robustness, we compare our model with several recent tomographic maps from different research groups. We extract the cross-section along 49 °N from 4 models and compare it with our Cordillera-Craton Transition Velocity model (2014)(hereinafter CCTV14) and the results are shown in Fig. 4.10. Fig 4.10b shows the P velocity perturbation of the northwestern United States (NWUS11) by *James et al.* [2011], recovered from the inversion of teleseimic P-wave traveltimes using the ray theory assumption. It is worth noting that Cordillera-craton transition is defined in the top 200 km in NWUS11, but the transition boundary is positioned to the west of that of CCTV14 by ~150 km. The craton structure elongates obliquely to a depth of 400+ km, which is likely caused by smearing effect and/or limited vertical resolution. Fig 4.10c shows the profile extracted from the global velocity model (HMSL-S06) from long-period body-wave tomography by *Houser et al.* [2008]. Due to its global nature, the model is discretized into 4-degree wide model blocks and the craton structure suggested by the high velocities appear to extend more than 800 km laterally due to over-smoothing. The scale of the craton is 2 times larger than that of CCTV14 and the inferred CDF boundary is roughly 100 km west of our results. The model that shares comparable resolution with CCTV14 is DNA13 (Fig. 4.10d), a recent P and S velocity model of US derived from the joint inversion of teleseismic body-wave traveltimes and surface-wave phase velocities[*Porritt et al.*, 2013]. The spatial resolution is significantly improved by incorporating both body and surface waves, as suggested by the refined velocity structures in their model. The low velocity anomaly pertaining to Cordillera shows similar vertical and lateral scales to that of CCTV14. However, the craton structure is mainly confined between 114 °W and 112 °W in the former model, which is about 200 km shorter in longitudinal dimension thanthe estimation from craton scale in the CCTV14. The transitional boundary between the Cordillera and craton is in good agreement between these two models, which potentially extends to ~200 km near 114 °W. It is worth noting that DNA13 exhibits considerable effects of smearing along the incoming direction of the seismic waves, hence the vertical scale of the velocity

anomalies could be slightly exaggerated. Fig. 4.10e shows a comparable image from the P velocity model of western US (wUS), obtained from teleseismic P body-wave tomography [*Schmandt and Humphreys*, 2010]. While slow upper mantle beneath the Cordillera may not be well resolved in wUS, the presence of dominant triangle-shaped low velocity anomaly is well correlated with that of CCTV14. The positive anomaly that represents the cratonic lithosphere in wUS is again significantly broader than that of CCTV14 but close to that of the global scale HMSL model.

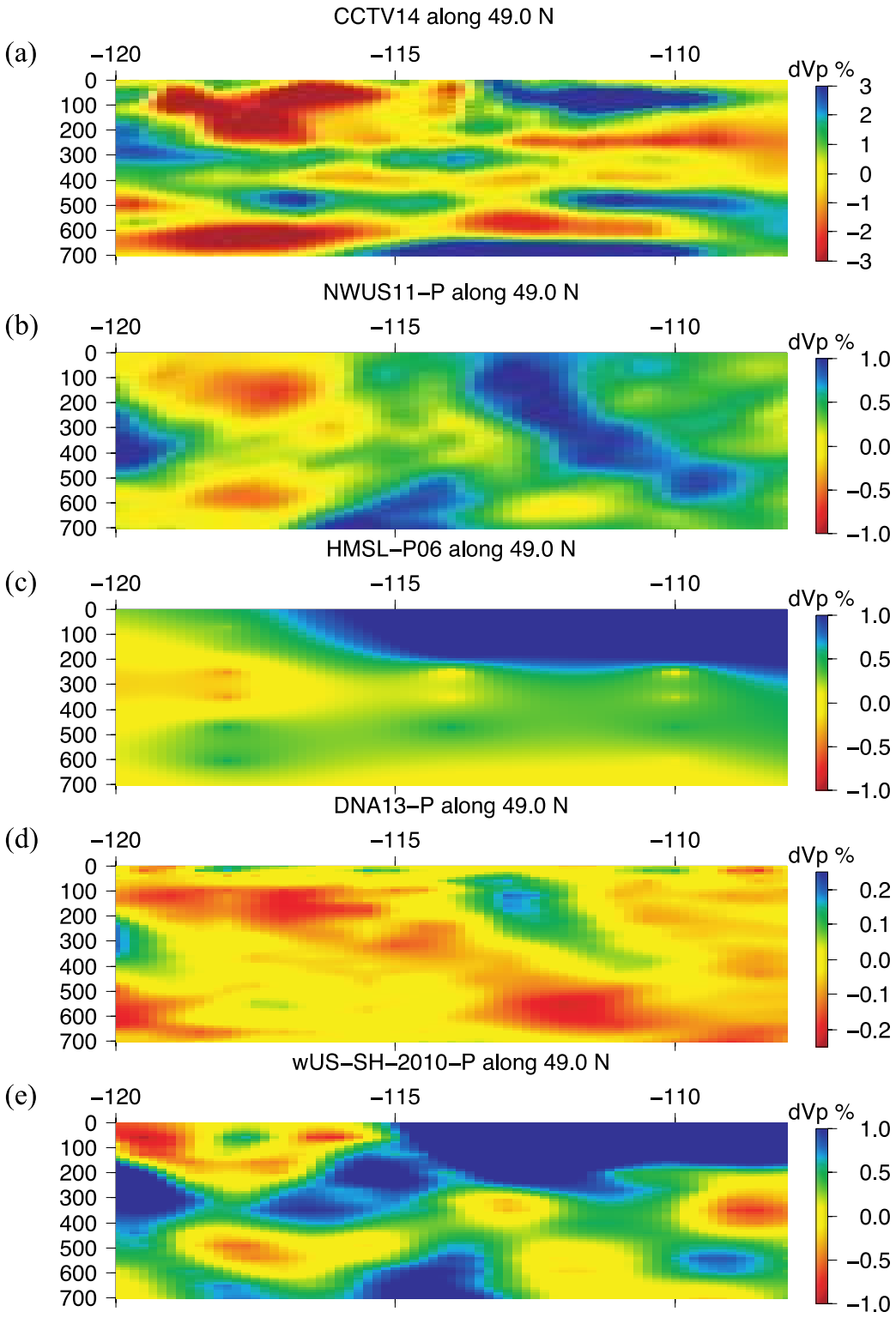
CCTV14 along 49.0 N
(a)
−120
−115
−110
0
100
200
300
400
500
600
700
dVp %
3
2
1
0
−1
−2
−3
NWUS11−P along 49.0 N
(b)
−120
−115
−110
0
100
200
300
400
500
600
700
dVp %
1.0
0.5
0.0
−0.5
−1.0
HMSL−P06 along 49.0 N
(c)
−120
−115
−110
0
100
200
300
400
500
600
700
dVp %
1.0
0.5
0.0
−0.5
−1.0
DNA13−P along 49.0 N
(d)
−120
−115
−110
0
100
200
300
400
500
600
700
dVp %
0.2
0.1
0.0
−0.1
−0.2
wUS−SH−2010−P along 49.0 N
(e)
−120
−115
−110
0
100
200
300
400
500
600
700
dVp %
1.0
0.5
0.0
−0.5
−1.0

Fig. 4.10Cross-sections along 49 N from a) CCTV14 model of this study, b) northwestern United States model by *James et al.* [2011](NWUS11), c) global P velocity model by*Houser et al.* [2008](HMSL-S06), d) P velocity model of US by*Porritt et al.* [2013](DNA13) and e) P velocity model of western US by *Schmandt and Humphreys* [2010](wUS).

To a certain degree, regional tomographic models,NWUS11, DNA13 and uWS, are affected by artifacts, which are evident in the systematic oblique elongations of the anomalies. The choices of the weighting/soothing schemes in the inversion and, more importantly, limited path converges of the incident body waves are mainly responsible. For the regional structure in Alberta, all these models are predominantly controlled by USArray stations south of 49 °N. The lack of receivers further north would significantly reduces the number of crossing rays, especially at upper mantle depths. In comparison, the inclusion of CRANE and CNSN stations offers regional path constraints for CCTV14, which exhibits minimal smearing structures above 400-km depth (also see the checkerboard test results in Fig. 4.7). In other words, the location of the Cordillera-craton transition in southern-central Alberta should be best resolved in our study. The following section provides a closer examination of cratonic lithosphere in this region.

4.5.2 Craton structure of central-southern Alberta

The positive anomaly beneath the vast region of the central-southern Alberta is potentially part of the Precambrian core of the western Laurentia. Our model overlaps with southern Hearne and Rae provinces, two lithospheric fragments of the Western Churchill province[*Hoffman*, 1989]. Separated by the enigmatic Snowbird Tectonic Zone (STZ), a SW-NE trending aeromagnetic and gravity anomaly, the Rae and Hearne provinces have been suggested to have collided during the Paleoproterozoic [*Ross et al.*, 1991]. The southwestern segment of the proposed collision suture and the Hearne province are well represented in our

model, especially DD' that spatially overlaps with an earlier cross-section of *Shragge et al.* [2002].

While the suggested lithosphere mantle signature extends down 250 km in Shragge02 beneath much of the Hearne province [*Shragge et al.*, 2002], the precise spatial scale of this high velocity structure remain questionable due to the limited data coverage provided by 9 linearly distributed stations, a short (1 year) deployment time, and the use of ray theoretical kernels in the inversion. In the DD' profile of CCTV14, we define the cratonic lithosphere by a value of 0.5% or above, a relatively high value that emphasizes the robust craton features and avoids over-interpreting the scale of the craton by minor variations. The most prominent feature on DD' profile is the continuous subhorizontal positive anomaly that spans the entirety of the Hearne province. The cratonic lithosphere is flat with nearly constant thickness of ~125 km beneath the Rae province. It is thickened by ~50 km beneath the Hearne province, where the lithosphere shows the highest velocity anomaly (~5%) that represents the ancient rigid core of the Hearne province, the Loverna Block (LB). The negative crustal anomaly overlying the Rae and LB are likely associated to the crustal low velocity zone in central Alberta due to Proterozoic granite intrusion[*Chen et al.*, 2014, Under review; *Gu and Shen*, 2014, under review]. A horizontally oriented high velocity structure is observed in the southeastern end of profile DD', where the lithosphere is concentrated between 0 and ~150 km and interpreted to be the Archean Medicine Hat Block (MHB). The lower crustal/upper mantle velocities of this region are distinctively faster than those beneath the LB and Rae province (See Fig. 4.9). The deepest craton root is observed near the base of LB, the oldest craton core, with a maximum depth of 200 km. This is distinctively shallower than the proposed value (250 km) by Shragge02, but appears to be at odds with the proposed lithosphere detachment [*Ross*, 2002].

Our model also sheds light on the formation of Vulcan structure (VS), which has been interpreted as a Precambrian rift zone by *Kanasewich et al.* [1969]. The Lithoprobe project conducted two reflection surveys including Southern Alberta Lithospheric Transect (SALT, *Lemieux et al.* [2000]) and Vibroseis Augmented Listen Time experiment (VAULT,*Eaton et al.* [1999]) that, together with the potential-field signature of VS, suggest that the VS marks a collisional suture zone between the MHB and LB [*Ross*, 2002]. The VS on our profile is potentially characterized by a low velocity crustal wedge between horizontally oriented high velocity zones beneath the LB in the northwest and the MHB in the southeast. The variable plate thicknesses (~180 km beneath LB and ~150 km beneath MHB), plate dipping angles (southeast for LB and northwest for MHB), slight negative values near the intersection of these two high velocity structures form a compelling argument that 1) LB and MHB belong to two different tectonic blocks and 2) VS is likely a collisional suture. A 3D view of the rigid core of cratonic lithosphere of LB and MHB are shown in Fig. 4.11.

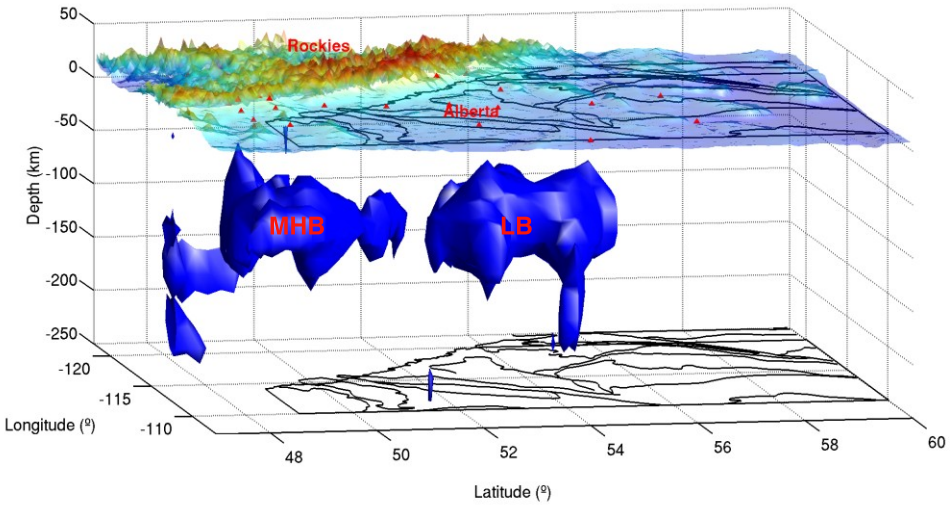

Fig. 4.11 3D view of lithosphere structure in the craton region. The blue color represents the isosurface of 2.5% positive anomaly. Two distinctive

lithospheric plates, Loverna Block (north) and Medicine Hat Block (south), are clearly defined.

An intriguing observation from CCTV14 is the asymmetry of high velocity structures beneath the LB and MHB. While the former structure continues down to 180-200 km, the southeastern counterpart beneath eastern MHB appears to terminate at ~150 km while exhibiting major complexities down to 300 km. The geometry of a low velocity zone between velocity structure 130-180 km depths in DD' profile (see Fig. 4.9) beneath eastern MHB/VS resembles that of a divot on the cratonic root, a structural complexity that could be associated with erosion or partial detachment. Unfortunately, earlier geophysical studies in this region provided only weak constraints on the lithosphere structure below 100 km due to limited penetration depths of the reflection/refraction methods. The lack of comparisons necessitates a closer examination of resolving power of our inversions. We computed synthetic traveltime data from a hypothetical cylinder shaped body of 2.5% positive velocity perturbations that resembles a thick lithosphere (see Fig. 4.12a and Fig. 4.12b). Gaussian noise of 0.05 sec is added to simulate observations. The damping parameter, regularization scheme and source-receiver path constraints remain the same from the inversion of real data. The recovered model is shown in Fig 4.12c and Fig. 4.12d.

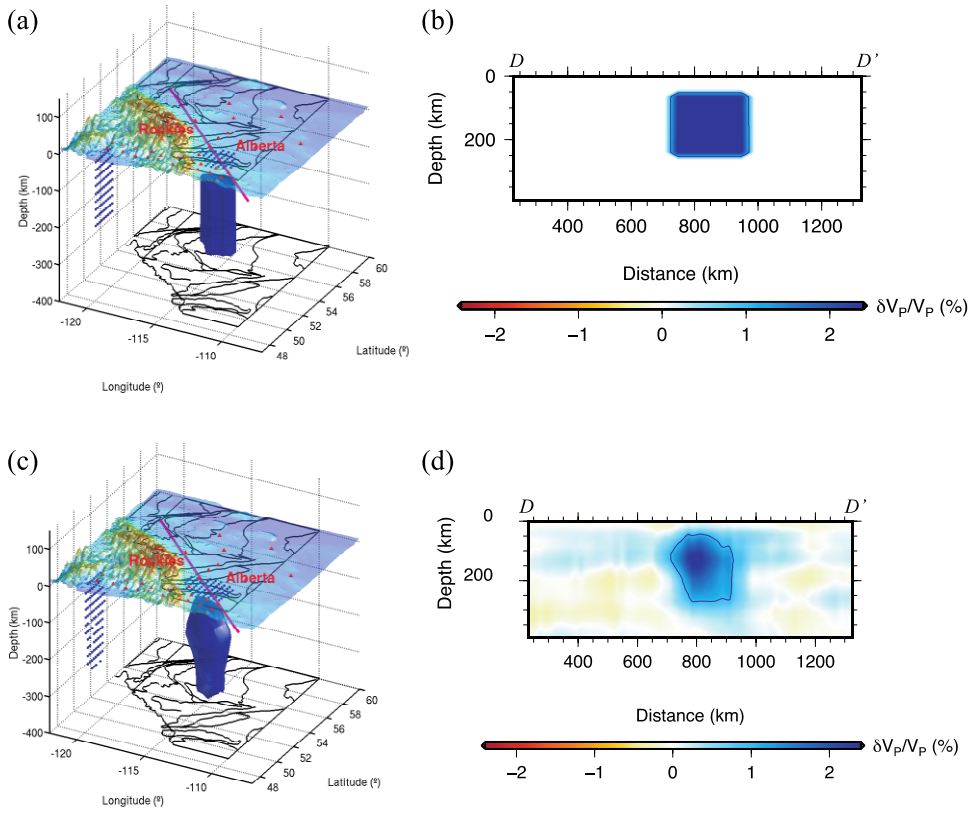

Fig. 4.12The results of the resolution test for a cylindrical high velocity structure resembling the lithosphere structure beneath MHB/VS. (a) Input model in 3D view. The red triangles present the station locations. The regions of blue dots are the projection of input model onto the surface and one side of the cube. The location of DD' is marked as the red line. (b) Input model shown on the DD' profile. (c) The recovered model in 3D view. (d) Recovered model on the DD' profile with contour line representing a 1% positive anomaly.

The contour of 1% velocity perturbation in the recovered model slightly underestimates the scale of the input anomaly in the lateral direction. The vertical scale of the recovered model, which is well constrained between 50 and 250 km, is in excellent agreement with that of the input model. Since only ~40% of the amplitude can be resolved, the geometry of the lithosphere is better constrained compared to its velocities.

Based on the results of checkerboard test (see Fig. 4.7 and 4.8) and this hypothesis test (see Fig. 4.12), we tentatively suggest that a thickened lithosphere beneath MHB or VS should be adequately resolved by our inversion. The corollary is that the divot at ~150 km beneath VS is most likely a robust feature in connection with a relatively thin lower lithosphere in the convergent tectonic environment. Partial detachment of the lithospheric root [*Ross*, 2002] in response to the subduction process occurred along the VS in Archean[*Clowes et al.*, 2002; *Gorman et al.*, 2002] may not be ruled out. However, the upper-to-middle lithosphere beneath both LB and MHB are most likely intact.

4.6 Conclusions

Finite-frequency method in combination with regional arrays provided us a high-resolution solution of the upper mantle structure beneath southern WCSB. Our P velocity model reveals a definitive Cordillera-craton transition structure in a ~50 km wide zone beneath the foothills of the southern Canadian Rockies. In the Alberta sedimentary basin underlain by the Canadian Shield, our model shows plate like fast velocity structures in connection with the Archean-aged cratonic lithospheres under Hearne and MHB. The lithosphere under LB extends down to ~180 km, while MHB is underlain by a ~150 km thick cratonic root structure. Both cratons exhibit low crustal velocities, especially the latter province. The Hearne lithosphere is about 20-70 km thinner than that suggested by *Shragge et al.* [2002], but there are no clear indications of a delaminated lithosphere root, especially under the Hearne province as suggested earlier by *Ross et al.* [2000]. The boundary zone of two distinctive microplates coincides with the location of the VS, which is mainly evidenced by a low velocity crustal wedge. Overall, the results of this study shed new lights on the Precambrian assembly and evolution of western Laurentia.

Chapter 5 Conclusions

The increased data volume from the CRANE provides a solid foundation for the implementation of a variety of seismic analysis methods. This thesis examines two types of seismic observations in details and combines two different imaging approaches to a better understanding of the regional crustal and upper mantle structures. Various chapters combine seismic imaging using receiver function, which provides detailed analysis of the sharp jumps in the seismic elastic properties, with an up-to-date tomographic method, which constrains the smooth variations in the seismic velocity field. Both imaging approaches have been the powerful tools in the understanding of the Earth's interior and dynamics. There are several important conclusions that can be drawn from this thesis. Below is a list of robust observations and interpretations based on the improved seismic data constraints from the local array.

1, Chapter 3 provides compelling evidence for a strong mid-crustal LVZ beneath central Alberta. P-to-S receiver functions from more than 9000 events are analyzed and inverted for the shear velocity structure down to 80 km. The thick (10+ km) and wide (200+ km) mid-crustal LVZ is interpreted to be a crystalized melt zone of granitic compositions, which is formed by the partial melting of the crust in Paleoproterozoic eon. In addition to favorable convergent tectonic environment in connection to THO, high spatial correlation between LVZ and heat flow and shear velocities that are consistent with laboratory measurements and reports of granite provide further evidence for our hypothesis. The existence of a broad crustal LVZ suggests extensive subduction, orogenesis, and crustal melting during the Precambrian assembly of the North American craton.

2, Chapter 4 presents a new tomographic model of P-wave velocity perturbations for the lithosphere and upper mantle beneath the Cordillera-cration transition region in southwestern Canada based on the inversion of the cross-correlation teleseismic relative traveltime. The up-to-date finite-frequency tomographic method provides us a high-resolution crustal and upper mantle model beneath southern WCSB. Our model reveals 1) A Cordillera-craton transiton structure in ~ 50 km wide zone beneath the proposed Cordillera Deformation Front (CDF); 2) Archean-aged cratonic lithosphere under the Loverna Block (LB) and Medicine Hat Block (MHB) and 3) a boundary zone evidenced by a low velocity crustal wedge between LB and MHB that coincides the Vulcan structure (VS).

Our new constraints based on receiver function imaging and tomography shed new light on the history and dynamics of the southwestern WCSB. The quality of the images and their correlation with the history below this region can certainly be improved further in the near future. The southernmost Alberta is well covered by the regional data while northern Alberta above 55° N the data coverage remains spotty, which leads to the difficulties to the interpretation of the seismic data. With more recordings from regional array and the continuing growth of the density of the stations in this area, these problems are expected to be overcome in the next 5 to 10 years.

Furthermore, even with the existing data additional work can bring fruitful results. For example the finite-frequency tomographic method can be easily applied to S-wave and simultaneously constrains S and P velocities and hence the Vp/Vs ratio, which can provide information not only on structure but also on the potential inclusion of fluid and mineralogy; seismic anisotropy brings another dimension of data set to verify some of the large-scale structures that we observed in the lithosphere. Ultimately, a community model should be a key objective for improving the understanding of the regional tectonic history and dynamics. Such

a model requires an integration of various results including body waves, surface waves [*Gu and Shen*, 2014, under review], anisotropic variation, P and S velocities, exploration seismic observations and MT data, etc. With the techniques and dataset analyzed from this study, such a community model is likely achievable within a decade. Hopefully, part of uncertainties can be answered and improvements can be implemented during my PhD study in the University of Alberta starting Fall 2014.

Bibiography

Abers, G. A. (2005), Seismic low-velocity layer at the top of subducting slabs: observations, predictions, and systematics, *Physics of the Earth and Planetary Interiors*, *149*(1), 7--29.

Aki, K., A. Christoffersson, and E. S. Husebye (1977), Determination of the three-dimensional seismic structure of the lithosphere, *Journal of Geophysical Research*, *82*(2), 277--296.

Aki, K., and P. G. Richards (2002), *Quantitative seismology*.

Allen, R. V. (1978), Automatic earthquake recognition and timing from single traces, *Bulletin of the Seismological Society of America*, *68*(5), 1521--1532.

Ammon, C. J. (1991), The isolation of receiver effects from teleseismic P waveforms, *Bulletin of the Seismological Society of America*, *81*(6), 2504--2510.

Ammon, C. J., G. E. Randall, and G. Zandt (1990), On the nonuniqueness of receiver function inversions, *Journal of Geophysical Research: Solid Earth (1978--2012)*, *95*(B10), 15303--15318.

Annesley, I. R., C. Madore, and P. Portella (2005), Geology and thermotectonic evolution of the western margin of the Trans-Hudson Orogen: evidence from the eastern sub-Athabasca basement, Saskatchewan, *Canadian Journal of Earth Sciences*, *42*(4), 573--597.

Astiz, L., et al. (2014), The Array Network Facility Seismic Bulletin: Products and an Unbiased View of United States Seismicity, *Seismological Research Letters*, *85*(3), 576--593.

Bachu, S. (1988), Analysis of heat transfer processes and geothermal pattern in the Alberta Basin, Canada, *Journal of Geophysical Research: Solid Earth (1978--2012)*, *93*(B7), 7767--7781.

Bachu, S. (1993), Basement heat flow in the Western Canada sedimentary basin, *Tectonophysics*, *222*(1), 119--133.

Bai, C.-Y., and B. Kennett (2001), Phase identification and attribute analysis of broadband seismograms at far-regional distances, *Journal of seismology*, *5*(2), 217--231.

Ballard, S., and H. N. Pollack (1987), Diversion of heat by Archean cratons: a model for southern Africa, *Earth and Planetary Science Letters*, *85*(1), 253--264.

Beck, S. L., and G. Zandt (2002), The nature of orogenic crust in the central Andes, *Journal of Geophysical Research: Solid Earth (1978--2012)*, *107*(B10), ESE--7.

Berman, R., W. Davis, and S. Pehrsson (2007), Collisional Snowbird tectonic zone resurrected: Growth of Laurentia during the 1.9 Ga accretionary phase of the Hudsonian orogeny, *Geology*, *35*(10), 911--914.

Bezacier, L., B. Reynard, J. D. Bass, C. Sanchez-Valle, and B. Van de Moort`ele (2010), Elasticity of antigorite, seismic detection of serpentinites, and anisotropy in subduction zones, *Earth and Planetary Science Letters*, *289*(1), 198--208.

Boerner, D., R. Kurtz, J. Craven, G. Ross, and F. Jones (2000), A synthesis of electromagnetic studies in the Lithoprobe Alberta Basement Transect: constraints on Paleoproterozoic indentation tectonics, *Canadian Journal of Earth Sciences*, *37*(11), 1509--1534.

Bostock, M. (1996), A seismic image of the upper mantle beneath the North American craton, *Geophysical Research Letters*, *23*(13), 1593--1596.

Bouzidi, Y., D. R. Schmitt, R. A. Burwash, and E. R. Kanasewich (2002), Depth migration of deep seismic reflection profiles: crustal thickness variations in Alberta, *Canadian Journal of Earth Sciences*, *39*(3), 331--350.

Burdick, L. J., and C. A. Langston (1977), Modeling crustal structure through the use of converted phases in teleseismic body-wave forms, *Bulletin of the Seismological Society of America*, *67*(3), 677--691.

Caldwell, W. B., S. L. Klemperer, S. S. Rai, and J. F. Lawrence (2009), Partial melt in the upper-middle crust of the northwest Himalaya revealed by Rayleigh wave dispersion, *Tectonophysics*, *477*(1), 58--65.

Cassidy, J. F. (1992), Numerical experiments in broadband receiver function analysis, *Bulletin of the Seismological Society of America*, *82*(3), 1453--1474.

Cassidy, J. F. (1995), A comparison of the receiver structure beneath stations of the Canadian National Seismograph Network, *Canadian Journal of Earth Sciences*, *32*(7), 938-951.

Chen, G., and R. H. Grapes (2007), *Granite genesis: in-situ melting and crustal evolution*, Springer.

Chen, Y., Y. J. Gu, M. D. Sacchi, and R. M. H. Dohkt (2014, Under review), Crustal Imprints of Precambrian Orogenesis in Western Laurentia.

Chen, Y., and F. Niu (2013), Ray-parameter based stacking and enhanced pre-conditioning for stable inversion of receiver function data, *Geophysical Journal International*, ggt179.

Chiao, L.-Y., and B.-Y. Kuo (2001), Multiscale seismic tomography, *Geophysical Journal International*, *145*(2), 517--527.

Chmielowski, J., G. Zandt, and C. Haberland (1999), The Central Andean Altiplano-Puna magma body, *Geophysical Research Letters*, *26*(6), 783--786.

Christensen, N. I., and W. D. Mooney (1995), Seismic velocity structure and composition of the continental crust: A global view, *Journal of Geophysical Research: Solid Earth (1978–2012)*, *100*(B6), 9761-9788.

Clayton, R. W., and R. A. Wiggins (1976), Source shape estimation and deconvolution of teleseismic bodywaves, *Geophysical Journal of the Royal Astronomical Society*, *47*(1), 151--177.

Clowes, R. M., M. J. Burianyk, A. R. Gorman, and E. R. Kanasewich (2002), Crustal velocity structure from SAREX, the southern Alberta refraction experiment, *Canadian Journal of Earth Sciences*, *39*(3), 351--373.

Clowes, R. M., A. J. Calvert, D. W. Eaton, Z. Hajnal, J. Hall, and G. M. Ross (1996), LITHOPROBE reflection studies of Archean and Proterozoic crust in Canada, *Tectonophysics*, *264*(1), 65--88.

Corrigan, D., S. Pehrsson, N. Wodicka, and E. De Kemp (2009), The Palaeoproterozoic Trans-Hudson Orogen: a prototype of modern accretionary processes, *Geological Society, London, Special Publications*, *327*(1), 457--479.

Courtier, A. M., J. B. Gaherty, J. Revenaugh, M. G. Bostock, and E. J. Garnero (2010), Seismic anisotropy associated with continental lithosphere accretion beneath the CANOE array, northwestern Canada, *Geology*, *38*(10), 887--890.

Crosson, R. S., and D. H. Hesser (1983), An algorithm for automated phase picking of digital seismograms from a regional network, *Eos*, *64*, 775.

Crotwell, H. P., and T. J. Owens (2005), Automated receiver function processing, *Seismological Research Letters*, *76*(6), 702--709.

Currie, C. A., J. F. Cassidy, R. D. Hyndman, and M. G. Bostock (2004), Shear wave anisotropy beneath the Cascadia subduction zone and western North American craton, *Geophysical Journal International*, *157*(1), 341-353.

Dahlen, F., S.-H. Hung, and G. Nolet (2000), Fréchet kernels for finite-frequency traveltimes---I. Theory, *Geophysical Journal International*, *141*(1), 157--174.

Deschamps, F., M. Godard, S. e. Guillot, and K. Hattori (2013), Geochemistry of subduction zone serpentinites: A review, *Lithos*, *178*, 96--127.

Dueker, K. G., and A. F. Sheehan (1997), Mantle discontinuity structure from midpoint stacks of converted P to S waves across the Yellowstone hotspot track, *Journal of Geophysical Research: Solid Earth (1978--2012)*, *102*(B4), 8313--8327.

Dziewonski, A. M., and D. L. Anderson (1981), Preliminary reference Earth model, *Physics of the earth and planetary interiors*, *25*(4), 297--356.

Earle, P. S., and P. M. Shearer (1994), Characterization of global seismograms using an automatic-picking algorithm, *Bulletin of the Seismological Society of America*, *84*(2), 366--376.

Eaton, D. W., and J. F. Cassidy (1996), A relic Proterozoic subduction zone in western Canada: New evidence from seismic reflection and receiver function data, *Geophysical Research Letters*, *23*(25), 3791--3794.

Eaton, D. W., G. M. Ross, and R. M. Clowes (1999), Seismic-reflection and potential-field studies of the Vulcan structure, western Canada: A Paleoproterozoic Pyrenees?, *Journal of Geophysical Research: Solid Earth (1978--2012)*, *104*(B10), 23255--23269.

Flowers, R., S. Bowring, and M. Williams (2006), Timescales and significance of high-pressure, high-temperature metamorphism and mafic dike anatexis, Snowbird tectonic zone, Canada, *Contributions to Mineralogy and Petrology*, *151*(5), 558--581.

Frederiksen, A., M. Bostock, and J. Cassidy (2001), S-wave velocity structure of the Canadian upper mantle, *Physics of the Earth and Planetary Interiors*, *124*(3), 175--191.

Frederiksen, A., M. Bostock, J. VanDecar, and J. Cassidy (1998), Seismic structure of the upper mantle beneath the northern Canadian Cordillera from teleseismic travel-time inversion, *Tectonophysics*, *294*(1), 43--55.

French, S., K. Fischer, E. Syracuse, and M. Wysession (2009), Crustal structure beneath the Florida-to-Edmonton broadband seismometer array, *Geophysical Research Letters*, *36*(8).

Gorman, A. R., R. M. Clowes, R. M. Ellis, T. J. Henstock, G. D. Spence, G. R. Keller, A. Levander, C. M. Snelson, M. J. A. Burianyk, and E. R. Kanasewich (2002), Deep Probe: imaging the roots of western North America, *Canadian Journal of Earth Sciences*, *39*(3), 375-398.

Grotzinger, J., and T. H. Jordan (2010), *Understanding earth*, Macmillan.

Gu, Y. J. (2010), *Arrays and array methods in global seismology*, Springer.

Gu, Y. J., A. Okeler, L. Shen, and S. Contenti (2011), the canadian rockies and alberta network (crane): new constraints on the rockies and western canada sedimentary basin, *Seismological Research Letters*, *82*(4), 575--588.

Gu, Y. J., A. Okeler, S. Contenti, K. Kocon, L. Shen, and K. Brzak (2009), Broadband seismic array deployment and data analysis in Alberta, *CSEG Recorder, September*, 37--44.

Gu, Y. J., D. Pana, and I. D. Bastow (2014, manuscript in preparation), Crustal Characteristics and Inferences for Proterozoic Craton Evolution in Southwestern Laurentia.

Gu, Y. J., and L. Shen (2014, under review), Noise correlation tomography of Southwest Western Canada Sedimentary Basin.

Gurrola, H., G. E. Baker, and J. B. Minster (1995), Simultaneous time-domain deconvolution with application to the computation of receiver functions, *Geophysical Journal International*, *120*(3), 537-543.

Hanmer, S., M. Williams, and C. Kopf (1995), Striding-Athabasca mylonite zone: implications for the Archean and Early Proterozoic tectonics of the western Canadian Shield, *Canadian Journal of Earth Sciences*, *32*(2), 178--196.

Hoffman, P. F. (1988), United Plates of America, the birth of a craton-Early Proterozoic assembly and growth of Laurentia, *Annual Review of Earth and Planetary Sciences*, *16*, 543--603.

Hoffman, P. F. (1989), Precambrian geology and tectonic history of North America, *The Geology of North America*, 447--512.

Houser, C., G. Masters, P. Shearer, and G. Laske (2008), Shear and compressional velocity models of the mantle from cluster analysis of long-period waveforms, *Geophysical Journal International*, *174*(1), 195--212.

Humphreys, E., and R. W. Clayton (1988), Adaptation of back projection tomography to seismic travel time problems, *Journal of Geophysical Research: Solid Earth (1978--2012)*, *93*(B2), 1073--1085.

Hung, S. H., W.-P. Chen, and L.-Y. Chiao (2011), A data-adaptive, multiscale approach of finite-frequency, traveltime tomography with special reference to P and S wave data from central Tibet, *Journal of Geophysical Research: Solid Earth (1978--2012)*, *116*(B6).

Hung, S. H., W.-P. Chen, L.-Y. Chiao, and T.-L. Tseng (2010), First multi-scale, finite-frequency tomography illuminates 3-D anatomy of the Tibetan Plateau, *Geophysical Research Letters*, *37*(6).

Hung, S. H., F. Dahlen, and G. Nolet (2000), Frechet kernels for finite-frequency traveltimeseII. Examples, *Geophysical Journal International*, *141*(1), 175--203.

Hung, S. H., Y. Shen, and L.-Y. Chiao (2004), Imaging seismic velocity structure beneath the Iceland hot spot: A finite frequency approach, *Journal of Geophysical Research: Solid Earth (1978--2012)*, *109*(B8).

Hyndman, R. (2010), The consequences of Canadian Cordillera thermal regime in recent tectonics and elevation: a review, *Canadian Journal of Earth Sciences*, *47*(5), 621--632.

Hyndman, R., and C. Currie (2011), Why is the North America Cordillera high? Hot backarcs, thermal isostasy, and mountain belts, *Geology*, *39*(8), 783--786.

James, D. E., M. J. Fouch, R. W. Carlson, and J. B. Roth (2011), Slab fragmentation, edge flow and the origin of the Yellowstone hotspot track, *Earth and Planetary Science Letters*, *311*(1), 124--135.

James, D. E., F. Niu, and J. Rokosky (2003), Crustal structure of the Kaapvaal craton and its significance for early crustal evolution, *Lithos*, *71*(2), 413--429.

Kanasewich, E., R. Clowes, and C. McCloughan (1969), A buried Precambrian rift in western Canada, *Tectonophysics*, *8*(4), 513--527.

Kennett, B., E. Engdahl, and R. Buland (1995), Constraints on seismic velocities in the Earth from traveltimes, *Geophysical Journal International*, *122*(1), 108--124.

Kilb, D., R. Newman, F. Vernon, J. Eakins, L. Ziegler, J. Bowen, and J. Otero (2003), Education and outreach based on data from the Anza seismic network in southern California, *Seismological Research Letters*, *74*(5), 522--528.

Kind, R., J. Ni, W. Zhao, J. Wu, X. Yuan, L. Zhao, E. Sandvol, C. Reese, J. Nabelek, and T. Hearn (1996), Evidence from earthquake data for a partially molten crustal layer in southern Tibet, *Science*, *274*(5293), 1692--1694.

Kumar, M. R., D. Ramesh, J. Saul, D. Sarkar, and R. Kind (2002), Crustal structure and upper mantle stratigraphy of the Arabian shield, *Geophysical Research Letters*, *29*(8), 130--131.

Landes, M., J. Ritter, B. O'Reilly, P. Readman, and V. Do (2006), AN---S receiver function profile across the Variscides and Caledonides in SW Ireland, *Geophysical Journal International*, *166*(2), 814--824.

Langston, C. A. (1979), Structure under Mount Rainier, Washington, inferred from teleseismic body waves, *Journal of Geophysical Research: Solid Earth (1978--2012)*, *84*(B9), 4749--4762.

Lawrence, J. F., and P. M. Shearer (2006), A global study of transition zone thickness using receiver functions, *Journal of Geophysical Research: Solid Earth (1978--2012)*, *111*(B6).

Lawson, C. L., and R. J. Hanson (1974), *Solving least squares problems*, SIAM.

Lemieux, S., G. M. Ross, and F. A. Cook (2000), Crustal geometry and tectonic evolution of the Archean crystalline basement beneath the southern Alberta Plains, from new seismic reflection and potential-field studies, *Canadian Journal of Earth Sciences*, *37*(11), 1473--1491.

Lewry, J., M. Stauffer, and S. Fumerton (1981), A cordilleran-type batholitic belt in the Churchill province in northern Saskatchewan, *Precambrian Research*, *14*(3), 277--313.

Li , H., W. Su, C.-Y. Wang, Z. Huang, and Z. Lv (2010), Ambient noise Love wave tomography in the eastern margin of the Tibetan plateau, *Tectonophysics*, *491*(1), 194--204.

Li , S., M. J. Unsworth, J. R. Booker, W. Wei, H. Tan, and A. G. Jones (2003), Partial melt or aqueous fluid in the mid-crust of Southern Tibet? Constraints from INDEPTH magnetotelluric data, *Geophysical Journal International*, *153*(2), 289--304.

Li, X., G. Bock, A. Vafidis, R. Kind, H.-P. Harjes, W. Hanka, K. Wylegalla, M. Van Der Meijde, and X. Yuan (2003), Receiver function study of the Hellenic subduction zone: imaging crustal thickness variations and the oceanic Moho of the descending African lithosphere, *Geophysical Journal International*, *155*(2), 733--748.

Li, X., M. D. Sacchi, and T. J. Ulrych (1996), Wavelet transform inversion with prior scale information, *Geophysics*, *61*(5), 1379-1385.

Ligorría, J. P., and C. J. Ammon (1999), Iterative deconvolution and receiver-function estimation, *Bulletin of the Seismological Society of America*, *89*(5), 1395--1400.

Liu, Q., and Y. Gu (2012), Seismic imaging: from classical to adjoint tomography, *Tectonophysics*, *566*, 31--66.

Lucas, S., A. Green, Z. Hajnal, D. White, J. Lewry, K. Ashton, W. Weber, and R. Clowes (1993), Deep seismic profile across a Proterozoic collision zone: surprises at depth, *Nature*.

Majorowicz, J., and S. E. Grasby (2010), Heat flow, depth--temperature variations and stored thermal energy for enhanced geothermal systems in Canada, *Journal of Geophysics and Engineering*, *7*(3), 232.

Mangino, S. G., G. Zandt, and C. J. Ammon (1993), The receiver structure beneath Mina, Nevada, *Bulletin of the Seismological Society of America*, *83*(2), 542--560.

Marquering, H., F. Dahlen, and G. Nolet (1999), Three-dimensional sensitivity kernels for finite-frequency traveltimes: the banana-doughnut paradox, *Geophysical Journal International*, *137*(3), 805--815.

Masson, F., A. Jacob, C. Prodehl, P. Readman, P. Shannon, A. Schulze, and U. Enderle (1998), A wide-angle seismic traverse through the Variscan of southwest Ireland, *Geophysical Journal International*, *134*(3), 689--705.

Mercier, J.-P., M. Bostock, J. Cassidy, K. Dueker, J. Gaherty, E. Garnero, J. Revenaugh, and G. Zandt (2009), Body-wave tomography of western Canada, *Tectonophysics*, *475*(3), 480--492.

Miller, M. S., and D. W. Eaton (2010), Formation of cratonic mantle keels by arc accretion: Evidence from S receiver functions, *Geophysical Research Letters*, *37*(18).

Monsalve, H., J. F. Pacheco, C. A. Vargas, and Y. A. Morales (2013), Crustal velocity structure beneath the western Andes of Colombian using receiver-function inversion, *Journal of South American Earth Sciences*, *48*, 106--122.

Montagner, J.-P., and B. Kennett (1996), How to reconcile body-wave and normal-mode reference Earth models, *Geophysical Journal International*, *125*(1), 229--248.

Montelli, R., G. Nolet, F. Dahlen, and G. Masters (2006), A catalogue of deep mantle plumes: New results from finite-frequency tomography, *Geochemistry, Geophysics, Geosystems*, *7*(11).

Mueller, S. (1977), A new model of the continental crust, *Geophysical Monograph Series*, *20*, 289--317.

Mueller, S., and M. Landisman (1966), Seismic Studies of the Earth's Crust in Continents I: Evidence for a Low‐Velocity Zone in the Upper Part of the Lithosphere*, *Geophysical Journal of the Royal Astronomical Society*, *10*(5), 525-538.

Nelson, K. D., et al. (1996), Partially molten middle crust beneath southern Tibet: Synthesis of project INDEPTH results, *Science*, *274*(5293), 1684--1688.

Niu, F. (2011), Preface to the special issue on seismic array analysis and CEArray, *Earthquake Science*, *24*(1), 1--2.

Obara, K. (2003), Hi-net: High sensitivity seismograph network, Japan, in *Methods and Applications of Signal Processing in Seismic Network Operations*, edited, pp. 79--88, Springer.

Owens, T. J., G. Zandt, and S. R. Taylor (1984), Seismic evidence for an ancient rift beneath the Cumberland Plateau, Tennessee: A detailed analysis of broadband teleseismic P waveforms, *Journal of Geophysical Research: Solid Earth (1978--2012)*, *89*(B9), 7783--7795.

Paige, C. C., and M. A. Saunders (1982), LSQR: An algorithm for sparse linear equations and sparse least squares, *ACM Transactions on Mathematical Software (TOMS)*, *8*(1), 43--71.

Park, J., and V. Levin (2000), Receiver functions from multiple-taper spectral correlation estimates, *Bulletin of the Seismological Society of America*, *90*(6), 1507--1520.

Petford, N., A. Cruden, K. McCaffrey, and J.-L. Vigneresse (2000), Granite magma formation, transport and emplacement in the Earth's crust, *Nature*, *408*(6813), 669--673.

Porritt, R. W., R. M. Allen, and F. F. Pollitz (2013), Seismic imaging east of the Rocky Mountains with USArray, *Earth and Planetary Science Letters*.

Porter, J., R. Price, and R. McCrossan (1982), The western Canada sedimentary basin, *Philosophical Transactions of the Royal Society of London. Series A, Mathematical and Physical Sciences*, *305*(1489), 169--192.

Price, R. (1981), The Cordilleran foreland thrust and fold belt in the southern Canadian Rocky Mountains.

Price, R. (1994), Cordilleran tectonics and the evolution of the Western Canada Sedimentary Basin, *Geological Atlas of the Western Canada Sedimentary Basin*, *4*.

Price, R., and E. Mountjoy (1970), Geologic structure of the Canadian Rocky Mountains between Bow and Athabasca Rivers---a progress report, *Structure of the southern Canadian Cordillera: Geological Association of Canada Special Paper*, *6*, 7--25.

Rapine, R., F. Tilmann, M. West, J. Ni, and A. Rodgers (2003), Crustal structure of northern and southern Tibet from surface wave dispersion analysis, *Journal of Geophysical Research: Solid Earth (1978--2012)*, *108*(B2).

Rawlinson, N., and M. Sambridge (2003), Seismic traveltime tomography of the crust and lithosphere, *Advances in Geophysics*, *46*, 81--199.

Romanowicz, B. (1991), Seismic tomography of the Earth's mantle, *Annual Review of Earth and Planetary Sciences*, *19*, 77.

Rondenay, S. (2009), Upper mantle imaging with array recordings of converted and scattered teleseismic waves, *Surveys in geophysics*, *30*(4-5), 377--405.

Ross, G. M. (2002), Evolution of Precambrian continental lithosphere in Western Canada: results from Lithoprobe studies in Alberta and beyond, *Canadian Journal of Earth Sciences*, *39*(3), 413--437.

Ross, G. M., J. Broome, and W. Miles (1994), Potential fields and basement structure: Western Canada Sedimentary Basin, *Geological atlas of the Western Canada Sedimentary Basin. Compiled by GD Mossop and I. Shetsen. Canadian Society of Petroleum Geologists and Alberta Research Council, Calgary, Alta*, 41--48.

Ross, G. M., and D. W. Eaton (1999), Basement reactivation in the Alberta Basin: Observational constraints and mechanical rationale, *Bulletin of Canadian Petroleum Geology*, *47*(4), 391--411.

Ross, G. M., D. W. Eaton, D. E. Boerner, and W. Miles (2000), Tectonic entrapment and its role in the evolution of continental lithosphere: an example from the Precambrian of western Canada, *Tectonics*, *19*(1), 116-134.

Ross, G. M., B. Milkereit, D. Eaton, D. White, E. R. Kanasewich, and M. J. A. Burianyk (1995), Paleoproterozoic collisional orogen beneath the western Canada sedimentary basin imaged by Lithoprobe crustal seismic-reflection data, *Geology*, *23*(3), 195-199.

Ross, G. M., R. R. Parrish, M. E. Villeneuve, and S. A. Bowring (1991), Geophysics and geochronology of the crystalline basement of the Alberta Basin, western Canada, *Canadian Journal of Earth Sciences*, *28*(4), 512--522.

Rost, S., and C. Thomas (2002), Array seismology: methods and applications, *Reviews of geophysics*, *40*(3), 2--1.

Rudnick, R. L., and D. M. Fountain (1995), Nature and composition of the continental crust: a lower crustal perspective, *Reviews of Geophysics*, *33*(3), 267--309.

Sambridge, M., and G. Drijkoningen (1992), Genetic algorithms in seismic waveform inversion, *Geophysical Journal International*, *109*(2), 323--342.

Sambridge, M. S. (1990), Non-linear arrival time inversion: constraining velocity anomalies by seeking smooth models in 3-D, *Geophysical Journal International*, *102*(3), 653--677.

Sato, H., I. S. Sacks, and T. Murase (1989), The use of laboratory velocity data for estimating temperature and partial melt fraction in the low-velocity zone: Comparison with heat flow and electrical conductivity studies, *Journal of Geophysical Research: Solid Earth (1978--2012)*, *94*(B5), 5689--5704.

Scales, J. A. (1987), Tomographic inversion via the conjugate gradient method, *Geophysics*, *52*(2), 179--185.

Schmandt, B., and E. Humphreys (2010), Complex subduction and small-scale convection revealed by body-wave tomography of the western United States upper mantle, *Earth and Planetary Science Letters*, *297*(3), 435--445.

Schmitz, M., W.-D. Heinsohn, and F. Schilling (1997), Seismic, gravity and petrological evidence for partial melt beneath the thickened central Andean crust (21--23 S), *Tectonophysics*, *270*(3), 313--326.

Schultz, R., V. Stern, and Y. J. Gu (2014), An investigation of seismicity clustered near the Cordel Field, west central Alberta, and its relation to a nearby disposal well, *Journal of Geophysical Research: Solid Earth*.

Sheehan, A. F., G. A. Abers, C. H. Jones, and A. L. Lerner‐Lam (1995), Crustal thickness variations across the Colorado Rocky Mountains from teleseismic receiver functions, *Journal of Geophysical Research: Solid Earth (1978–2012)*, *100*(B10), 20391-20404.

Shibutani, T., M. Sambridge, and B. Kennett (1996), Genetic algorithm inversion for receiver functions with application to crust and uppermost mantle structure beneath eastern Australia, *Geophysical Research Letters*, *23*(14), 1829--1832.

Shragge, J., M. Bostock, C. Bank, and R. Ellis (2002), Integrated teleseismic studies of the southern Alberta upper mantle, *Canadian Journal of Earth Sciences*, *39*(3), 399--411.

St-Onge, M. R., M. P. Searle, and N. Wodicka (2006), Trans-Hudson Orogen of North America and Himalaya-Karakoram-Tibetan Orogen of Asia: Structural and thermal characteristics of the lower and upper plates, *Tectonics*, *25*(4).

Stein, S., and M. Wysession (2009), *An introduction to seismology, earthquakes, and earth structure*, John Wiley \& Sons.

Stern, T., D. Okaya, S. Kleffmann, M. Scherwath, S. Henrys, and F. Davey (2007), Geophysical exploration and dynamics of the Alpine fault zone, *A Continental Plate Boundary: Tectonics at South Island, New Zealand*, 207--233.

Stern, V., R. Schultz, L. Shen, Y. Gu, and D. Eaton (2013), Alberta earthquake catalogue 2006-2010 (GIS data, point features), *Alberta Energy Regulator, Digital Data*, *17*.

Thurber, C. H. (1983), Earthquake locations and three-dimensional crustal structure in the Coyote Lake area, central California, *Journal of Geophysical Research: Solid Earth (1978--2012)*, *88*(B10), 8226--8236.

Tromp, J., C. Tape, and Q. Liu (2005), Seismic tomography, adjoint methods, time reversal and banana-doughnut kernels, *Geophysical Journal International*, *160*(1), 195--216.

Turcotte, D. L., and G. Schubert (2014), *Geodynamics*, Cambridge University Press.

Unsworth, M., et al. (2005), Crustal rheology of the Himalaya and Southern Tibet inferred from magnetotelluric data, *Nature*, *438*(7064), 78--81.

Van der Hilst, R., M. De Hoop, P. Wang, S.-H. Shim, P. Ma, and L. Tenorio (2007), Seismostratigraphy and thermal structure of Earth's core-mantle boundary region, *science*, *315*(5820), 1813--1817.

Van Der Hilst, R. D., and V. Maarten (2005), Banana-doughnut kernels and mantle tomography, *Geophysical Journal International*, *163*(3), 956--961.

Van Der Lee, S., and A. Frederiksen (2005), Surface wave tomography applied to the North American upper mantle, *Seismic Earth: Array Analysis of Broadband Seismograms*, 67--80.

VanDecar, J. C., and R. S. Crosson (1990), Determination of teleseismic relative phase arrival times using multi-channel cross-correlation and least squares, *Bulletin of the Seismological Society of America*, *80*(1), 150-169.

Villeneuve, M., G. Ross, R. Thériault, W. Miles, R. Parrish, and J. Broome (1993), Tectonic subdivision and U-Pb geochronology of the crystalline basement of the Alberta Basin, Western Canada.

Ward, K. M., R. C. Porter, G. Zandt, S. L. Beck, L. S. Wagner, E. Minaya, and H. Tavera (2013), Ambient noise tomography across the Central Andes, *Geophysical Journal International*, *194*(3), 1559--1573.

Wei, W., et al. (2001), Detection of widespread fluids in the Tibetan crust by magnetotelluric studies, *Science*, *292*(5517), 716--719.

Wiggins, R. A. (1972), The general linear inverse problem: Implication of surface waves and free oscillations for earth structure, *Reviews of Geophysics*, *10*(1), 251--285.

Wilde-Piórko, M., and M. Grad (2002), Crustal structure variation from the Precambrian to Palaeozoic platforms in Europe imaged by the inversion of teleseismic receiver functions---project TOR, *Geophysical Journal International*, *150*(1), 261--270.

Yang, T., Y. Shen, S. van der Lee, S. C. Solomon, and S.-H. Hung (2006), Upper mantle structure beneath the Azores hotspot from finite-frequency seismic tomography, *Earth and Planetary Science Letters*, *250*(1), 11-26.

Yang , Y., M. H. Ritzwoller, Y. Zheng, W. Shen, A. L. Levshin, and Z. Xie (2012), A synoptic view of the distribution and connectivity of the mid-crustal low velocity zone beneath Tibet, *Journal of Geophysical Research: Solid Earth (1978--2012)*, *117*(B4).

Yuan, X., J. Ni, R. Kind, J. Mechie, and E. Sandvol (1997), Lithospheric and upper mantle structure of southern Tibet from a seismological passive source experiment, *Journal of Geophysical Research: Solid Earth (1978--2012)*, *102*(B12), 27491--27500.

Yuan, X., et al. (2000), Subduction and collision processes in the Central Andes constrained by converted seismic phases, *Nature*, *408*(6815), 958--961.

Zandt, G., A. A. Velasco, and S. L. Beck (1994), Composition and thickness of the southern Altiplano crust, Bolivia, *Geology*, *22*(11), 1003--1006.

Zelt, C. A., and R. Ellis (1989), Seismic structure of the crust and upper mantle in the Peace River Arch region, Canada, *Journal of Geophysical Research: Solid Earth (1978--2012)*, *94*(B5), 5729--5744.

Zheng, T., L. Zhao, and R. Zhu (2009), New evidence from seismic imaging for subduction during assembly of the North China Craton, *Geology*, *37*(5), 395--398.

Zhu, L., and H. Kanamori (2000), Moho depth variation in southern California from teleseismic receiver functions, *Journal of Geophysical Research: Solid Earth (1978--2012)*, *105*(B2), 2969--2980.

Zorin, Y. A., V. Mordvinova, E. K. Turutanov, B. Belichenko, A. Artemyev, G. Kosarev, and S. Gao (2002), Low seismic velocity layers in the Earth's crust beneath Eastern Siberia (Russia) and Central Mongolia: receiver function data and their possible geological implication, *Tectonophysics*, *359*(3), 307--327.